Titre: Title:	Development of an Endonasal Raman Spectroscopy Probe for Transsphenoidal Pituitary Adenoma Surgery
Auteur: Author:	Victor Blanquez-Yeste
Date:	2025
Type:	Mémoire ou thèse / Dissertation or Thesis
Référence: Citation:	Blanquez-Yeste, V. (2025). Development of an Endonasal Raman Spectroscopy Probe for Transsphenoidal Pituitary Adenoma Surgery [Mémoire de maîtrise, Polytechnique Montréal]. PolyPublie. https://publications.polymtl.ca/63028/

URL de PolyPublie: PolyPublie URL:	https://publications.polymtl.ca/63028/
Directeurs de recherche: Advisors:	Frédéric Leblond
Programme: Program:	Génie physique

POLYTECHNIQUE MONTRÉAL
affiliée à l'Université de Montréal

Development of an Endonasal Raman Spectroscopy Probe for Transsphenoidal Pituitary Adenoma Surgery

VICTOR BLANQUEZ-YESTE
Département de génie physique

Mémoire présenté en vue de l'obtention du diplôme de *Maîtrise ès sciences appliquées*
Génie physique

Février 2025

POLYTECHNIQUE MONTRÉAL
affiliée à l'Université de Montréal

Ce mémoire intitulé :

Development of an Endonasal Raman Spectroscopy Probe for Transsphenoidal Pituitary Adenoma Surgery

présenté par **Victor BLANQUEZ-YESTE**
en vue de l'obtention du diplôme de *Maîtrise ès sciences appliquées*
a été dûment accepté par le jury d'examen constitué de :

Stephan REUTER, président
Frédéric LEBLOND, membre et directeur de recherche
Lucien WEISS, membre

DEDICATION

To my parents and brothers who always supported me
To Luna

ACKNOWLEDGEMENTS

First and foremost, I would like to express my sincere gratitude to my research supervisor, Pr. Frédéric Leblond, for his invaluable support, encouragement, and enthusiasm throughout this work. His approach to supervision allowed me the freedom to explore ongoing projects independently while providing insightful guidance when needed. This balance of trust and direction was a fundamental aspect of the success of this project. I would also like to thank him for offering me the opportunity to work on such a significant project, which has taught me a great deal.

I would like to thank Dr. Moujahed Ladibi for his enthusiastic collaboration, his precious time, and his deep interest in research, all of which were crucial to the clinical study's success. I would also like to thank Dr. Félix Janelle for his time, generosity, and the invaluable anatomical knowledge he shared with me. My gratitude extends to all the medical staff at the CHUM who made this work possible, particularly the operating room staff for their patience and invaluable assistance.

I would like to thank all my colleagues at the Lumed lab and express particular gratitude to: Guillaume Sheehy for his remarkable work, which made much of what was achieved in this project possible. I appreciate the time he took to help and explain ideas and concepts, as well as his insightful guidance in solving problems; Trang Tran for her help regarding redaction and organization of administrative tasks; Frédérick Dallaire for his supervision in the application of machine learning and his help in building my current knowledge; and David Orlando Grajales Lopera for his assistance and the numerous hours he spent with me in the operating rooms.

Lastly, I would like to extend a special thanks to Anaïs, who greatly assisted with the writing of this work, by offering emotional support and valuable revisions.

RÉSUMÉ

La résection chirurgicale est une des principales options de traitement des tumeurs parasellaires, notamment des adénomes hypophysaires situés à la base du crâne. La chirurgie transsphénoïdale endoscopique permet l'ablation des tumeurs par les cavités nasales, grâce à une visualisation endoscopique et à des instruments spécialisés. Identifier et délimiter les tumeurs avec précision est un défi majeur, mais essentiel, l'objectif étant d'obtenir une résection complète tout en limitant les dommages aux structures normales avoisinantes. Les techniques d'imagerie préopératoire, telles que l'imagerie par résonance magnétique (IRM), permettent de visualiser les tumeurs. Néanmoins, il n'existe actuellement aucune technologie péropératoire largement accessible permettant un diagnostic en temps réel des adénomes hypophysaires en dehors des cadres de recherche.

Cette thèse vise à développer une technique de diagnostic peropératoire pour aider les chirurgiens à effectuer une résection sécuritaire et efficace des adénomes hypophysaires et autres tumeurs dans cette zone complexe. La solution proposée est une sonde de Spectroscopie Raman (RS), conçue pour s'intégrer aux protocoles opératoires actuels de la chirurgie transsphénoïdale, permettant ainsi l'analyse en temps réel des structures anatomiques de la région parasellaire, incluant les adénomes.

La sonde endonasale RS a été conçue pour permettre une interrogation pratique, sécuritaire et minimalement invasive des tissus. Avant son déploiement clinique, la sonde a été évaluée dans une étude animale impliquant six têtes d'agneaux et 274 mesures spectroscopiques *in situ* sur des structures parasellaires. Des modèles d'apprentissage automatique binaires ont été entraînés, validés et testés pour discriminer la glande hypophysaire des autres structures, évaluant ainsi la capacité de la sonde à distinguer la glande de tissus moléculairement distincts. De plus, un modèle multi-classe a été développé pour différencier quatre structures, démontrant son potentiel pour la guidance chirurgicale. Tous les modèles ont atteint une sensibilité et une spécificité de 100 % sur des mesures de structures provenant d'individus non inclus dans les données d'entraînement.

Afin de préparer l'application clinique, des améliorations ont été apportées au système RS, notamment le développement d'un nouveau module de contrôle laser avec son interface utilisateur dédiée. Une expérience a été menée pour évaluer et minimiser l'impact de la lumière blanche endoscopique sur les mesures de la sonde. Le filtrage passe-bas a permis de réduire efficacement les interférences lumineuses de plusieurs ordres de grandeur, les ramenant à des niveaux comparables au bruit typique ; toutefois, la compatibilité du prototype créé avec le

système chirurgical reste un problème.

Une étude clinique a été lancée, soutenue par un protocole éthique comprenant des protocoles d'acquisition conçus pour une collecte de données rapide, sécuritaire et efficace en salle d'opération. Des mesures de spectroscopie Raman ont été obtenues lors de huit résections transsphénoïdales de tumeurs. Les premières analyses spectrales ont révélé des signatures Raman distinctes et des variations de fluorescence entre les types de tissus. Les tissus hypophysaires ont montré des signaux Raman intrinsèquement faibles en raison d'une fluorescence intense, une limitation non observée dans d'autres tumeurs ou tissus normaux. Des défis clés, notamment les interférences lumineuses endoscopiques et la contamination sanguine, ont été identifiés et évalués, soulignant la nécessité d'un filtrage optique compatible avec les systèmes chirurgicaux et d'une automatisation de la détection de sang.

Cette recherche pose les bases du déploiement clinique de la spectroscopie Raman en tant que système de support décisionnel peropératoire en temps réel, promettant des interventions chirurgicales transsphénoïdale sur les adénomes hypophysaires plus sécuritaires et plus efficaces.

ABSTRACT

Surgical resection is a primary therapeutic option for parasellar tumors, including pituitary adenomas, located at the skull base. Endoscopic transsphenoidal surgery allows for tumor removal through the nasal cavities using endoscopic visualization and specialized instruments. Accurate identification and delineation of the tumor is challenging yet crucial, as the objective is to achieve gross total resection while minimizing damage to surrounding normal structures. Although preoperative imaging techniques, such as Magnetic Resonance Imaging (MRI), enable tumor visualization, no widely available intraoperative technique currently provides real-time pituitary adenoma diagnosis beyond the point of research development.

The thesis aims to develop an intraoperative diagnosis technique to assist surgeons in the safe and effective resection of pituitary adenomas and other tumors in this critical area. The proposed solution is a Raman Spectroscopy (RS) probe that can be integrated with current transsphenoidal surgery workflows, enabling real-time interrogation of parasellar anatomical structures, including adenomas.

The endonasal RS probe was designed to enable practical, safe, and minimally invasive tissue interrogation. Before clinical deployment, the probe was evaluated in an animal study involving six lamb heads and 274 *in situ* spectroscopic measurements of parasellar structures. Binary machine learning models were trained, validated, and tested to discriminate the pituitary gland from all other structures, assessing the probe's ability to distinguish the gland from molecularly distinct tissues. Additionally, a multiclass model was developed to differentiate between four structures, demonstrating the potential for safe surgical guidance. All models achieved 100% sensitivity and specificity on structures from individuals not included in the training data.

To prepare for clinical application, improvements were made to the RS system, including the development of a new laser control module with its designated user interface. An experiment was conducted to evaluate and minimize the impact of the endoscopic white light on the probe's measurements. Short-pass filtering effectively reduced light interference by multiple orders of magnitude, bringing it to levels comparable to typical noise; however, the prototype's compatibility with surgical systems remains an issue.

A clinical study was initiated, supported by an ethics protocol including acquisition protocols designed for rapid, safe, and efficient data collection in operating rooms. RS measurements were acquired during height transsphenoidal tumor resections. Initial spectral analysis revealed distinct Raman signatures and fluorescence variations across tissue types. Pituitary

tissues exhibited inherently weak Raman signals, due to intense fluorescence, a limitation not observed in other tumors or normal tissues. Key challenges, including endoscopic light interference and blood contamination, were identified and evaluated, underscoring the need for light filtering compatible with surgical systems and automation in blood detection.

This research sets the foundation for the clinical deployment of Raman spectroscopy as an intraoperative real-time decision support system for safer and more effective transsphenoidal surgeries, such as pituitary adenoma resections.

TABLE OF CONTENTS

LIST OF TABLES

LIST OF FIGURES

LIST OF SYMBOLS AND ACRONYMS

ACTH	Adrenocorticotropic Hormone
AEC	Automatic Exposure Control
ANN	Artificial Neural Network
CCD	Charged-Couple Device
CHUM	Centre Hospitalier de l'Université de Montréal
CNN	Convolutional Neural Network
CNS	Congress of Neurological Surgeons
CT	Computed Tomography
CW	Continuous-Wave
GH	Growth Hormone
GTR	Gross Total Resection
GUI	Graphical User Interface
iCT	Intraoperative Computed Tomography
ICG	Indocyanine Green
iMRI	Intraoperative Magnetic Resonance Imaging
IOUS	Intraoperative Ultrasound
KNN	k-Nearest Neighbor
LDA	Linear Discriminant Analysis
LH	Luteinizing Hormone
LSRM	Line Scan Raman Microspectroscopy
MPE	Maximal Permissible Exposure
ML	Machine Learning
MPM	Multi-Photon Microscopy
MSE	Mean Squared Error
MRI	Magnetic Resonance Imaging
NIR	Near-Infrared
OCT	Optical Coherence Tomography
OD	Opical Density
PCA	Principal Component Analysis
PRL	Prolactin
QDA	Quadratic Discriminant Analysis
QF	Quality Factor
ROC	Receiver-Operating Characteristic

RS	Raman Spectroscopy
SAM	Spectral Angle Mapper
SERDS	Shifted excitation Raman difference spectroscopy
SBR	Signal-to-Baseline Ratio
SNR	Signal-to-Noise Ratio
SNV	Standard-Normal-Variate
SP	Short-Pass
SVM	Support Vector Machine
TG	Time-Gating
TS	Transsphenoidal surgery
TSH	Thyroid-Stimulating Hormone

LIST OF APPENDICES

CHAPTER 1 INTRODUCTION

1.1 Context

Pituitary adenomas are intracranial tumors that can be resected through the nasal cavities during endoscopic transsphenoidal surgeries. Precise tumor discrimination and delimitation are crucial for achieving optimal surgical outcomes [1]. The instrument developed in this thesis aims to improve this process by providing intraoperative molecular-based differentiation of anatomical structures.

1.1.1 Pituitary adenomas

The pituitary gland, located at the skull base in the sellar region, is an organ that controls several vital endocrine functions. It comprises two parts: the anterior lobe (adenohypophysis) and the posterior lobe (neurohypophysis), as illustrated in Figure 1.1. The anterior pituitary secretes a range of hormones, including growth hormone (GH), adrenocorticotropic hormone (ACTH), thyroid-stimulating hormone (TSH), gonadotropin (LH), and prolactin (PRL). The posterior pituitary releases hormones synthesized in the hypothalamus [2]. These hormones regulate the function of many organs, including glands, skin, muscles, bones, ovaries, thyroid, kidneys, and others [2]. Each hormone is produced by a distinct cell line, each of which potentially gives rise to a different type of tumor. Tumors originating from the pituitary gland are collectively known as pituitary adenomas.

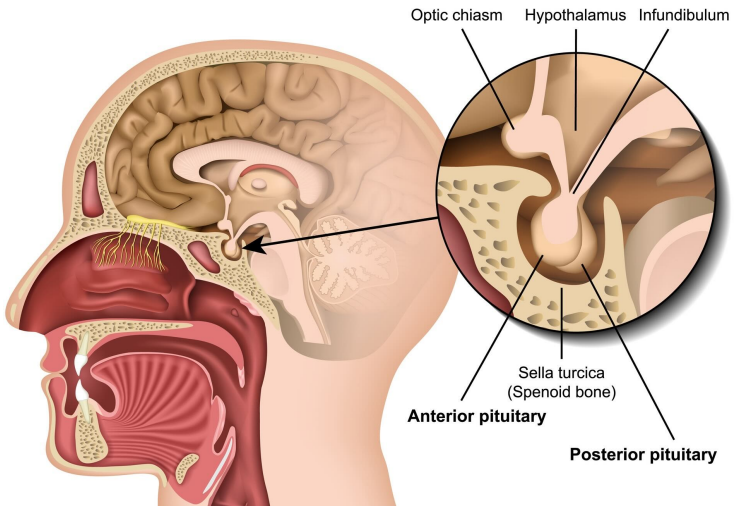

Figure 1.1 Pituitary anatomy. Reprinted from [3] with permission

Pituitary adenomas represent approximately 15% of intracranial tumors and occur in 10% of the population, with the majority remaining harmless and undiagnosed during life [4, 5]. While they can be classified using various complex systems, they are more easily categorized based on their functionality (hormone-secreting), the specific hormone they produce if functioning, and their size [4, 6]. Functioning adenomas secrete excessive amounts of hormones, disrupting normal endocrine regulation, and account for two-thirds of all tumors, secreting PRL, GH, and ACTH in decreasing order of frequency [4]. The remaining third are non-functioning adenomas. Based on their size, adenomas are classified as macroadenomas if they are larger than 1 cm and microadenomas when smaller than this threshold [4, 7].

The effects and manifestations on the patients' health vary based on the tumor's size, location, and whether it is functioning. These effects can be classified into two broader categories: local mass effects and endocrine (hormonal) dysregulation. Local mass effects refer to the excessive pressure applied to surrounding anatomical structures due to tumor growth, particularly in cases of macroadenomas. Compression of nerves, such as the optic chiasm, can lead to vision impairment, loss of peripheral vision, headaches, and, in severe cases, neurological deficits. Functioning adenomas lead to different syndromes depending on the specific overproduced hormone [4, 7], such as:

- Prolactinomas: overproduction of prolactin (PRL) results in galactorrhea, amenorrhea in women, and erectile dysfunction, as well as decreased libido in men.
- Acromegaly and gigantism: excessive production of growth hormone (GH) results in acromegaly in adult patients, presenting characteristic growth in facial features, hands, and feet. Children develop gigantism with abnormal body size growth.
- Cushing's disease: corticotroph adenomas secrete adrenocorticotropic hormone (ACTH), which causes hypertension, central body obesity, and facial roundness.

Pituitary adenoma diagnosis is based on a complementary analysis of clinical assessments of symptoms, hormonal testing, and advanced imaging. Symptoms related to hormonal imbalances and local mass effects, such as vision impairment and headaches, are usually followed up with biochemical and hormonal testing to assess the secretory activity of the adenoma [7]. Magnetic Resonance Imaging (MRI) is the gold standard for visualization, localization, and assessment of potential invasion of surrounding tissues [8]. Computed Tomography (CT) can be an alternative imaging modality, though it is less sensitive to detect microadenomas due to its poorer resolution [1].

1.1.2 Surgical treatment

Treatment options include surgery, medical therapies, and radiotherapy. Transsphenoidal surgery (TS) is typically the first-line treatment, except for prolactinomas, for which hormonal therapy is often prescribed unless these medications are contraindicated [9]. During transsphenoidal endoscopic resection surgery, pituitary adenomas and other tumors of the sellar region are removed through the nasal cavity and the sphenoid sinuses, using a rigid endoscope, illustrated in Figure1.2 [10]. The endoscope is used for visualization while the patient is under general anesthesia. During the procedure, the anterior wall of the sphenoid sinus is identified and removed with specialized instruments. Subsequently, any residual septations within the sinus are cleared to provide access to the sella turcica, the bony structure enclosing the pituitary gland. The bony wall of the sella (sellar floor) is meticulously removed with drills or punches, and the dura mater is incised to expose the pituitary gland and the tumor. The tumor is then removed in pieces using micro-instruments or suction devices. This approach has become the standard for most pituitary adenomas and lesions confined to the sella turcica because of its precision, safety, and minimal invasiveness [11, 12].

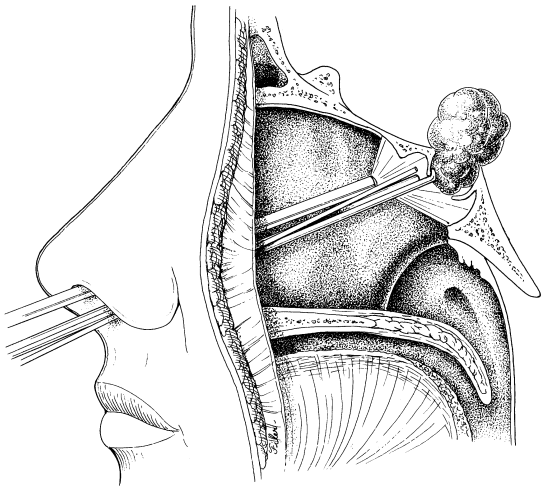

Figure 1.2 Schematic drawing of endoscopic transsphenoidal surgery of a pituitary adenoma through a nostril. Two surgical instruments are inserted parallel to the endoscope. Reprinted from [10] with permission.

1.1.3 Clinical challenges of transsphenoidal resection surgery

During surgical resection of the pituitary adenoma, the accurate identification and delineation of the tumor is crucial, as the objective is to achieve Gross Total Resection (GTR) of the

tumor while limiting damage to the surrounding normal structures. Achieving gross total resection safely is critical for local tumor control, as residual tumor volume significantly influences the likelihood of recurrence, potentially requiring further treatment and increasing the risk of early mortality [13, 14]. In contrast, unwanted resection of normal (healthy) tissue is dangerous for the patient. Resection of normal pituitary gland tissue may result in hormonal imbalances and diabetes insipidus, an incurable condition in which the body can't balance its fluid levels. [15] Studies estimated that 16% of patients undergoing surgery presented signs of postoperative diabetes insipidus, with up to 12.5% of patients having the disease permanently [16, 17].

Accurate tumor resection is complicated by the heterogeneity of pituitary adenomas in subtypes, size, structure, and growth patterns. While different subtypes can vary greatly in compositions and structures, different sizes are associated with different surgical challenges. Microadenomas are often more difficult to localize, while macroadenomas are associated with greater risks of incomplete tumor resection [8, 13]. To further complicate tumor resection, invasion of surrounding parasellar tissues, such as the cavernous sinus and the dura mater, may also occur. Tumor invasion has been associated with a higher prevalence of residual tumor [18]. Roughly one in three patients undergoing TS for non-functioning macroadenomas will have an incomplete resection [15].

Currently, preoperative MRI allows tumor visualization prior to the intervention and is also used during the surgery as a navigation tool. Intraoperative lesion sampling, followed by histopathological analysis, confirms the tumor presence and allows for precise classification. However, the immunohistochemistry panel requires time to react with the tissue section, and the pathologist must evaluate the results before a diagnosis can be made on a tissue that has already been resected. Various detection and imaging techniques are currently under development to allow real-time intraoperative diagnosis and delineation [1, 19]. Nonetheless, neurosurgeons currently rely on visual assessment, supported by preoperative MRI, to determine the nature of uncertain pituitary tissue during surgery, with optimal outcomes reliant on the surgeon's expertise [1, 8].

Another challenge regarding those surgeries is the proximity to critical neurovascular structures, such as cranial nerves and the internal carotid artery. These structures must be carefully navigated during surgery to avoid complications [20]. A comprehensive review of the anatomical structures of the sellar region is depicted in Appendix A.

Those clinical challenges highlight the need for an intraoperative tool that can differentiate pituitary adenomas from normal tissues, and a tool capable of identifying structures within the parasellar region to ensure safe transsphenoidal surgeries. Such a tool could enable real-

time diagnosis of various other tumors of the sellar region, including craniopharyngiomas, chondrosarcomas, meningiomas, and cavernomas, which also require accurate intraoperative diagnosis due to their low GTR rates and high recurrence risks [6].

1.2 Research hypotheses and objectives

This project, conducted within the *Lumed Lab*, focuses on the development and validation of a hand-held endonasal Raman spectroscopy probe for *in vivo* pituitary adenoma diagnosis during surgery. Raman spectroscopy, incorporated into a fiber-optic probe capable of accessing the pituitary gland and other structures of the sellar region, could offer a promising solution to various clinical challenges currently faced in surgery. The choice of this solution is based on the following hypotheses:

- **Hypothesis 1**: Intraoperative contact Raman spectroscopy allows fast, reliable, and accurate molecular characterization. This can assist surgeons in distinguishing abnormal tissues from normal structures or identifying normal structures for surgical navigation.
- **Hypothesis 2**: A Raman spectroscopy system can be seamlessly integrated within current transsphenoidal surgery workflows without causing significant disruptions or delays.

Accordingly, the following objectives have been established:

- **Objective 1**: Design and develop a Raman spectroscopy probe for use during endoscopic transsphenoidal surgeries and validate its potential for machine learning-based molecular tissue characterization in animals.
  - **Sub-objective 1.1**: Develop a Raman spectroscopy probe that enables practical interrogation of parasellar structures and is compatible with existing endoscopic systems.
  - **Sub-objective 1.2**: Validate the probe's classification performance in a preclinical animal study by accurately distinguishing intracranial anatomical structures in the parasellar region using classification models for *in situ* spectral measurements.
- **Objective 2**: Improve and integrate a Raman spectroscopy system in endoscopic transsphenoidal surgeries for safe, time-efficient, and practical use during tumor resection procedures.

- **Objective 3**: Acquire Raman spectroscopy measurements of parasellar structures, including pituitary adenomas and healthy pituitary glands, in human patients during a clinical study to assess its feasibility.

1.3 Thesis outline

This thesis includes 6 chapters, including this introduction. A comprehensive review of the clinical challenges and opportunities, discussed in Chapters 1 and 2, has been realized in a dedicated review paper [21], titled *"Challenges and opportunities for new intraoperative optical techniques in the surgical treatment of pituitary adenomas"*, in collaboration with *Félix Janelle* (neurosurgery resident, CHUM). The paper was submitted to the *Journal of Biomedical Optics* on November 12, 2024.

Chapter 2 presents a literature review covering the current state and development of intraoperative detection of pituitary adenomas. It subsequently covers Raman spectroscopy, its application to cancer diagnosis, and its integration into fiber-optic probes, as well as the use of machine learning for Raman spectra classification. Chapter 3 presents a research article covering the development of the hand-held endonasal probe and its preclinical evaluation focused on classifying intracranial tissues in animals with Machine learning (ML) models. Chapter 4 presents the integration of a Raman spectroscopy system in surgery. It covers the contributions to the modernization of the *Lumed Lab* Raman spectroscopy systems, as well as the challenges associated with the integration. Chapter 5 presents the preliminary results of the clinical study, acquiring Raman spectra of multiple tumors and healthy tissues in human patients during surgery. The last chapter covers the important results, limitations, and the project's future.

CHAPTER 2 LITERATURE REVIEW

This literature review examines current imaging and detection techniques for pituitary adenomas and reviews the modalities developed for intraoperative detection and imaging. Subsequently, it explores Raman spectroscopy, its application to biological samples, cancer diagnosis, and specifically pituitary adenomas. The integration of the technology into fiber-optic probes is then covered. Finally, the last section provides a foundational understanding of machine learning classification techniques that can be used for tissue characterization using Raman spectroscopy.

2.1 Intraoperative imaging and diagnosis techniques of pituitary adenomas

2.1.1 Current imaging and diagnosis techniques

As briefly discussed in the introduction, two primary methods currently assist neurosurgeons in localizing and delineating pituitary adenomas: MRI-guided neuronavigation and histopathological analysis of the first resection.

Preoperative MRI is the gold-standard imaging technique for tumor visualization and delimitation before surgery [8]. While essential for diagnosis, MRI is typically performed again a few hours before the procedure, once the patient's head is fixed in place, to provide a detailed map of the tumor and its location. This approach offers several advantages, including high-resolution 3D imaging, precise anatomical detail, and assessment of the tumor's relationship with surrounding structures.

The latest preoperative imaging also enables intraoperative MRI-guided neuronavigation using infrared cameras or electromagnetic sensors to track surgical instruments in real time. These instruments are then visible on the MRI-based 3D images displayed on monitors, providing real-time feedback of the instrument's position along with the endoscopic video feed, illustrated in Figure 2.1. This integrated guidance allows safer navigation through the cavities and toward the tumor. It has been shown that neuronavigation-guided surgeries increase the rates of GTR and reduce the incidence of postoperative complications [22]. An international pilot questionnaire-based study revealed that over 75% of leading academic neurosurgeons believe neuronavigation expands the scope of neuroendoscopic procedures, allowing operations that were previously judged as inoperable [23].

However, MRI-guided neuronavigation has some limitations, including constraints of MRI imaging itself and inaccuracies with the anatomy of the patient in real time. Conventional

(a) 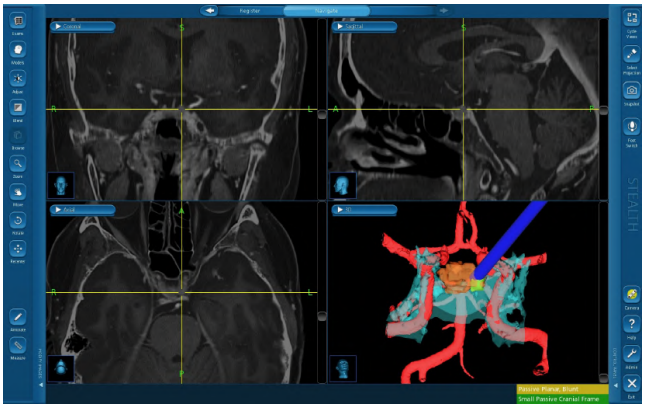

(b) 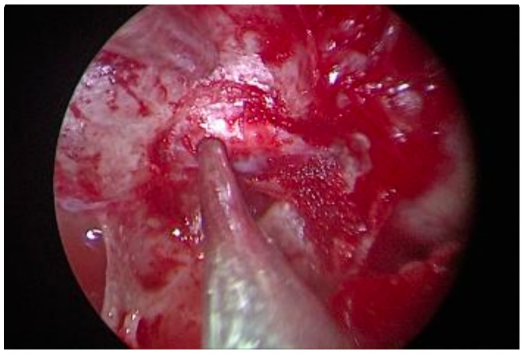

Figure 2.1 Screen captures of the live displays used to guide transsphenoidal surgery. a) Preoperative MRI: 2D views of the 3D scan and neuronavigation representation of an instrument in dark blue on the preoperative reconstruction. The normal gland is shown in orange, the adenoma in lime green, the cavernous sinus in light blue, and the arteries in red. b) Endoscopic image showing the instrument with its tip on the pituitary gland.

3 Telsa MRI has limited sensitivity for detecting pituitary adenomas. Its resolution leads to radiological uncertainties in the assessment of microadenomas [24], and it is also occasionally unsuccessful in definitively identifying the site of de novo, persistent, or recurrent tumor [8]. For neuronavigation, accuracy is affected by many factors, with registration errors likely playing the most significant role [25]. The instrument is represented on a static MRI image, representing the patient's anatomy as it was before surgery, not during. Tissue movement and gradual resection of the tumor cause discrepancies with the preoperative image. This technique provides spatial orientation but lacks real-time tissue differentiation.

Histopathological analysis remains the gold standard for characterizing pituitary gland tissue. Examining tumor cells microscopically confirms malignancy, grades the tumor, and offers insights into its biological behavior [6]. During surgery, an initial sample of the lesion is resected, frozen, and sent for histopathological analysis to confirm tumor presence. Intraoperative diagnosis using frozen sections presents high concordance rates (up to 90-95%) with the definitive histopathological diagnosis [26]. However, this process is time-consuming during surgery, requiring sample transport, immunohistochemical staining, and pathologist examination before a diagnosis can be made. Moreover, since the diagnosis is made on already resected tissue, it does not provide an assessment before removal, which could impact the surgical decision-making.

While preoperative imaging and diagnostic techniques provide valuable guidance, surgical decision-making for tissue resection ultimately relies on the neurosurgeon's visual assessment, distinguishing tumor tissues from normal glands based on morphology and color. Intraop-

erative decisions are based on the surgeon's expert training or, at times, made reactively through trial and error [19]. Optimal outcomes in tumor resection, hormonal correction, and complication reduction are obtained in high-volume centers with sufficiently experienced and specialized surgeons [1]. Therefore, a real-time intraoperative tool capable of reliably distinguishing *in vivo* pituitary adenomas from normal structures is needed to support surgical decision-making.

2.1.2 Modern and new intraoperative detection techniques

Various intraoperative techniques have been developed and continue to be tested in operating rooms to distinguish pituitary adenomas [1, 19, 27], including:

Intraoperative magnetic resonance imaging (iMRI)

Intraoperative MRI consists of performing MRI scanning of residual tumor volume during the resection by incorporating a scanner in a surgical setting. First implemented at the Brigham and Women's Hospital in Boston in 1994 [28], this technique has shown utility in detecting unexpected residual tumors and can increase the likelihood of achieving GTR by up to 40% [29, 30]. Despite these improvements, iMRI is not a standardized method, nor is it available in most surgical centers [19, 31]. Its cost-effectiveness and prolonged scan times present significant challenges. The high-cost integration of iMRI requires specialized infrastructure, including shielded surgical suites and advanced equipment to maintain sterility and imaging accuracy, which has limited its widespread use [31]. Additionally, it is estimated that the surgical workflow is interrupted for 30 minutes to obtain images for each scan [30], overextending overall operating time and prolonging general anesthesia [29, 31]. While high-field MRI enhances resolution and reduces acquisition times, it also entails significantly higher costs [1, 24, 29]. Recent guidelines by the Congress of Neurological Surgeons (CNS) do not recommend iMRI for estimating residual tumors due to its reported variable false-positive rate [32].

Intraoperative computed tomography (iCT)

Intraoperative CT (iCT) provides cross-sectional images of the surgical area during the procedure using X-rays and computer processing. While the literature on the use of iCT for pituitary adenomas is sparse, a recent study explored it for the resection of challenging large and giant adenomas [33]. The imaging technique has shown utility in increasing the extent of resection and helped accurately convey prognosis. Similar to iMRI, it faces the limitation

of being costly and challenging to integrate into a surgical room. It requires an expensive lead-shielded operating theater without any staff to minimize radiation exposure. The total time between stopping to initiate scanning and resuming surgery is approximately 10–12 minutes [33]. Although its integration cost is lower than that of iMRI, iCT is associated with reduced resolution and involves the administration of minimal radiation doses to the patient [1, 33].

Intraoperative ultrasound (IOUS) probes

Over the years, hand-held ultrasound probes have been developed to aid pituitary adenoma localization and improve operation safety [34, 35]. They utilize high-frequency sound waves to create images of internal body structures. Although various prototypes were realized to access the parasellar region, some were too large to safely enter the sphenoid sinuses [34, 36]. Successful designs have proven effective in guiding safer surgeries, with neurosurgeons reporting their usefulness [34]. Nonetheless, their effectiveness in detecting pituitary adenomas has not been established, and CNS guidelines did not find enough evidence to recommend their use [32]. However, recent technological improvements in ultrasound have enabled probe miniaturization. A newly developed probe has shown promising results by increasing the GTR rate while decreasing blood loss and operative times [37]. The single-use, sterile, bayoneted, side-firing instrument, illustrated in Figure 2.2, features a 2.87 mm diameter and a 10-mm scanning head, specifically designed for transsphenoidal surgeries [37].

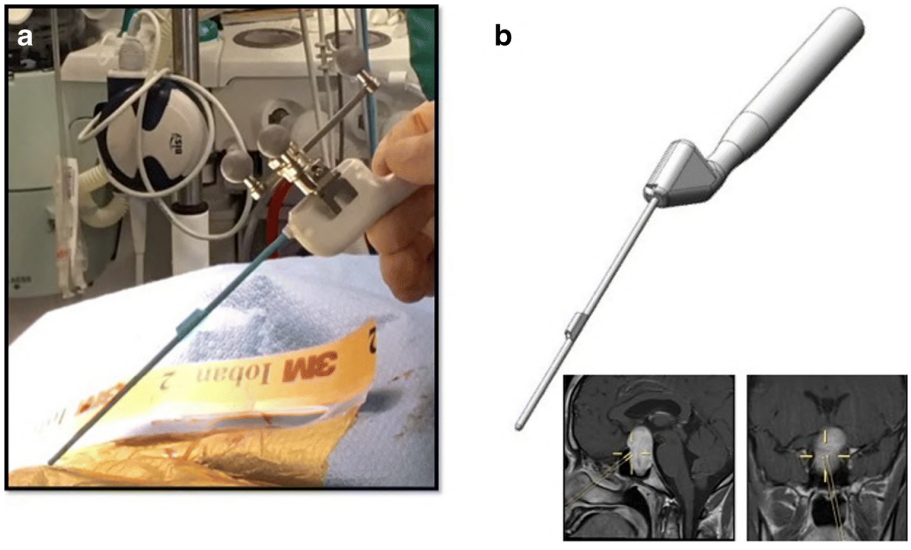

Figure 2.2 a) Intraoperative IOUS probe and its simultaneous use in neuronavigation for guidance (see MRI images bottom right). b) 3D model of the ultrasound probe. Reprinted from [37] with permission.

Elastography

Recently, interest in studying the mechanical properties of human tissues at subcellular resolution has grown, fueled by evidence that cell-scale tissue mechanics influenced tumor progression [38]. The distinctive micromechanical signature of pituitary adenoma tissue provides new perspectives on intraoperative diagnosis. Atomic force microscopy measurements of human specimens showed that adenoma tissues are two orders of magnitude softer than normal tissues, independent of the type of hormonal secretion, thus tumor subtype [39]. This significant difference in softness suggests that intraoperative interrogation could be evaluated by an elastography probe performing stiffness analysis [39].

Fluorescence-guided endoscopy

Fluorescence imaging has been explored to improve visualization and facilitate the identification of adenomas. Preoperative administration of fluorophores with preferential uptake in tumoral cells, such as Indocyanine green (ICG), enhances contrast with normal glands compared to white-light endoscopic visualization [40]. The difference in fluorescence emission between the tumor and the pituitary gland appears useful for facilitating tumor resection from 15 to 90 minutes after ICG administration [41]. Conversely, higher emission of the normal pituitary gland can be exploited to differentiate it from the tumor showing less fluorescence with NIR visualization, as illustrated in Figure 2.3 [41].

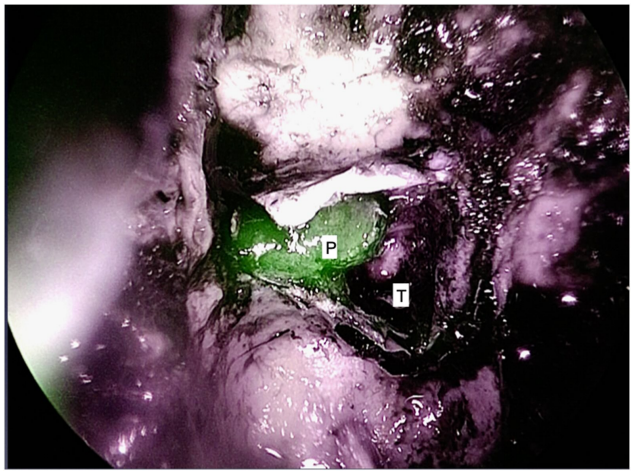

Figure 2.3 Near-infrared (NIR) fluorescence-guided endoscopy. NIR fluorescence in the normal pituitary gland (P) can be detected (green), with tumor (T) showing low fluorescence (dark) at 180 minutes from administration in a patient. Reprinted from [41] with permission.

A key challenge lies in the fact that fluorophores differ in uptake and emission across various

types of adenomas. However, second window ICG appears to be a promising option for use in all pituitary adenomas, regardless of their secretory status [42]. This technique is time-sensitive, providing enhanced contrast only for a limited period, which may not align with the demands of the often complex surgical workflows. Additionally, integrating the equipment and agents in this workflow is challenging and a limitation to its widespread use [40].

Contact endoscopy

The introduction of rigid endoscopes modernized transsphenoidal surgeries by virtually introducing the eyes of the surgeon into the sphenoid sinus or tumor cavity [1]. Enhanced endoscopic techniques have been investigated for performing real-time *in vivo* differentiation of adenomas based on tissue vascularity [43]. Contact endoscopy is a minimally invasive technique that enables the observation of microstructures by making close contact with the tissue. Although further validation in larger studies is necessary, the visualization of tissue vascularity through contact endoscopy emerges as a promising marker for distinguishing normal pituitary glands from adenomas [43].

General discussion

The various diagnostic techniques developed in recent years highlight the growing need to provide solutions for clinical challenges. Techniques aimed at discriminating pituitary adenomas are also being developed and utilized for safe surgical navigation and tissue mapping during transsphenoidal surgeries [1, 19]. Guidelines from neurosurgical congresses emphasize that the extended surgical time with the patient under anesthesia should be minimized and that the accuracy of the technique should be high enough to justify any increase in surgery duration [32]. An ideal diagnostic technique should be minimally invasive, capable of detecting microadenomas, and effective across all pituitary adenoma subtypes. Ideally, it should also be adaptable for detecting other tumors in the parasellar region.

2.2 Raman spectroscopy

For the past few years, optical spectroscopy and imaging technologies have seen a steady increase in their biomedical use, with notable improvements in accuracy and specificity [44]. These techniques can provide insight into the metabolic and pathological states of tissues through the analysis of light interactions, allowing minimally invasive detection. One of these techniques is Raman spectroscopy, characterized by its high molecular specificity, high spatial resolution, and non-destructive nature [44, 45]. These qualities make Raman spectroscopy a strong candidate for intraoperative diagnosis, offering molecular-level tissue differentiation that could aid in the detection of parasellar tumors and provide surgical tissue mapping.

2.2.1 Raman scattering

Raman scattering is a fundamental optical phenomenon that arises when light interacts inelastically with matter. It was first observed in 1928 by C.V. Raman and K.S. Krishnan [46]. When a photon of frequency ω_0 and energy $E_0 = \hbar\omega_0$ is scattered by a molecule with a vibrational mode of energy E_p. The electromagnetic field of the incident photon interacts with the molecule by inducing a temporary dipole moment, which distorts the electron cloud around the nuclei. The photon is said to be absorbed by the molecule in a short-lived unstable state of the molecule ($\sim$5 fs) [47]; *a virtual state*. The molecule then re-emits a photon in a random direction, radiating the excess energy. This process is known as scattering. In most occurrences, the scattered photon has the same energy as the incident photon, referred to as *Rayleigh* scattering.

C.V. Raman and K.S. Krishnan observed a rare change in the wavelength ω_0 of the scattered photon, now known as Raman scattering. This inelastic scattering occurs in approximately 1 out of 10 million scattering instances and involves a change in the vibrational state of the molecule, leading to a shift in the energy of the scattered photon. Unlike Rayleigh scattering, the inelastically scattered photon carries vibrational information from the molecule it interacted with. If the incident photon transfers energy to the molecule, exciting its vibrational state and resulting in a scattered photon with lower energy, the process is called *Stokes* Raman scattering. Conversely, if energy is transferred from the molecule to the photon, increasing its energy, the process is known as *anti-Stokes scattering*. Since, at body temperature, most molecules are in the ground state rather than in a thermally excited state, Stokes scattering is more likely than anti-Stokes scattering [48]. These phenomena, along with other key light-matter interactions, are illustrated in the Jablonski diagram in Figure 2.4.

Absorption, fluorescence, Rayleigh scattering, and specular reflection are competing processes

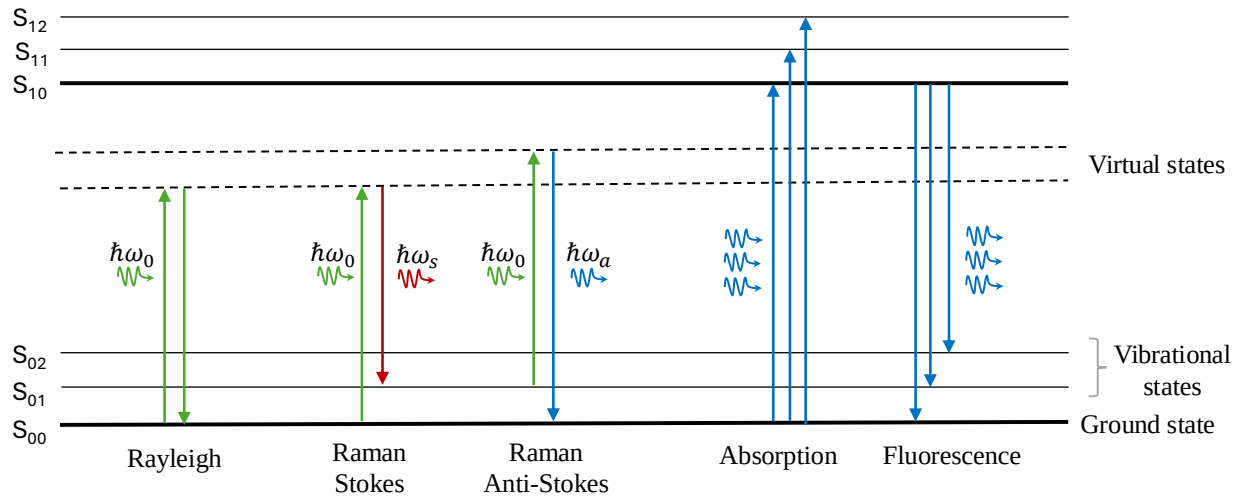

Figure 2.4 Jablonski diagram of the principal light-matter interactions.

of Raman scattering and must be considered when designing a Raman spectroscopy system. A Raman spectrum represents the superposition of all photons that have interacted with the vibrational modes of a molecule. As a result, Raman spectral peaks appear as narrow bands at specific energies, corresponding to molecular vibrational modes and providing detailed information about molecular bonds and symmetry. For Stokes scattering, the energy shift is expressed as:

$$E = \hbar(\omega_0 - \omega_s) = hc(\frac{1}{\lambda_0} - \frac{1}{\lambda_s}) = hc\Delta\omega \tag{2.1}$$

where λ_0 is the wavelength of the incident photon and λ_s is the re-emitted Stokes photon. Raman spectra are typically plotted in terms of energy shift rather than absolute wavelengths, as vibrational state transitions involve relatively small energy changes. Raman shifts are expressed in cm^{-1}:

$$\Delta\omega[cm^{-1}] = 10^7(\frac{1}{\lambda_0[nm]} - \frac{1}{\lambda_s[nm]}) \tag{2.2}$$

A consequence of the equation is that the width of the Raman peaks is directly influenced by the width of the excitation source. Therefore, Raman excitation sources must have a narrow emission wavelength and stable power output to achieve high-resolution spectra. Since Raman scattering is such a rare phenomenon, high power density sources, such as lasers, are required to generate sufficiently strong Raman signals. However, this also significantly in-

creases Rayleigh scattering, since only about 1 in 10^7 scattered photons will undergo inelastic scattering. To isolate the Raman signal, a high-pass filter centered at the laser's wavelength must be used to block Rayleigh scattered light before it reaches the spectrometer.

Each peak in a Raman spectrum represents a vibrational transition of the molecules present in the illuminated sample. The Raman spectrum region from 400 to 1800 cm^{-1} is known as the *fingerprint* region, rich in vibrations unique to particular molecular structures. This region is widely used for the analysis of biomolecular tissues due to its specificity [45]. The region from 2400 cm^{-1} to 3800 cm^{-1}, called the *high wavenumber* region, is simpler, with fewer peaks and broader bands. It has also been explored to provide tissue characterization and can be beneficial for samples where the fingerprint region is highly congested or not as informative [49].

2.2.2 Fluorescence

Fluorescence is a competing process that is difficult to filter when measuring Raman signals due to its similar laser-based excitation mechanism and broadband emission spectrum. Absorption occurs when a photon transfers energy to a molecule, exciting it from the ground state S_0 to an excited electronic state S_1 if the photon energy matches the energy difference between these states (Fig. 2.4). After excitation, vibrational relaxation occurs, allowing the molecule to transition from a higher vibrational state to the lowest vibrational level S_{10}. The absorbed energy can then be released with the emission of another photon. This process, known as fluorescence, corresponds to the emissions of lower-energy photons, similar to Stokes scattering. The emitted photons of both processes have longer wavelengths than those of the excitation source. This overlap makes it difficult to filter fluorescence from the desired Raman signal. However, unlike Raman scattering, fluorescence produces a broader emission spectrum due to the many possible vibrational levels to transition to, leading to a wider range of emitted photon wavelengths. This particular distinction can be exploited to differentiate between both signals, as explained in the following section 2.2.8.

2.2.3 Raman spectroscopy of biological samples

Performing Raman spectroscopy on biological samples is significantly more challenging than on organic minerals or single-molecule compounds. Biomolecular samples contain a vast number of molecular species with diverse bonds and complex structures, leading to a multitude of Raman peaks. Consequently, the Raman signal is weaker compared to simpler molecular structures with fewer peaks, resulting in a significantly lower Signal-to-Noise Ratio (SNR). Additionally, identifying the specific molecular compound responsible for each Raman peak

is complicated by their great number. However, previous studies have helped facilitate this identification process by compiling published Raman spectral interpretations of biological tissues into databases [50]. The Raman spectra of pure molecular constituents of tissues, such as proteins [51], lipids [52], and amino acids [53], can be cross-checked with these databases to assign specific compounds to the peaks of new spectra.

Fluorophores are molecules responsible for fluorescence emission. Biological tissues are naturally composed of many fluorophores, which are responsible for *autofluorescene*, the intrinsic emission from endogenous molecules. Most cellular autofluorescence originates from mitochondria and lysosomes [54]. The great number of biological fluorophores emit a much stronger signal than Raman scattering upon tissue illumination. This phenomenon reduces the Signal-to-Baseline Ratio (SBR) of the Raman peaks by increasing the baseline signal due to the broad emission spectra of the many fluorophores that overlap. The decrease of the SBR in biological samples is illustrated in Figure 2.5 with unprocessed Raman measurements of nylon and pork muscle tissue.

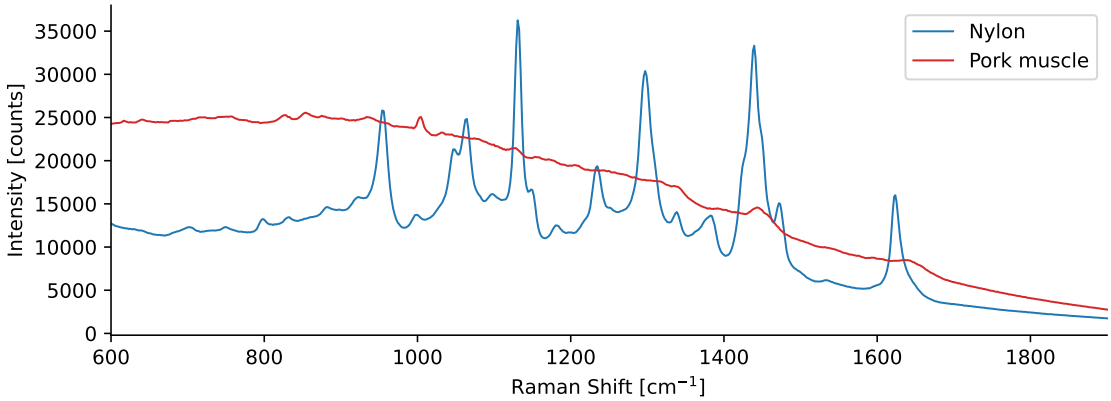

Figure 2.5 Unprocessed Raman signal from nylon compared to pork muscle tissue. Acquisitions were performed with the Raman system presented in the following sections.

For Raman spectroscopy, the Signal-to-Noise Ratio is defined as:

$$SNR_{Raman} = \frac{Raman}{\sqrt{Raman + Noise}} \tag{2.3}$$

while the Signal-to-Baseline Ratio is defined as:

$$SBR_{Raman} = \frac{Raman}{\sqrt{Raman + Baseline\ signal}} \tag{2.4}$$

2.2.4 Selecting the excitation wavelength

When selecting the excitation wavelength, multiple factors must be considered, as the probabilities of light-matter interaction vary throughout the spectrum. To maximize the Raman signal, shorter wavelengths can be used since the Raman scattering cross-section is inversely proportional to the excitation wavelength ($\sigma_{Raman} \propto \frac{1}{\lambda^4}$). This makes UV or short-wavelength visible light attractive for the application since it gives the largest Raman signal from tissue. However, lower wavelengths also increase tissue autofluorescence, as endogenous fluorophores emit primarily between 350 and 600 nm [55]. Moreover, tissue absorption between 700 and 1400 nm is weaker for the principal components of biological tissues [56], reducing the risk of damage from laser exposure. This spectral region, known as the *therapeutic window*, along with the reduced autofluorescence at higher wavelengths, explains why Raman spectroscopy is usually done with Near-Infrared (NIR) lasers in biomedical applications.

2.2.5 Raman spectroscopy for cancer diagnosis and detection

Raman spectroscopy has been investigated for cancer detection during surgery for over 30 years [57], with the aim of helping surgeons achieve complete tumor removal. This application relies on the potential of Raman spectroscopy for tissue characterization based on molecular differences. The decay of healthy tissue towards tumor tissue is associated with molecular changes [58]. By detecting these molecular differences, Raman spectroscopy can help identify new biomarkers to differentiate tumors and healthy tissues. These changes can even be detected at early stages, making Raman spectroscopy a promising technique for early diagnosis and monitoring of cancer progression [57]. Raman spectroscopy is well-suited for *ex vivo* diagnosis on biopsies, as well as *in vivo* diagnosis, as it can be integrated into a fiber-optic probe, which will be covered in section 2.2.7. This technique is non-destructive, minimally invasive, and label-free, as no endogenous contrast agent is needed. Additionally, compared to other spectroscopic methods, Raman spectroscopy provides high molecular specificity, further enhancing its potential for clinical applications [44].

For surgical guidance, Raman probes can be used to perform contact measurements on tissues and organs exposed by open surgeries or integrated into endoscopes and biopsy needles. Studies exploring the utility of the technique for cancer detection have been realized in the brain [59–61], skin [62], lungs [63], ovaries [64], prostate [65], breast [66, 67], and many other structures associated with cancer [57, 68].

2.2.6 Raman spectroscopy of the pituitary gland and adenomas

Multiple studies have explored Raman spectroscopy of pituitary adenomas and normal gland samples. Zhou et al. (2012) investigated resonance Raman spectroscopy to examine several brain tumor specimens obtained during surgical procedures, including pituitary adenomas [69]. The study used a confocal Raman microspectroscopy system using a 532 nm excitation laser to enhance the 1548 cm^{-1} peak. Machine learning (ML) models were developed to discriminate normal brain tissue (i.e. grey and white matter) from all tumors, including pituitary adenomas. Although this demonstrated clinical diagnostic potential, the more relevant challenge in adenoma surgery is differentiating tumors from normal gland tissue.

In 2019, Austrian researchers used confocal Raman microspectroscopy with a translation stage to perform Line Scan Raman Microspectroscopy (LSRM), enabling the discrimination and visualization of pituitary glands and adenomas [70]. LSRM systems use a laser line to capture multiple Raman spectra simultaneously, generating hyperspectral 3D images with a translation stage, where each pixel corresponds to a Raman spectrum. A k-Nearest Neighbor (kNN) classifier achieved 95% accuracy in discriminating between gland tissue and all subtypes and 84–99% between adenoma subtypes. This system was later integrated into a multimodal imaging platform combining Optical Coherence Tomography (OCT), Multi-Photon Microscopy (MPM), and LSRM, improving adenoma subtype classification to 93–99% accuracy [71].

A recent study from Banerjee et al. used confocal Raman microspectroscopy, with attenuated total reflection-Fourier transform infrared spectroscopy and mass spectroscopy, to classify pituitary adenoma subtypes using blood serum samples [72]. Principal component-based linear discriminant analysis models were developed to classify the subtypes with their Raman spectra. The models classified acromegaly with an accuracy of 79.17%, sensitivity of 75%, and specificity of 81.25%; Cushing with an accuracy of 66.67%, sensitivity of 100%, and specificity of 52.63%; and nonfunctional pituitary adenomas with an accuracy of 73.17%, sensitivity of 75%, and specificity of 72.73%.

These findings highlight Raman spectroscopy's potential for diagnosing and classifying pituitary adenomas. However, all studies so far have been conducted *ex vivo* on samples and biopsies. While analysis of biopsies could be valuable in a clinical setting, providing a faster alternative to histopathological analysis, it does not enhance resection accuracy. A significant advancement would be real-time, *in vivo* tumor interrogation before resection to guide surgical decision-making. This requires integrating Raman spectroscopy into an intraoperative tool capable of accessing the parasellar region. To our knowledge, Raman spectroscopy has yet to be applied *in vivo* to pituitary adenomas using a dedicated probe.

2.2.7 Hand-held Raman spectroscopy probes

Performing conventional Raman spectroscopy with a single surgical tool requires the integration of both excitation and collection signals into optical fibers. A fiber-optic Raman spectroscopy probe was manufactured by a collaboration of the *Lumed Lab* and *EmVision LLC* to perform Raman acquisitions intraoperatively [73, 74]. The probe houses a central 300 μm core silica fiber for laser excitation and 200 μm core silica fibers for collection, as illustrated in Figure 2.6. The excitation fiber is connected to a 785 nm NIR laser, while the collection fibers are connected to a spectrometer. A low-pass filter $\lambda < 785$ nm was placed at the output of the excitation fiber to minimize scattering signals from the optical fibers. A doughnut-shaped high-pass filter $\lambda > 785$ nm was placed in front of the collection fibers to filter Rayleigh scattering and collect Stokes scattering. A focusing lens at the probe's tip ensures overlap of the excitation and collection light cones. This results in an interrogated spot area of 500 μm in diameter at the probe's tip during contact measurements.

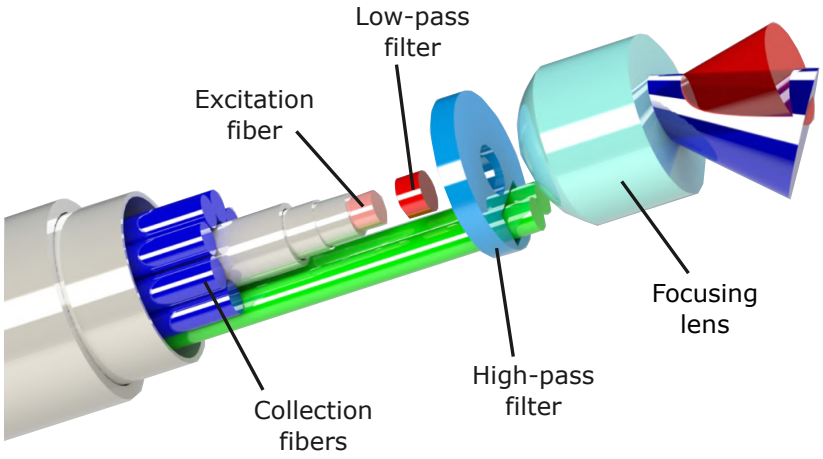

Figure 2.6 Single point hand-held Raman spectroscopy probe. Adapted from [73].

The probe is made of biocompatible and sterilizable materials to ensure surgical compatibility. This type of probe has already demonstrated effectiveness for accurate *in situ* detection of cancer during resection surgery of brain [59], breast [67], and prostate [65] tumors, in studies conducted by the *Lumed Lab*. The developed hand-held instrument achieved diagnostic accuracies of 91% for glioblastoma, 97% for brain metastases, and 96% for meningiomas, distinguishing these from normal brain tissue [59].

Although the excitation wavelength is selected in the therapeutic window to minimize fluorescence, it does not eliminate it, particularly when measuring biological samples, as illustrated with the measurements in Figure 2.5 obtained using this type of probe.

2.2.8 Methods for fluorescence suppression

The dominance of fluorescence over the weaker Raman signal is one of the major challenges in Raman spectroscopy, particularly in biological tissues. Various methods have been investigated to mitigate this effect, broadly categorized into post-acquisition numerical methods, wavelength-domain methods, time-domain methods, and frequency-domain methods [75].

The most common approach is post-acquisition numerical suppression, as it requires no modification to the system or acquisition process. The output signal of a conventional Raman spectroscopy system is an intensity curve versus the wavelength, obtained after diffraction of the collected signal, composed of Raman diffusion and fluorescence. Numerical methods exploit the spectral width difference between the two competing processes. Raman peaks are significantly narrower in bandwidth than fluorescence, enabling various algorithmic baseline correction methods. The simplest and most widely used method is the polynomial regression of the fluorescence signal [75]. A polynomial function of order 4 to 7 can be fitted to approximate the fluorescence signal and is subtracted from the spectrum. However, this technique is sensitive to polynomial order and has seen multiple improved versions, such as the algorithm *I-ModPoly* [76]. Generally, polynomial removal of baseline (i.e. fluorescence) is difficult to tune and often introduces artifacts, especially for biological samples [77]. Derivative-based methods can isolate Raman signals but are associated with increased high-frequency noise [78].

The *Bubblefill* algorithm, developed by *Lumed Lab* and integrated into the ORPL data processing package [77], applies a morphological approach. It uses circular bubbles that iteratively expand to fill the region underneath the spectrum and outperforms most common algorithms across a wide range of samples. This method was used for processing all spectra analyzed in this thesis. Although very practical, numerical methods are limited by the detector's dynamic range, as they do not change the ratio of measured signals (i.e. SBR) and can introduce artifacts.

To suppress fluorescence at the acquisition stage, Shifted excitation Raman difference spectroscopy (SERDS) employs two slightly shifted laser excitations. Signal differentiation lies on the change of the wavelength of the Raman peaks with the excitation wavelength, while the much broader fluorescence peak is insensitive to the excitation wavelength [79]. Time-domain techniques exploit fluorescence's longer emission lifetime (nanoseconds) compared to nearly instantaneous Raman scattering (picoseconds). Time-Gating (TG) methods use ultra-fast pulsed lasers and precise synchronization with the detector to selectively capture Raman signals, significantly improving the SBR. While it provides better results than most techniques, it requires complex and expensive systems [80]. Lastly, frequency-domain meth-

ods exploit the same difference in emission lifetime, which results in greater phase delays and amplitude demodulation in fluorescence compared to Raman scattering when the excitation light is modulated at high frequencies. However, like TG techniques, these methods require sophisticated and expensive instrumentation [75].

2.3 Machine learning and classification of Raman spectra

The molecular diversity of biological samples produces rich and complex Raman spectra, making interpretation more challenging than for single-molecule compounds and minerals. For a long time, this complexity has hindered their routine use for classification in clinical settings [81]. Machine and deep learning methods have been increasingly applied to this field and hold promise for further advancements [81]. However, their "black-box" nature necessitates careful methodological use, as they are prone to errors in result interpretation and method selection.

Machine learning, a subset of artificial intelligence, is widely used for data classification, automated decision-making, anomaly detection, and more. Those automated classification algorithms are trained and tested on the same type of data they are designed to classify. They can be categorized into supervised learning and unsupervised learning methods. Supervised learning involves training on labeled data to make predictions on predefined classes. Unsupervised learning operates without labeled data, typically focusing on tasks such as clustering and anomaly detection.

2.3.1 Application to cancer diagnosis

Diagnostic classification of samples with their Raman spectra can be performed with supervised learning algorithms. The data labels fed to the algorithms can be provided by the gold standard for diagnosis: histopathological analysis. Specifically for cancer diagnosis, data must be classified as *tumor* or *normal* (healthy).

Various supervised learning techniques have been explored to differentiate tumors from normal tissues based on Raman spectra classification. The most common techniques include Linear Discriminant Analysis (LDA), Quadratic Discriminant Analysis (QDA), k-Nearest Neighbor (KNN), Support Vector Machine (SVM), Artificial Neural Network (ANN), and Convolutional Neural Network (CNN). A critical step of supervised learning is determining which part of the Raman spectra data will be used to train the algorithm for class discrimination. This step is known as *feature selection* and can be performed with automated methods such as Principal Component Analysis (PCA) or other algorithms. Deep learning is a branch

of machine learning for which models are based on a neural network architecture, such as ANN, or the more sophisticated CNN. These models do not require prior feature selection, as their deep levels of layers are designed to train on a great number of features and sort the importance of each for their desired task.

Some successful machine learning applications in this field are shown in table 2.1. Although not exhaustive, it illustrates the great potential of the models and the variety of approaches.

Table 2.1 Results of different machine learning classification models for Raman spectroscopy-based cancer detection.

Model	**Pathology/tissue**	**Nb patients**	**Accuracy**	**Sensitivity**	**Specificity**
SVM [82]	Glioma (Brain)	38	87%	87%	87%
PCA-kNN [83]	Colon cancer	67	91.0%	90.0%	92.6%
PCA-LDA [84]	Brain metastases	21	80.2%	Not stated	Not stated
PCA-QDA [85]	Oral cancer	80	82%	84%	75%
ANN [86]	Prostate cancer	32	86%	87%	86%
CNN [87]	Breast cancer	20	92%	98%	86%

Deep learning methods seem to outperform traditional machine learning models in comparative studies [87, 88], and hold the potential to revolutionize this field [89]. However, they are more prone to overfitting, especially on small datasets, and lack interpretability, making it difficult to extract the impact of specific features. Specific features of the spectra often correspond to Raman peaks, which can be linked to biomarkers. This correlation not only aids in refining model testing and improvement but also enhances the understanding of the underlying pathology. The most common model used in biomedical Raman spectroscopy is PCA-LDA [81], and PCA is frequently used for feature selection in supervised learning models. It is a powerful dimensionality reduction tool that can greatly reduce the number of features of a model by creating new uncorrelated features containing most of the initial variance. However, its application to supervised learning can be discussed. Since PCA does not consider class labels during dimensionality reduction, it risks discarding features that are crucial for classification. Furthermore, the transformed features lack interpretability, making it challenging to link them to the original variables or underlying biomolecular information.

Although several algorithms yield excellent results, no consensus exists on which performs best. Moreover, no standardized protocols have been established for applying machine learning in clinical settings, including pre-processing steps, which significantly influence algorithm outcomes. Selecting the best classifier and training parameters for a specific pathology requires extensive testing and optimization. SVM models are well-suited for small datasets with many features, as they are also quite robust to overfitting with regularization techniques and

easy to interpret. For these reasons, it is the only classifier further discussed in this work.

2.3.2 Support Vector Machine

The Support Vector Machine algorithm works by finding a *decision boundary* within the feature space of the data. The *decision boundary* is a hyperplane of dimension N, where N is the number of features and thus the number of dimensions of the feature space. For Raman spectra, the number of features N can be the intensity points associated with specific Raman shifts (i.e. wavelengths). The *decision boundary* tries to separate the classes in the feature space with the help of support vectors. A support vector is a data point of a given class that lies closest to the opposing class and thus to the *decision boundary*. To find the optimal *decision boundary*, the algorithm uses these support vectors and finds the hyperplane that maximizes the total distance between the *decision boundary* and the support vectors, called the margin. Figure 2.7 illustrates this with a linear SVM trained on two features.

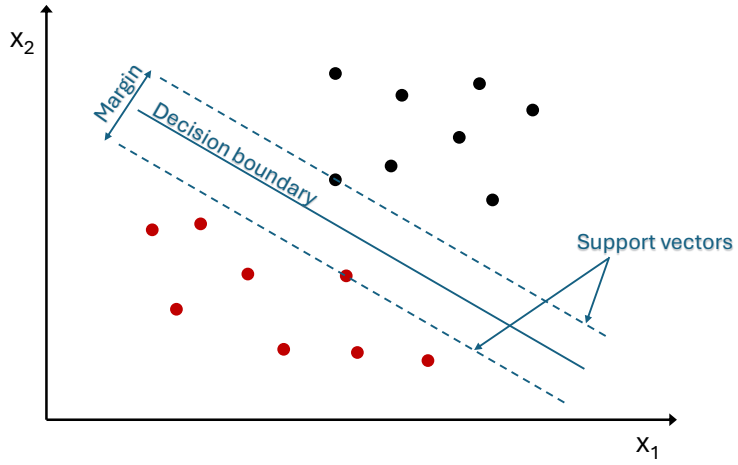

Figure 2.7 Support Vector Machine (SVM) classification of 2 classes in a feature space of 2 dimensions.

While a linear kernel is shown here, SVM can use other kernels to classify data that are not linearly separable. A different kernel function can express data in a new dimensional space in which it becomes linearly separable. Hyperparameters (C,γ) can be chosen to influence the size of the margin and the shape and smoothness of the decision boundary. This affects the model's tolerance for errors and sensitivity to individual data points, influencing the balance between underfitting and overfitting, which are covered in the following section.

2.3.3 Assessing performance

Evaluating a model's performance accurately is a crucial aspect of machine learning, associated with various concepts. High performances commonly reported in biomedical applications often overestimate true performance [81]. This section reviews the basics of performance evaluation. One of the fundamental concepts associated with testing model performance is to do it on data it was not trained on. This involves splitting the dataset into training, validation, and testing subsets.

The performance of the model can be computed for each set of data. Although simple and easy to compute, the accuracy can be a misleading metric to quantify how well a classifier performs. This is the case when the dataset is unbalanced, with one class containing more data than the other. For instance, in a dataset where 90% of the data corresponds to a given class, a model classifying all samples as that class will have an accuracy of 90%. A better performance metric is the Receiver-Operating Characteristic (ROC) curve and the Area Under the Curve (AUC) [90]. ROC curves are graphical plots that illustrate the performance of a binary classification model, by plotting the true positive rate (TPR) versus the false positive rate (FPR), as illustrated in Figure 2.8. The graph illustrates the sensitivity (TPR) and specificity (1-FPR) of the model, addressing the need for accurate classification of both classes. In biomedical applications, both metrics are crucial to avoid false negatives that could miss a diagnosis and false positives that could lead to unnecessary treatments. The AUC synthesizes that information into a single value ranging from 0 to 1, where a result of 0.5 corresponds to a random guess.

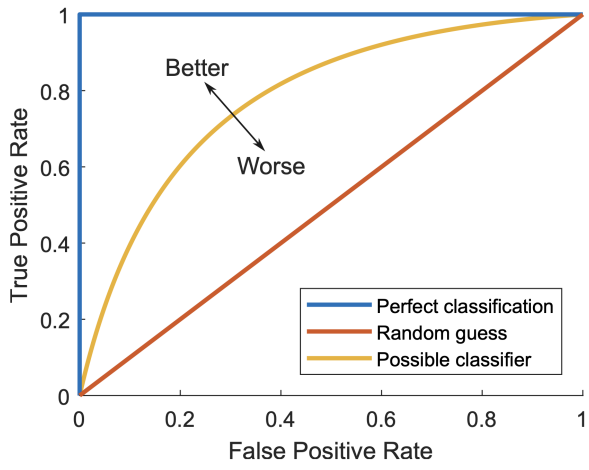

Figure 2.8 Illustration of the Receiver-Operating Characteristic (ROC) curve, the Area Under the Curve (AUC), and their utility to evaluate the performance of a binary classifier.

The training set teaches the algorithm to classify data based on its features. In SVM models, the *decision boundary* is computed to fit the training data. The training process is associated with the concepts of underfitting and overfitting, illustrated in Figure 2.9. If the model performs poorly on the training data, it is said to be underfitting. This indicates that the model fails to properly capture the underlying trend in the data. More complex models or different hyperparameters might perform better. Conversely, high performance on the training set indicates that the model classifies that data accurately. However, it must also generalize and perform well with new and unseen data. If it does not, the model might be overfitting the training data, giving importance to noise and minor details of the training data as illustrated in Figure 2.9.

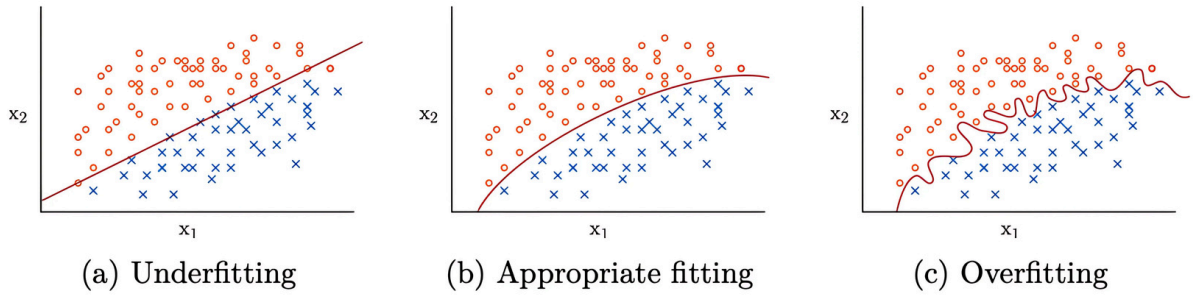

(a) Underfitting (b) Appropriate fitting (c) Overfitting

Figure 2.9 Illustration of a model fitting training data: underfitting, proper fitting, and overfitting.

The validation set helps assess the classifier's performance on unseen data and optimize the model or its hyperparameters. Overfitting and the overall performance of the model might be addressed using the model's results on the validation set. When dealing with small datasets, a popular and practical approach is *cross-validation*, which eliminates the need for a separate validation set. For instance, *K-fold* validation splits the training data into K subsets, using each subset for validation while training on the remaining data. This approach benefits by identifying overfitting in specific folds and providing a more robust evaluation of model performance.

The testing set, however, should not be used for optimization. Its purpose is to provide an unbiased evaluation of the model's performance on unseen data after the training and validation process is complete.

CHAPTER 3 ARTICLE 1: DEVELOPMENT AND PRECLINICAL EVALUATION OF AN ENDONASAL RAMAN SPECTROSCOPY PROBE FOR TRANSSPHENOIDAL PITUITARY ADENOMA SURGERY

Victor Blanquez-Yeste[a,b], Félix Janelle[c], Trang Tran[a,b], Katherine Ember[a,b], Guillaume Sheehy[a,b], Frédérick Dallaire[a,b], Eric Marple[d], Kirk Urmey[d], Moujahed Labidi[c*], Frédéric Leblond[a,b,e*]

[a]Engineering Physics Department, Polytechnique Montréal, Québec, Canada
[b]Centre de recherche du Centre hospitalier de l'Université de Montréal (CRCHUM), Québec, Canada
[c]Division of Neurosurgery, Department of Surgery, University of Montreal, Québec, Canada
[d]EMVision LLC, 1471 F Road, Loxahatchee, Florida, 33470, USA
[e]Institut du cancer de Montréal, Montréal, Québec, Canada
[*]Corresponding Authors, e-mails: frederic.leblond@polymtl.ca, moujahed.labidi@umontreal.ca

Subimtted to *Journal of Biomedical Optics*,
2^{nd} December 2024

Context

This section is not included in the original version of the article.

To address the clinical needs for intraoperative detection of pituitary adenomas and safe navigation, a Raman spectroscopy probe was designed and manufactured to be seamlessly integrated with current transsphenoidal surgery workflows. This endonasal probe was engineered with a form factor compatible with the use of endoscopy systems during transsphenoidal surgeries, facilitating live interrogation of intracranial anatomical structures within the parasellar region. The article reports on the development of the probe and its preclinical evaluation in an animal experiment conducted to differentiate intracranial structures with *in situ* Raman spectroscopy measurements.

The first author's contribution to the article included study design, instrument design, experimental execution, data processing, machine learning model design and evaluation, as well as manuscript redaction. The endonasal design of this probe was realized in collaboration with Dr. Moujahed Labdibi, neurosurgeon for the *Centre Hospitalier de l'Université de Montréal (CHUM)*. A crucial constraint was minimizing the bending stress sustained by the fiber optic cables within the angled instrument. The optical fibers' composition and the optical elements of the tip are similar to that of the probe described in section 2.2.7. Additional illustrations and technical drawings of the probe are represented in Appendix B. The instrument was manufactured by *EmVision LLC*. Benchmark comparisons with earlier probe designs were realized before the presented preclinical evaluation in animals.

The introduction of this article (section 3.2) may overlap with Chapters 1 and 2 of this thesis but can serve as a concise summary.

3.1 Abstract

Significance: For most patients with pituitary adenomas, surgical resection represents a viable therapeutic option, particularly in cases with endocrine symptoms or local mass effects. Diagnostic imaging, including MRI and computed tomography, is employed clinically to plan pituitary adenoma surgery. However, these methods cannot provide surgical guidance information in real-time to improve resection rates and reduce risks of damage to normal tissue during tumor debulking.

Aim: Here we present the development of a hand-held Raman spectroscopy system that can be seamlessly integrated with transsphenoidal surgery workflows to allow live discrimination of all normal intracranial anatomical structures, including the pituitary gland, and potentially, tissue abnormalities such as adenomas.

Approach: A fiber-optic probe was developed with a form factor compatible with endoscopic systems for endonasal surgeries. The instrument was evaluated in an *ex vivo* experimental protocol designed to assess its ability to distinguish normal intracranial structures. A total of 274 *in situ* spectroscopic measurements were acquired from six lamb heads, targeting key anatomical structures encountered in surgery. Support vector machine (SVM) models were developed to classify tissue types based on their spectral signatures.

Results: Binary classification models successfully distinguished the pituitary gland from other tissue structures with a sensitivity and a specificity of 100%. Additionally, a four-class predictive model enabled >95% accuracy *in situ* discrimination of four structures of most importance during pituitary adenoma tumor resection: the pituitary gland, the sella turcica bone, the optic chiasm, and the sella turcica dura mater.

Conclusions: This work sets the stage for the clinical deployment of Raman spectroscopy as an intraoperative real-time decision support system during transsphenoidal surgery, with future work focused on clinical integration and the generalization of the approach to include the detection of tissue abnormalities, such as pituitary adenomas.

Keywords: Raman spectroscopy, pituitary adenoma, neurosurgery, tissue optics, biochemistry, machine learning.

3.2 Introduction

Several tumors originate in the pituitary gland, which regulates hormonal balance and controls endocrine functions. This gland is located in the sellar region at the base of the brain. Pituitary adenomas represent approximately 15% of all intracranial tumors and can have several consequences on human health, including local nerve compression, visual impairment, endocrine dysfunctions and diseases, such as acromegaly, gigantism, or Cushing's disease [4]. The symptoms are contingent upon the size of the tumor and whether it secretes hormones [4, 6]. Endoscopic transsphenoidal resection surgery is a common treatment approach, during which pituitary adenomas and other tumors of the sellar region are removed through the nasal cavity and the sphenoid sinuses, using a rigid endoscope [12]. The endoscope is used for visualization while the patient is under general anesthesia. During the procedure, the anterior wall of the sphenoid sinus is identified and removed. Subsequently, the surgeon removes any remaining septations within the sinus and exposes the sella turcica, the bony cavity that houses the pituitary gland. The bony wall of the sella (sellar floor) is meticulously removed with drills or punches [10]. Subsequently, the dura mater is incised to expose the pituitary gland and the tumor. The tumor is then removed in pieces using micro-instruments or suction devices. Great care is taken to preserve the normal pituitary tissue and to avoid damage to surrounding structures, including the optic nerves superiorly and the carotid arteries laterally. This approach has become the standard for most pituitary adenomas and lesions confined to the sella turcica, because of its precision, safety, and minimal invasiveness [9].

The accurate identification and delineation of tumors during transsphenoidal surgery are of paramount importance, as the objective is to achieve a gross total resection of the tumor while minimizing damage to the surrounding normal structures. Achieving gross total resection safely is critical for local tumor control, as residual tumor volume significantly influences the likelihood of recurrence and endocrine control [13]. Conversely, the resection of normal tissues may result in unintended consequences such as hormonal imbalances and diabetes insipidus [15]. Invasion of surrounding parasellar tissues, such as the cavernous sinus and the dura mater, may also occur, further complicating complete resection [18]. Microadenomas (<10 mm) are often more difficult to localize due to their sizes, while macroadenomas (>10 mm) are associated with greater risks of incomplete tumor resection [7, 8]. In approximately one-third of patients undergoing transsphenoidal surgery for non-functioning macroadenomas, an incomplete resection is inevitable [15]. The development of surgical tools that distinguish tumor tissue from surrounding healthy pituitary tissue in real-time, before surgical resection, could potentially mitigate this outcome.

Currently, preoperative magnetic resonance imaging (MRI) is the preferred imaging technique for tumor visualization and delimitation prior to surgical intervention. Additionally, it enables neuronavigation during the procedure [22]. However, MRI is occasionally unsuccessful in definitively identifying the site of microadenomas and de novo, persistent, or recurrent disease [8]. Various intraoperative detection and imaging techniques are currently used, including intraoperative MRI, computed tomography, and ultrasound probes, which have demonstrated utility in detecting unexpected residual tumors and increasing the likelihood of achieving a gross total resection [30, 33, 37]. Other promising intraoperative techniques include fluorescence-guided endoscopy and contact endoscopy, which enhances tissue vascularity imaging to aid in identifying adenomas [40, 43]. However, these techniques are not yet available in all neurosurgical centers, and while some require a significant amount of time, others are expensive or difficult to implement [19, 27]. As a result, neurosurgeons often rely on visual assessment, supported by preoperative MRI, to determine the nature of uncertain pituitary tissue during surgery.

A promising method for surgical guidance during transsphenoidal surgeries is near-infrared (NIR) Raman spectroscopy. This technique employs inelastically scattered light in biological tissues to reveal molecular information in the form of a spectrum. The vibrational modes of all molecules present within the illuminated biological sample contribute to the obtained spectroscopic information, particularly in the fingerprint region (wavenumber shifts: $\sim$400 to 1800 cm^{-1}). This allows for tissue classification based on molecular composition and could identify normal tissue structures in real-time as well as provide insight into tumoral molecular changes. Raman spectroscopy has been successfully employed for the identification of pituitary adenomas. In 2012, a group of researchers employed Raman spectroscopy to examine several brain tumor specimens obtained during surgical procedures, including pituitary adenomas [69]. More recently, Austrian researchers utilized line scanning Raman microspectroscopy to differentiate between subtypes of pituitary adenoma biopsies, achieving high levels of accuracy [70, 71]. For Raman spectroscopy to become an intraoperative tool, it must be integrated into a fiber-optic probe and encapsulated in a specific endonasal design. A Raman probe could offer minimally invasive and real-time *in situ* tissue classification before resection, providing a faster alternative to post-resection histopathologic analysis.

This work presents the development of a hand-held Raman spectroscopy probe designed for use during endonasal surgeries. The design and development of the instrument are presented as well as a preliminary evaluation of its performance in a preclinical setting. An *ex vivo* experimental protocol was developed to assess the capacity of the method to capture and differentiate *in situ* Raman spectral fingerprints of intracranial tissues within deceased lamb heads. Machine learning models were developed to assess the technique's capacity to classify

and differentiate the various types of tissues encountered during endonasal surgical procedures. This study is an initial step toward the development of a technique that will facilitate real-time identification of abnormalities and normal tissue structures during transsphenoidal surgery.

3.3 Materials and Methods

3.3.1 Hand-held Fiber-optic Probe Adapted to Transsphenoidal Surgery

To address the need for precise and real-time tissue identification described previously, a Raman spectroscopy probe was developed with a form factor allowing access to the pituitary gland during transsphenoidal endonasal endoscopic surgery (Fig. 1a). The probe was designed with a bayoneted handle to improve access to narrow anatomical corridors and to avoid interference between the surgeon's hands and the endoscope [12]. The instrument includes a stainless-steel extension of length 11 cm with a bifurcated tip at its distal end. An angled tip is a standard feature of most endoscope-assisted and microscopic surgery accessories (e.g. curettes, dissectors, hooks, and enucleators). It increases the reach of the surgical tools with a simple rotation and provides improved visualization through the endoscopic system. The length of stainless-steel tubing was determined to ensure surgeons were able to reach the posterior part of the sella turcica comfortably during a procedure.

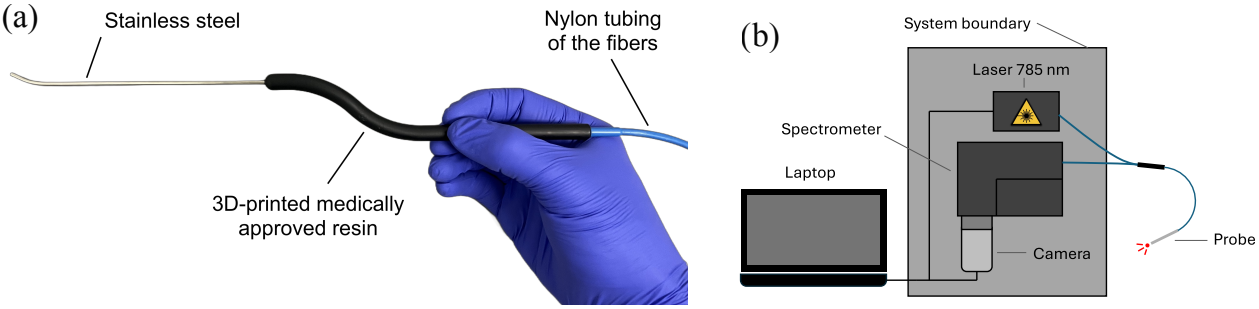

Figure 3.1 (a) Hand-held endonasal Raman spectroscopy probe. Annotations indicate the different types of sterilizable materials used to fabricate the device. (b) Schematics of the complete system illustrating the enclosed module housing the near-infrared laser, the spectrometer, and the sensor, all connected to the endonasal probe. A control laptop manages all system operations.

The stainless-steel tubing, with an outer diameter of 2.1 millimeters, houses thirteen multimode optical fibers. One central fiber, with a 300 μm core diameter, is dedicated to laser tissue illumination, while the remaining twelve collection fibers, each with a 200 μm core diameter, collect reemitted light through a microlens sub-assembly. The slim diameter of the

tubing allows for safe and practical insertion through the sphenoid sinuses. Similar to previously published designs, interference filters were mounted within the probe tip to minimize inelastic scattering and fluorescence signal from the optical fibers material as well as to cut excitation light bleed-through to the spectrometer [74]. The filters and lenses' optical design ensured that measurements, with the probe in direct contact with the sample, resulted in an interrogated spot size of a diameter of 500 μm. All materials used to fabricate the probe were sterilizable and biocompatible, including the wand, crafted from a 3D-printed medically approved resin.

3.3.2 Raman Spectroscopy System: Illumination and Detection Subassembly

A 3-meter fiber optics cable was used to connect the excitation fiber to a NIR laser and the collection fibers to a spectrometer (Fig. 1b). The module housing the illumination and detection components was operated by a custom software responsible for all aspects of system control and data acquisition. Data processing was done using the open-source software ORPL [77]. The complete system consisted of the hand-held endonasal probe (EmVision LLC), the illumination/detection module (Sentry 1000-R, Reveal Surgical Inc.), and custom software packages. The excitation fiber was connected to a continuous-wave 785 nm diode laser (class IIIB) with a maximum output power of 350 mW (Innovative Photonic Solutions, Plainsboro, New Jersey). The detection components consisted of a 100 μm spectrometer slit, a diffraction transmission holographic grating, and a charge-coupled device (CCD) sensor (Newton model, Andor Technology, Belfast, UK), that was pre-cooled at -70°C. Each spectrum acquired with the system covered a range of spectral shifts from 400 to 2000 cm^{-1}, with a spectral resolution of approximately 8.7 cm^{-1}.

The axial resolution of the system, here perhaps more accurately referred to as tissue depth sampling, varies depending on the intrinsic optical properties of the interrogated tissue. Monte Carlo light transport simulations showed that depth sampling varied from 10 to 600 μm, for absorption coefficients (μ_a) of 0.001 to 1.4 mm^{-1} and reduced scattering coefficients ($\mu_s^{'}$) of 0.5 to 30 mm^{-1} [91]. These values cover the ranges expected for biological tissues, including intracranial structures such as the brain, bone, mucosa, and meninges [92–94].

3.3.3 Single-point Spectroscopic Data Acquisition Protocol

A calibration procedure was implemented on each Raman spectroscopy measurement acquired as part of the study [77]. System calibration used a NIST Raman standard (SRM 2214) measurement performed prior to each tissue measurement session to account for the instrument response. A measurement on acetaminophen powder, used as a reference spectrum,

was also performed to calibrate the x-axis, ensuring each camera pixel index corresponded to a spectral bin reported in inverse centimeters (cm^{-1}). The probe tip was cleaned with alcohol after each measurement to minimize the likelihood of contamination from tissue deposits from previous measurements.

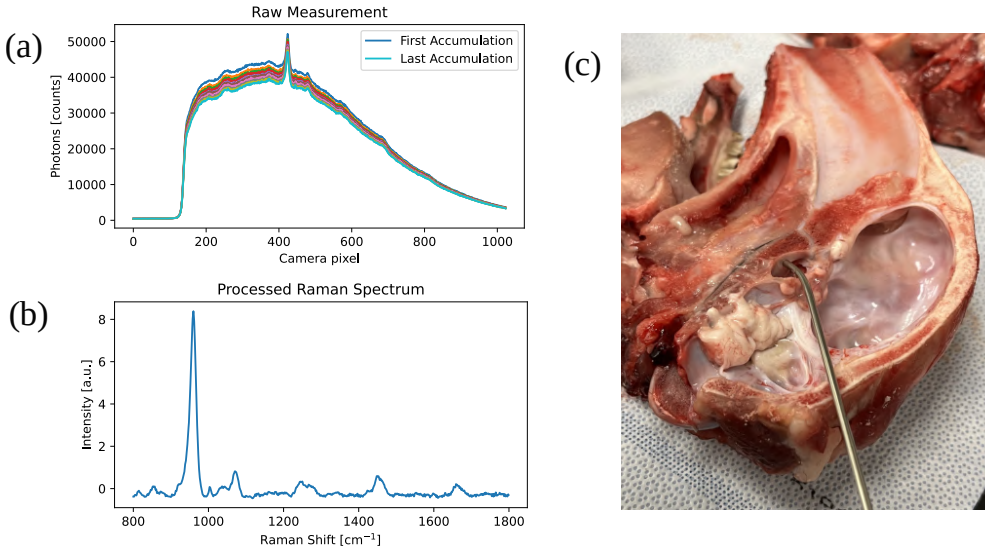

Figure 3.2 (a) Raw spectroscopic measurement using the near-infrared Raman spectroscopy probe. Repeat measurements were made for each tissue location and averaged to maximize the overall signal-to-noise ratio. A representative measurement is shown for the sella turcica bone. (b) SNV-normalized processed Raman spectrum. (c) Close-up of the endonasal probe positioned at an angle on the sella turcica bone, after removal of the pituitary gland and overlying dura mater.

Two individuals were involved with the acquisition of Raman measurements. An engineer (VBY) operated the system while a neurosurgery resident (FJ) identified targeted tissue locations based on knowledge of intracranial anatomy. The neurosurgery resident held the probe in contact with the tissue during each measurement (Fig. 2c). The latter was performed at fixed on-tissue laser power (40 mW) with a variable exposure time, automatically adapted to maximize the photonic count while avoiding CCD sensor saturation [95]. Each spectral measurement consisted of averaging 10 spectral accumulations, with total acquisition times ranging from 3 to 11 seconds, depending on the tissue type. Brain tissues, such as white and grey matter, required longer acquisition times—8.9 and 10.1 seconds on average, respectively—due to their lower signal intensities. All measurements were carried out under low ambient light to minimize background contributions and allow inelastically scattered photons signal to capture the largest possible fraction of the camera's dynamic range.

3.3.4 *In situ* Raman Spectroscopy of Normal Intracranial Structures

A pre-clinical *ex vivo* study protocol was designed and implemented to assess the ability of the Raman spectroscopy probe to detect macroscopically distinguishable intracranial structures, including the brain. A total of 6 lamb heads were purchased at a butcher shop. The heads were all cut in half with a bandsaw through a sagittal plane, exposing the different tissues to be probed within 48 hours of the animals' death. The half-heads were rinsed with distilled water to remove bone residue without affecting tissue integrity.

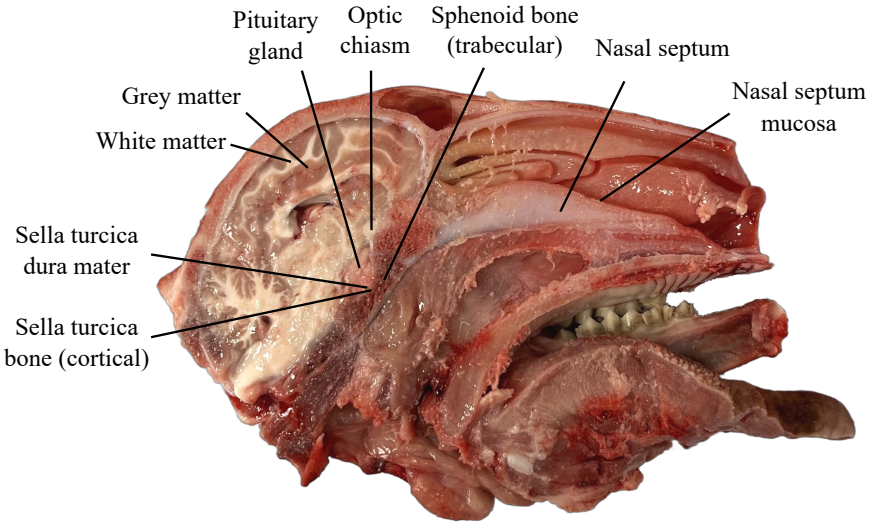

Figure 3.3 Annotated image of a lamb half-head, displaying the various tissues measured using a Raman spectroscopy probe in the scope of the study.

In situ spectral measurements were acquired for 9 different anatomical structures: the pituitary gland, the optic chiasm, the sella turcica bone, the dura mater of the sella turcica, the sphenoid bone, the nasal septum, the mucosa covering the nasal septum, as well as white and grey matter in the brain (Fig. 3). Anatomical regions encountered during transsphenoidal pituitary adenoma resection are the pituitary gland, the optic chiasm, the sella turcica bone and dura mater, and the sphenoid bone. The nasal mucosa and nasal septum are also commonly encountered during the approach to the region where tumor debulking is done. While not relevant to pituitary adenoma resection, white and grey matter were considered here nevertheless for reference, as multiple publications reported Raman spectra of the brain [61,96], including past work from our group [59,97]. In total, between 15 and 59 spectra were acquired for each of the 9 tissue categories across 6 different lambs heads. Visual classification of the tissues and selection of the measurement sites was performed by the neurosurgery resident.

Measurements were conducted on areas accessible with the probe's tip within each tissue type. Specifically for bone tissues, samples were collected from the cortical region of the sella turcica bone, while probing the sphenoid bone focused on its trabecular area, exposed by the cut through the sagittal plane. The trabecular, or spongy region, is the bone's porous lattice structure fully enclosed by opaque cortical bone.

Some tissues were measured after the removal of other structures that initially obstructed the probe's access. For instance, to obtain spectra from the sella turcica bone, the pituitary gland and the dura mater covering the bone were carefully resected (Fig. 2c). For the dura mater, the *in situ* measurements focused on the part of the membrane overlying the sella turcica bone, known as the sella turcica dura, before its resection. The bone was directly beneath the dura, aligned with the probe's field of view. In humans, the dura in this region typically measures approximately 0.4 mm in thickness [98, 99], and is expected to be even thinner in juvenile sheep. The comparison of this value with the probe's estimated sampling depth highlights a potential contribution of Raman scattering originating from the underlying sella turcica bone in the spectral acquisitions corresponding to the sella turcica dura.

3.3.5 Pituitary Gland Measurements Under Different Experimental Conditions

Three different tissue preparation methods were tested to acquire Raman spectra of the pituitary gland, aiming to evaluate spectral consistency and classification model robustness under different experimental conditions. First, *in situ* measurements were made prior to excision, as described in section 2.4, directly on the glands. Then, *ex situ* measurements were made on the excised glands. Finally, the glands were sectioned into 4 or 5 slices of approximately equal thickness ($\sim$2 mm) along the axial plane, resembling the specimens acquired during surgery. These measurements will be herein referred to as "in-section" acquisitions. Three out of 6 lamb heads were selected for this experiment. The resulting dataset included 29 *in situ* measurements, 21 *ex situ* measurements, and 27 in-section measurements. All acquisitions were completed within an hour to minimize the impact of tissue degradation.

3.3.6 Spectroscopic Data Processing and Analysis

Spectroscopic data pre-processing

The following data processing steps were applied to each raw spectroscopic measurement (Fig. 2a) using the ORPL open-source software [77]: 1) subtraction of a dark count background measurement acquired with the laser turned off prior to each measurement (e.g., to remove signal from residual ambient light sources), 2) removal of cosmic ray events, 3) x-axis

calibration using the known positions of Raman peaks and instrument response correction from spectral measurements acquired in calibration materials (acetaminophen, NIST 785 nm Raman), 4) averaging of successive measurements (i.e. accumulations) acquired at the same location, 5) baseline subtraction using a custom algorithm, BubbleFill, with the minimum 'bubble' parameter of 50 cm^{-1}, and 6) curve smoothing using a Savitzky-Golay filter of order 3 with a window size of 1. Spectra were then truncated to keep only the spectral bins between 800 and 1800 cm^{-1}, followed by standard-normal-variate (SNV) normalization (Fig. 2b). As a result of the SNV normalization, the "intensity" associated with each spectral bin must be interpreted as a deviation relative to the average of all detected inelastic scattering contributions across the spectral domain.

Spectral quality factor to assess measurement reliability

A spectral quality factor (QF) metric was computed for each SNV-normalized spectral fingerprint to assess the quality of the Raman signals. This metric measured the average signed squared intensity, quantifying the likelihood that the signal is associated with a random probability distribution [77]. If a signal contains few large and narrow peaks, the QF will be large (close to 1), whereas if a signal contains many small and broad peaks, the QF will be smaller. Finally, a signal that contains only stochastic noise will have a QF of 0. The quality factor is defined as:

$$QF := \frac{1}{N}\sum_{i=1}^{N} \mathrm{sgn}(r_i) \cdot r_i^2 \tag{3.1}$$

where r is an SNV-normalized Raman spectrum and sgn(x) returns the sign (+1 or -1) of the variable x. To ensure high-quality Raman signals for subsequent analyses and machine learning models, a cut-off value of QF was established. The optimal threshold value of 0.3 was chosen to maximize models' performances, while avoiding class imbalances, and was consistent with previous work [59]. This led to the elimination of 10 out of the 284 spectra collected in this study.

Spectral angle mapper to assess the similarity of different measurements

The spectral angle mapper (SAM) was used as a quantitative measure of the similarity between two spectra. The SAM is a metric that measures the angles between spectra in a multi-dimensional space, where each spectral bin is a dimension [100]. It is defined as:

$$\theta = \cos^{-1}\left(\frac{\sum_{i=1}^{n} X_i Y_i}{\sqrt{\sum_{i=1}^{n} X_i^2 \cdot \sum_{i=1}^{n} Y_i^2}}\right) \tag{3.2}$$

where X_i and Y_i are the i^{th} bin (wavenumber shift values) associated with spectra X and Y represented as n-dimensional vectors. This measure of similarity is independent of gain factors due to its angular nature. Identical vectors will have a SAM value of $\theta = 0°$, while $\theta = 90°$ corresponds to orthogonal vectors (i.e. unrelated in spectral shape).

Band assignment for all interrogated tissue types

The relatively narrow Raman peaks (< 50 cm^{-1}), obtained after baseline signal removal, can be associated with their corresponding vibrational modes and biomolecular assignments. However, in biological samples, identifying the specific biomolecular compound giving rise to a Raman peak is complicated by the great number of molecular bonds and their complex structures present in biological tissues. Recent Raman spectroscopy studies have significantly contributed to facilitating identification by compiling published Raman spectral interpretations of biological tissues to develop databases [50]. The peak assignments of the spectral fingerprint acquired in this study were based on multiple studies focused on Raman spectroscopy of pure molecules, such as proteins, lipids, and amino acids [51–53]. All the assignments were then correlated with databases, and cross-checked with their original publications and corresponding samples.

3.3.7 Machine Learning Tissue Classification Models

Predictive modeling approaches were used to assess the ability of Raman spectroscopy to distinguish different types of intracranial tissues. Two machine learning classification modeling schemes were used to train, validate, and test models with the *in situ* Raman spectra. Binary models were initially developed to assess the ability of the technique to distinguish the pituitary gland from all other normal structures. Then, a more clinically relevant model was developed in the form of a 4-class model designed to discriminate four structures of importance for surgical guidance during pituitary adenoma tumor resection.

The first class of models (Models I) consisted of multiple two-class classifiers, each specifically designed to differentiate the pituitary gland spectra from those of a single other probed tissue. Additionally, one model was trained to distinguish the gland from all the other tissues combined. This approach focused on distinguishing normal (healthy) gland tissue from molecularly distinct tissues, particularly surrounding tissues, such as the dura mater and bone of the sella. This served as a foundational step toward differentiating between normal gland tissues and adenomas in human patients. No classifier was built to distinguish the gland from the nasal mucosa and septum measurements, as the number of spectra collected for these tissues (n = 15 each) was deemed insufficient to provide a robust testing set.

Additionally, these distinctions were considered less clinically relevant. The second class of models (Model II) was a multi-class model developed to differentiate four neighboring tissues commonly encountered during surgery: the pituitary gland, the sella turcica bone, the optic chiasm, and the sella turcica dura mater. This model highlighted the potential of the probe for surgical guidance by providing real-time tissue mapping to improve procedural safety during adenoma resection.

All models were tested on hold-out datasets that were not used during training and validation. For all tissues, between 33% and 40% of the measurements were reserved for testing, while the remaining 60% to 67% were used for training and validation. To ensure the ability to classify tissues from new and independent individuals could be tested, the training and testing datasets were completely separated by heads, ensuring that no data from the same individual was used in both training/validation and testing.

The methodology used to develop the models was described elsewhere [59]. Briefly, each processed Raman spectrum consisted of approximately 1,000 spectral bins, ranging from 800 to 1800 cm^{-1}. Prior selection of Raman peaks was applied to prevent the inclusion of features that corresponded to stochastic noise rather than actual Raman signal [101]. Then, the number of spectral bins used for machine learning modeling was reduced to N < 20 spectral features through a linear support vector machine (SVM) approach with L1-regularization (Lasso regression) optimization, which promotes sparsity by selecting only the most relevant spectral features. The optimal N was determined via cross-validation to balance model performance and prevent overfitting. The selected features corresponded to the spectral bins with the largest absolute coefficients from the linear SVM. These features were used to train and validate the final classification SVM model with L2-regularization (Ridge regression). Hyperparameter optimization was applied to the regularization methods of both the feature selection and classification phases to maximize predictive accuracy using five-fold cross-validation. Monitoring accuracy across the folds minimized the risk of overfitting. The cross-validation results were summarized in confusion matrices by aggregating the results from each fold.

Once the optimal parameters were selected for all models, performance was assessed using the hold-out testing datasets, with accuracy metrics, confusion matrices, as well as receiver-operating-characteristic (ROC) analysis for the two-class models I. The multi-class model II results on the validation and testing data were summarized in a four-by-four confusion matrix. Subsequently, *ex situ* and in-section pituitary gland measurements were classified using Model II, which had been trained solely on *in situ* measurements, to assess the ability to classify spectra independent of the acquisition method. These results were also presented

in four-by-four confusion matrices.

3.4 Results

3.4.1 *In situ* Tissues Mean Spectral Fingerprint and Band Assignment

All the SNV-normalized spectra collected *in situ* for each type of tissue were represented in the form of spectrograms (Fig. 4a). In those spectrograms, each line corresponded to an individual spectrum depicted as a yellow (maximum value) to blue (minimum value) gradient. The name and total number of processed spectra for each tissue were shown on the spectrogram for each tissue category. The average Raman spectrum for each tissue type was also drawn along with the variance across all measurements (Fig. 4b). The variance was computed for each spectral bin and was represented as a semi-transparent grey band.

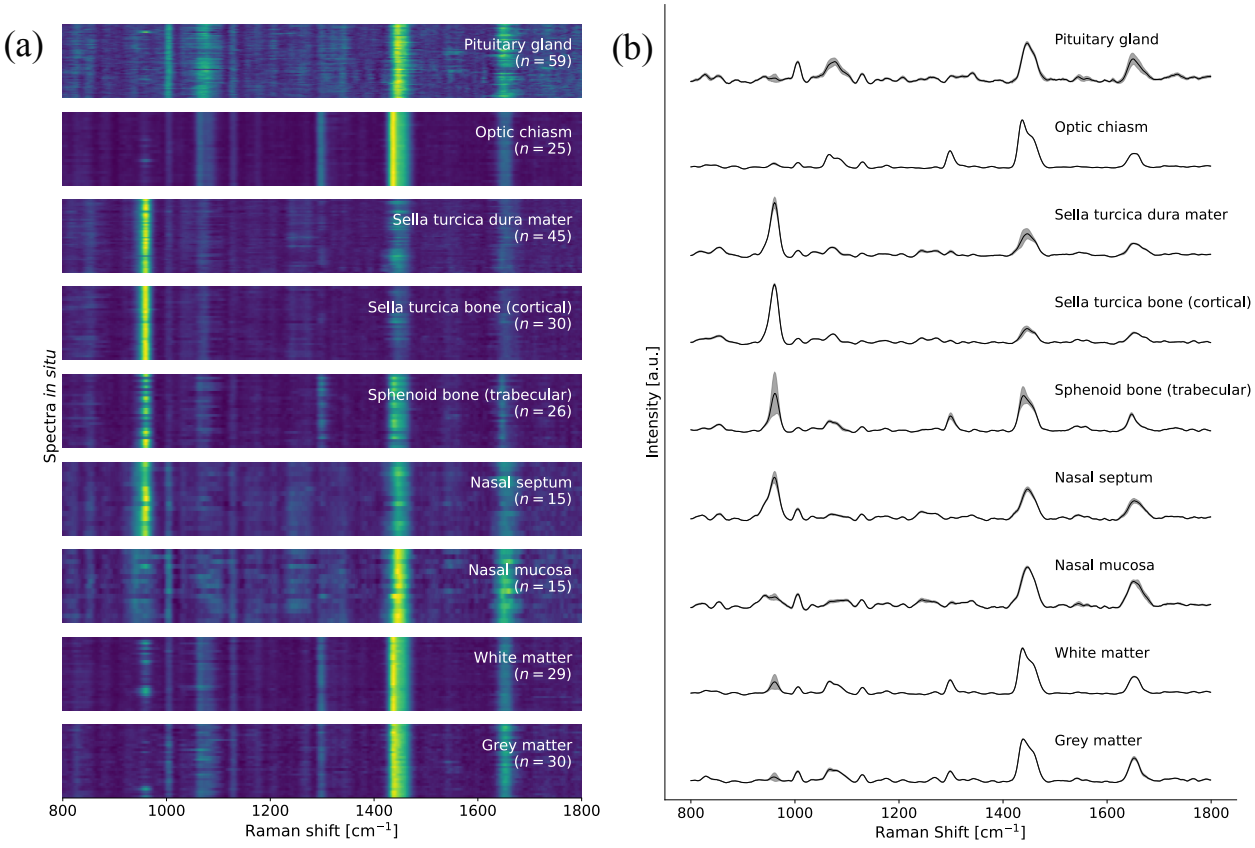

Figure 3.4 (a) Spectrogram showing the entire *in situ* Raman spectroscopy dataset. (b) Average spectra per tissue, with the corresponding inter-measurement variance shown for each spectral bin.

The assignments of the spectral bands composing the mean spectral fingerprints of the tissues

are summarized in Table 1. For each visually identifiable spectral peak, a biomolecular association with the corresponding vibrational modes was attempted. The relative intensity (across all tissues) of the spectral peaks was categorized using a scale from 1 to 5 and represented with asterisks ranging from the lowest contribution (*) to the highest (*****).

Table 3.1 Principle vibrational modes, band assignments, and corresponding relative concentration in each tissue type indicated by the number of asterisks from lowest (*) to highest (*****).

Peak center (cm^{-1})	Main vibrational modes	Biomolecular assignment	**Pituitary gland**	**Optic chiasm**	**Sella turcica bone and dura mater**	**Sphenoid bone**	**Nasal septum and mucosa**	**Cerebral matter**
822-825	C-C stretching	Proteins (Tyrosine)	*	-	-	-	*	-
856	C-C vibration	Proteins (Tyrosine)	*	-	*	*	*	-
940	ν(C–C) skeletal	Proteins (N-C-C)	*	-	-	-	**	-
961	Calcium phosphate stretch band	Calcium hydroxyapatite, cholesterol, protein (tryptophan, valine)	*	*	Bone: ***** Dura: ****	****	Bone: **** Mucosa: **	*
1004	Symmetric stretching and ring breathing modes	Protein (phenylalanine, tryptophan)[34,36]	**	*	*	-	**	*
1064	Skeletal C–C stretch	Lipids, triacylglycerols (C-C)	**	**	-	*	-	*
1078	C–C and C–O stretching mode	Phosphate (dihydrogen phosphate, hydrogen phosphate), lipid (C-C)[35]	**	*	*	*	-	*
1128	C–N stretching	Fatty acid (C-C), protein (C-N, serine),[34,36] glucose	*	*	-	*	*	**
1298	CH_2 twisting, deformation	Lipid (CH_2)	*	**	-	**	-	White: ** Grey: *
1437-1439	CH_2 deformation, scissoring, bending	Lipid (CH_2, CH_3),[35] protein (C-H, isoleucine, valine)[34,36]	***	****	Bone: * Dura: **	***	Bone: ** Mucosa: ***	****
1446-1452	CH_2/CH_3 deformation	Protein (histidine, leucine, lysine, methionine, serine, threonine)[34,36]	****	***	Bone: * Dura: **	***	Bone: *** Mucosa: ****	***
1649-1652	C=O and C=C stretching, α-helix	Lipid (unsaturated C=C),[35] protein (amide I)[34,36]	***	**	*	**	Bone: ** Mucosa: ***	White: ** Grey: ***

The peak at 961 cm^{-1}, often referred to as the mineral peak [50], is associated with calcium hydroxyapatite, a mineral component that makes up ∼60% of bones [102]. It is highly present in bone spectra, such as the sella turcica, sphenoid, and nasal septum bone. The peak at 1004 cm^{-1} can be attributed to proteins, such as phenylalanine and tryptophan [51, 53].

Both 1064 and 1298 cm^{-1} peaks are primarily due to lipids, with a higher contribution in the pituitary gland, optic chiasm, and cerebral matters. Lipids can be found in the form of phospholipids, cholesterol, and triglycerides in the pituitary gland [103]. The optic chiasm and cerebral matter are high in lipids, which compose 70% to 80% of myeline [104, 105], the insulating layer surrounding nerve fibers. Those peaks are also present in sphenoid bone, likely because measurements were taken from the spongy, trabecular region of the bone,

containing bone marrow. Marrow is composed of hematopoietic cells (bone stem cells) and marrow adipose tissue is high in lipid and supportive stromal cells [106]. It is also associated with a lower mineral density than cortical bones [106], correlating with the lower intensity of the mineral peak (at 961 cm^{-1}) in the spectral fingerprint of the trabecular sphenoid bone. Those spectra also show significantly more variance than those of the cortical region of the sella turcica bone. This variability reflects the trabecular bone's porous lattice structure, which contains more connective tissues, marrow, fat, and blood vessels, contributing to its greater heterogeneity compared to the denser, more uniform cortical bone [107]. Only 20% of the volume of the trabecular compartment is bone [107].

The peak with the highest contribution in the components of the central nervous system (CNS), such as both cerebral matters and the optic chiasm, is at 1437 to 1439 cm^{-1}. It has been associated with proteins, lipids, and DNA/RNA. The aggregation of these different molecular species represents the distribution of proteins and genetic information in nerve fibers of the CNS. Similarly to lipids, different proteins can be found in myelin, such as myelin basic protein, proteolipid protein, isoleucine, and valine [105]. This peak also contributes significantly to the spectra of the pituitary gland and the nasal mucosa. However, the highest contribution for both tissues is the peak at 1446 to 1452 cm^{-1}, which encompasses fatty acids and other lipids. These lipids are important components of the pituitary gland's lipid composition [103]. The peak at 1649 to 1652 cm^{-1}, associated with a mix of lipid and protein contribution, such as amide I, is present in most tissues. Its lowest relative contribution appears in the cortical bone's spectrum, similar to the other peaks associated with proteins and lipids.

The similarity between the average spectral fingerprints of the tissues was assessed by computing the SAM of all possible pairs of average spectral fingerprints (Fig. 5), which was represented by an average SAM value of 41.04°. The average spectra of the optic chiasm and white matter yielded the lowest SAM value of 9.16°, probably due to their similar composition of myelinated axons, which gives them their white appearance. The angles computed for these tissues when compared to grey matter were 12.08° for white matter and 14.54° for the optic chiasm. While all three tissues share similar compositions as integral components of the central nervous system (CNS), grey matter differs as it is primarily composed of unmyelinated axons, neuronal cell bodies, and dendrites [108].

The visual resemblance between the spectral fingerprints of the dura mater and the bone of the sella turcica is corroborated by a SAM value of 12.77° between their mean spectra. This similarity is notable given the distinct compositions of these tissues: the dura mater is a membrane composed primarily of connective tissue rich in collagen and elastic fibers [98],

Figure 3.5 Spectral Angle Mapper (SAM) computed between the average Raman spectra for all possible combinations of tissue types. SAM values range from 0° for identical spectral fingerprints to a maximum of 90° when the spectra are highly dissimilar.

whereas the underlying tissue consists of dense cortical bone. The presence of a varying and pronounced mineral peak at 961 cm^{-1}, characteristic of bone tissues, is notable, though less intense than in the sella turcica bone's fingerprint. This peak's intensity, along with the varying higher intensities of peaks associated with proteins and lipids in the dura mater's mean spectrum compared to the bone, supports the hypothesis of an underlying bone contribution within the dura mater's Raman signals. All the other SAM measurements between average spectra of different tissues were superior to 20°, indicating less similarity.

While SAM provides a useful dataset overview by comparing average spectra, its effectiveness in classifying individual spectroscopic measurements is limited. Since SAM relies on spectral angle calculations, baseline variations and noise can shift vector orientation without altering key spectral features, resulting in misleading similarity measures. For all tissues, some comparisons of spectra within that same tissue yielded higher SAM values than those with spectra from different tissues, emphasizing this limitation. In contrast, machine learning models provide superior accuracy, robustness to noise, and scalability, making them more suitable for clinical applications. Unlike SAM, which depends on a predefined reference and

is greatly affected by spectral variability, SVM can generalize to new spectra, select key spectral features, and mitigate overfitting through regularization.

3.4.2 Binary Tissue Classification Models

Visual inspection of the average Raman spectra for each tissue type revealed distinct spectral bands enabling discrimination, which was further confirmed by the SVM models. The Raman peaks from which spectral features were selected for machine learning modeling in distinguishing the pituitary gland from the sella turcica bone were highlighted in graphs showing average spectra for these two tissue types (Fig. 6a). Key peaks used to separate the pituitary gland from the bone included the peaks centered at 961, 1004, 1438, and 1650 cm^{-1}, attributed to mineral, phenylalanine (proteins), lipids, and proteins (amide I) contributions respectively. The model was able to predict tissue class with 100% sensitivity and 100% specificity, both during the cross-validation phase (Fig. 6b) and when it was directly applied to an independent testing set (Fig. 6c).

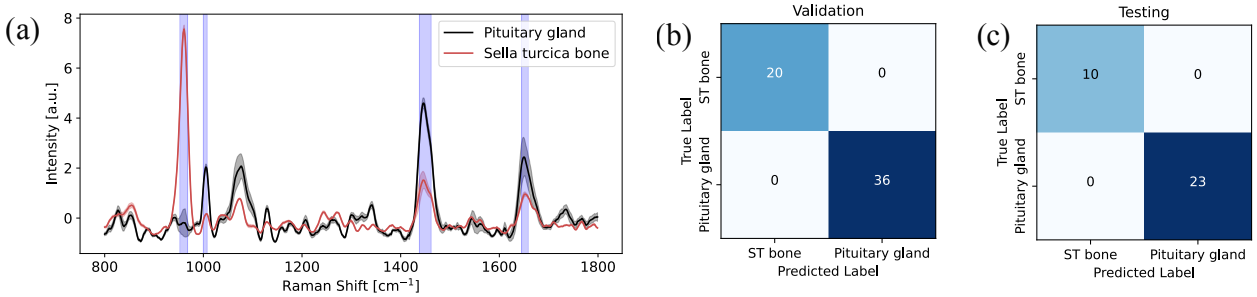

(d)

Class 1	Class 2	Raman peaks center [cm^{-1}]	Validation accuracy	Testing accuracy	Testing AUC
Pituitary gland	Optic chiasm	1004, 1298, 1438	100%	100%	1
Pituitary gland	Sella turcica dura mater	961, 1004, 1438, 1650	100%	100%	1
Pituitary gland	Sella turcica bone	961, 1004, 1438, 1650	100%	100%	1
Pituitary gland	Sphenoid bone	1004, 1298, 1438	100%	100%	1
Pituitary gland	White matter	1004, 1298, 1438	100%	100%	1
Pituitary gland	Grey matter	1004, 1298, 1438	100%	100%	1
Pituitary gland	All other tissues	1004, 1078, 1438, 1650	98.7%	100%	1

Figure 3.6 Results of the 2-class predictive models classifying the pituitary gland and the sella turcica (ST) bone: (a) average Raman spectra with the bands from which features were used for modeling highlighted in blue, confusion matrices representing the classification results associated with the (b) cross-validation and (c) testing phases of model development. (d) Table summarizing the results of all 2-class models, including the Raman bands from which features were used by the models, validation and testing predictive accuracies as well as the area-under-the-curve (AUC) of the testing set receiver-operating characteristic (ROC) analysis curve.

For conciseness, spectral comparison graphs and confusion matrices were not shown for the

models developed to distinguish the pituitary gland from the optic chiasm, the dura mater, the sphenoid bone, white matter, and grey matter. However, the performance metrics, as well as the main peaks from which spectral features were extracted for modeling, were tabulated (Fig. 6d). On average 11 spectral features were used by the models which all led to 100% validation and testing accuracies. All models were associated with a ROC curve area-under-the-curve (AUC) of 1. Discrimination from the sella dura mater required features from the same peaks as the bone, i.e. 961, 1004, 1438, and 1650 cm^{-1}. Discriminating the pituitary gland from the other structures (optic chiasm, sphenoid bone, white matter, grey matter) was possible with identical spectral peaks. The classification was done by selecting features from the bands centered around 1004, 1298, and 1438 cm^{-1}.

Lastly, the model designed to differentiate the pituitary gland from all other probed tissues used 20 spectral bins and misclassified 1 out of 36 pituitary gland spectra and 1 out of 115 spectra from other tissues during cross-validation, achieving a sensitivity of 97.2% and a specificity of 99.1%. In the hold-out test set, all spectra were correctly classified, resulting in a testing accuracy of 100%, which was tabulated along with the other performances (Fig 6d).

3.4.3 Multi-Class Tissue Classification Model

A multi-class predictive model was then developed that could be used as a real-time decision support system for neurosurgical guidance. The model was trained, validated, and tested using the *in situ* spectral datasets associated with the pituitary gland, the optic chiasm, the sella turcica dura, and the sella turcica bone (Fig. 7a). The spectral peaks chosen to perform multi-class discrimination were highlighted in blue on the spectral graphs and correspond to the bands around 961, 1004, 1064, 1298, 1438 and 1650 cm^{-1}. A total of 19 spectral bins (i.e. intensities corresponding to different wavenumbers) were used as features for the model. The model resulted in an accuracy of over 95% in training/validation, with only dura mater and bone spectra being misclassified, with validation accuracies of 90% for both classes. The model achieved an accuracy of 100% when applied to the hold-out testing set. The confusion matrices were shown for the validation phase (Fig. 7b) and the testing phase (Fig. 7c). The model misclassified 4 spectra out of 94 in the training/validation, while correctly classifying all the testing spectra that were not used for training and tuning of the model.

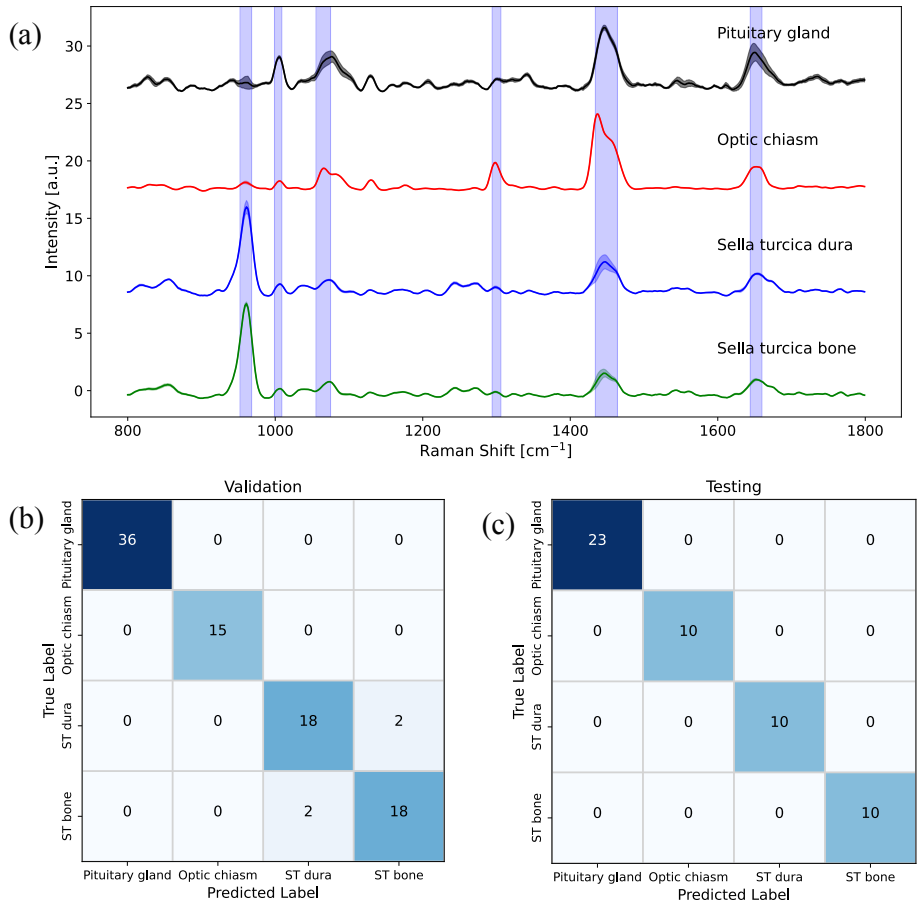

Figure 3.7 Results of the multiclass predictive model (model II). (a) Average Raman spectra of the tissue measurements used to develop a machine learning model. The bands from which features were used for modeling are highlighted in blue. (b) Confusion matrix representing the classification results associated with the cross-validation phase of model development. (c) Confusion matrix showing the results of the machine learning model on the testing hold-out dataset.

3.4.4 Comparison of *In situ*, *Ex situ*, and Sectioned Pituitary Gland Raman Acquisitions

The average Raman spectral fingerprints of the pituitary gland for all three different acquisition methods (*in situ*, *ex situ*, in-section) were represented with the corresponding variance associated with all spectral bins (Fig. 8a). Those fingerprints seemed visually similar while sharing some peak intensity differences, notably at 1064, 1341, and 1650 cm^{-1}. The total variance of the spectra for each measurement method, represented in Figure 8b, was calculated as the sum over all spectral bins. *In situ* measurements exhibited the highest total variance, followed by *ex situ* measurements, while the measurements from sectioned glands

showed the lowest total variance. This trend was consistent across all individual heads, as illustrated in the figure. The assessment of signal similarity between different methods, based on SAM measurements between the average spectra (Fig. 8c), showed that *in situ* and *ex situ* spectra shared greater spectral similarity compared to *in situ* and in-section spectra. Meanwhile, *ex situ* and in-section spectra exhibited the lowest SAM value, indicating the highest similarity. This relative ranking of similarity remains consistent across all individual heads.

Multi-class model II, which was trained using *in situ* measurements, accurately classified all the *ex situ* and in-section spectra as pituitary gland tissue, illustrated in the testing confusion matrix of both methods (Fig. 8). This demonstrates our ability to classify the glandular tissue with perfect accuracy, regardless of the acquisition method.

3.5 Discussion

Raman spectral fingerprints of different intracranial tissues critical to transsphenoidal surgery were measured and subsequently analyzed with biomolecular assignments and similarity comparisons. The alignment of peak intensities with each tissue's biomolecular composition substantiated the accuracy and reliability of the Raman signal acquisition process. The results of both binary and multi-class models demonstrated the ability of the technique to classify structures *in situ* with the Raman probe.

The spectral angle mapper (SAM) metric was used to assess the similarity of average spectral fingerprints of the different tissue. It allowed a better comprehension of the obtained spectra and validation with previous studies. This metric could be further explored to regroup similar tissues prior to machine learning classification. The observed similarity between the spectral fingerprints of the dura mater and the bone of the sella turcica is likely caused by the spectral contribution of the underlying bone in the spectrum taken on the thin dura mater, as suspected prior to the acquisitions. Nevertheless, multiclass model II was able to accurately classify those tissues. In the context of a clinical study, dura mater tissues in adult human patients are expected to be thicker than in lamb, potentially minimizing that effect. However, these findings suggest that the impact of the tissue-dependent sensing depth needs to be monitored.

Classifying pituitary adenomas from normal glands in human patients is expected to be more challenging than the classifications done by models I, as adenomas share a more similar molecular structure with normal glands, probably leading to more closely related spectral fingerprints than normal glands and surrounding structures. However, these results confirm

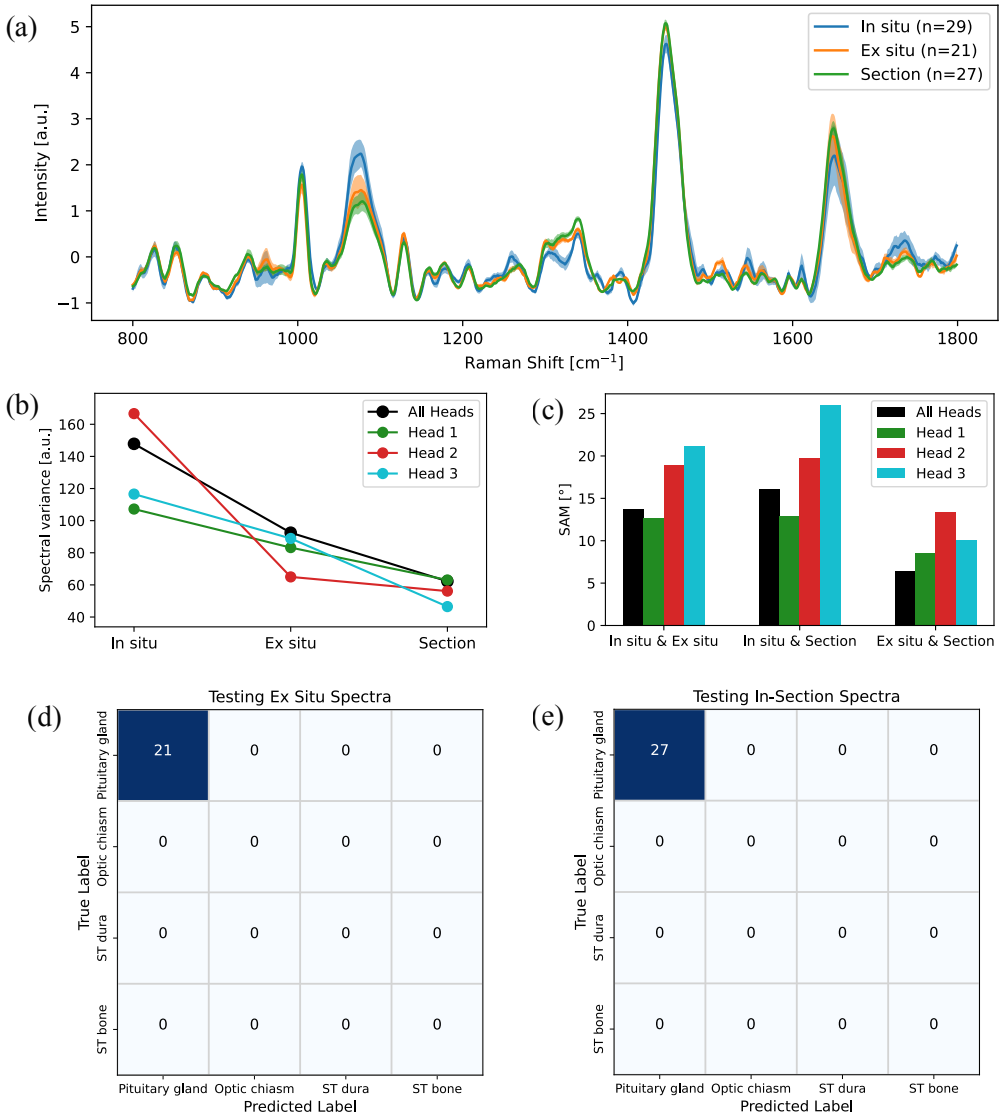

Figure 3.8 (a) Average Raman spectra of pituitary glands associated with each tissue preparation method (*in situ*, *ex situ*, in-section) with their corresponding inter-measurement variance. (b) Variance summed over all spectral bins for each acquisition method, and (c) SAM values computed between the average spectra from all combinations of tissue preparation methods. Variances and SAM values are represented for spectra averaged for each individual lamb head as well as for spectra averaged across all 3 lamb heads. Confusion matrices representing the classification results obtained when applying multi-class Model II to measurements associated with (d) *ex situ* and (e) in-section tissue preparation methods.

our ability to capture a spectral fingerprint specific to the normal gland in deceased lambs, as well as our ability to distinguish it from various other surrounding tissues in new individuals. Previous studies using comparable Raman spectroscopy systems have achieved high classification accuracies (>90%) in distinguishing brain tumors from normal tissue during

human surgical procedures [59]. These promising findings suggest that pituitary adenoma classification should be further explored in a clinical study involving human patients.

For multiclass model II, the slightly lower accuracy during cross-validation is likely due to the reduced dataset size that the model was trained on during five-fold cross-validation, combined with the similarity of the spectral fingerprints of sella turcica dura mater and bone, which were the only misclassified classes. However, the perfect classification of the model on the testing set comprising new individuals, illustrates the high potential of the probe as a multiclass tissue classifier to guide safe transsphenoidal endonasal surgery, as it would allow real-time mapping of any tissue whose exact nature is unsure during the operation.

Regarding the comparison of the different acquisition methods, the differences in spectral variance and the results of the similarity measurements between the methods can be attributed to greater contamination of the pituitary gland signal by surrounding tissues in the *ex situ* method, and even more so in the *in situ* method. Residual tissue from the cutting process used to expose the gland is likely more present on the surface in both *in situ* and *ex situ* spectra, despite rinsing the half-heads, compared to in-section gland spectra exposing the inner gland. In the *in situ* method, additional contamination may occur due to improper probe placement near tissue boundaries, causing the probe to detect scattered photons from adjacent tissues within the illuminated volume. Measurements performed on resected specimens seem to capture the Raman signal of the gland more accurately than those performed *in situ*. The results also highlight that differences between the acquisition methods seem to introduce more variability in the spectra than differences between individuals.

Considering all factors, a precise and accurate definition of the exact structures included in the illumination volume of the probe is crucial for a clinical study, whose first objective would be to acquire various spectral fingerprints characteristic of specific tissues. Accurate labeling of the spectra collected to train classification models is paramount. Measurements taken *in vivo* during surgery and their localization should be accurately correlated to resected specimens to obtain their true label. While the impact of measurements taken with different acquisition methods should be monitored, *ex vivo* measurements on tissues after their resection could prove useful. These measurements could present less cross-contamination of the other structures and various liquids associated with surgeries. They could validate and provide insights on the *in vivo* acquisitions, and increase the size of the dataset, a key factor in machine learning efficiency.

Disclosures

Frédéric Leblond co-founded Reveal Surgical, a medical device company that seeks to commercialize a Raman spectroscopy system for intraoperative cancer detection.

Code, Data, and Materials

The data and materials information that support the findings of this study are available from the corresponding author upon reasonable request.

Acknowledgments

This work is supported by the Discovery Grant program from the Natural Sciences and Engineering Research Council of Canada (NSERC) and the Canadian Institutes of Health Research (CIHR).

CHAPTER 4 INTEGRATION OF A HAND-HELD RAMAN SPECTROSCOPY SYSTEM INTO TRANSSPHENOIDAL SURGERY

This chapter presents the integration of a Raman spectroscopy system into transsphenoidal surgery to perform *in vivo* and *ex vivo* measurements of structures involved in parasellar tumor resection. The first section details the *Lumed Lab* enclosed system for surgical use and contributions made to its recent modernization. Next, laser safety measures for class IIIB lasers in human patients are discussed. The impact of the operating endoscope light on *in vivo* Raman measurements and strategies developed to filter out this interference are then examined. Finally, the chapter outlines the integration of the *Lumed lab* system in the clinical study.

4.1 Raman spectroscopy system

A recent upgrade of the *Lumed Lab* Raman spectroscopy systems, designed for surgical use, was conducted by lab members to optimize performance and enhance safety. As described in section 3.3.2, the system's main components include a probe, a continuous-wave 785 nm diode laser (class IIIB) with a maximum output power of 350 mW (Innovative Photonic Solutions, Plainsboro, New Jersey), and detection components. The detection system comprises a 100 μm spectrometer slit, a diffraction transmission holographic grating, and a charge-coupled device (CCD) sensor (Newton model, Andor Technology, Belfast, UK). The probe's 3-meter fiber-optic cable connects the excitation fiber to the NIR laser and the collection fibers to the spectrometer, as illustrated in Figure 4.1. The system also incorporates a microcontroller and various components to ensure coordinated operation and safe management of all system elements.

The modernization of the systems included:

- Complete isolation of all illumination, detection, and electronic components within a protective casing equipped with ventilation, as shown in Figure 4.1.
- Optimization of system control through the custom software *ORAS*, integrating new methods, components, and logic to improve reliability, safety, and workflow.
- Upgrade of the Graphical User Interface (GUI) for the *ORAS* control software.
- Implementation of robust safety mechanisms, including independent laser emergency controls (shutoff switch and turnkey) isolated from software communications.

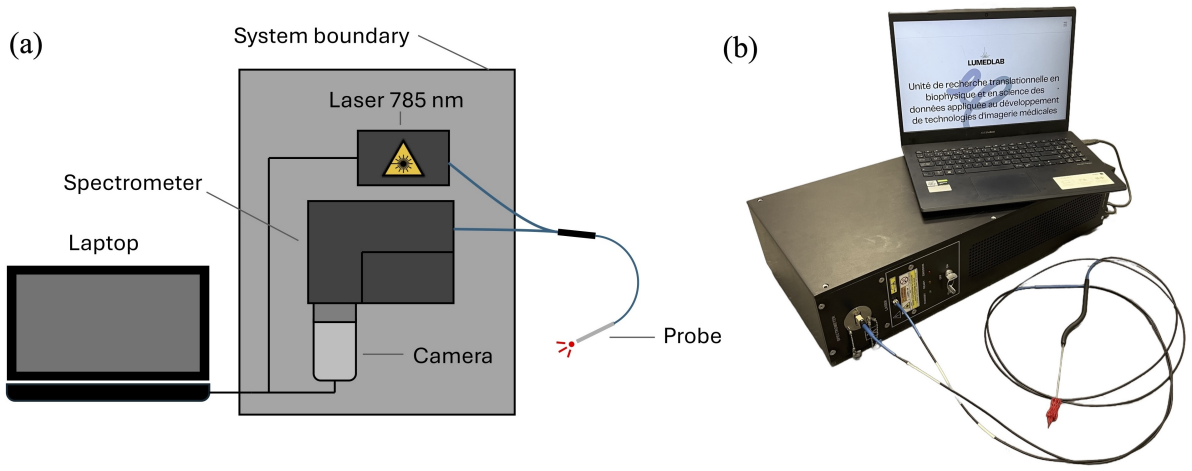

Figure 4.1 Raman spectroscopy system for surgical use. (a) Schematics of the complete system illustrating the enclosed module housing the near-infrared laser, spectrometer, and detector, all connected to the endonasal probe and control laptop. (b) Photograp of the control laptop, enclosed module, and endonasal probe.

The technical specifications of the system, including a hand-held probe, are presented in Table 4.1.

Excitation wavelength	785 nm
Probe output power	0-100 mW
Sampling area	500 μm diameter
Sampling depth	$\sim$100-600 μm
Spectral range	$\sim$400-2000 cm^{-1} ($\sim$810-931 nm)
Spectral resolution	$\sim$8.7 cm^{-1}

Table 4.1 Technical specification of the Raman spectroscopy system.

4.1.1 Original contribution: laser control

In the context of this thesis, a laser control module was implemented in *python* to control the newly integrated IPS (Innovative Photonic Solutions) digital U-Type module lasers via serial commands, as recommended by the manufacturer [109]. Communications with the IPS lasers use command syntax and structure following the rules defined in the Standard Commands for Programmable Instruments (SCPI v1999.0), based on the IEEE 488.2 standard. Serial communications are transmitted and received via a USB connection to the laser module using 8-bit ASCII encoding, as shown in Figure 4.2. The control module implements all commands specified in the user guide [109], along with custom methods implemented for Raman spectroscopy, such as pulse generation.

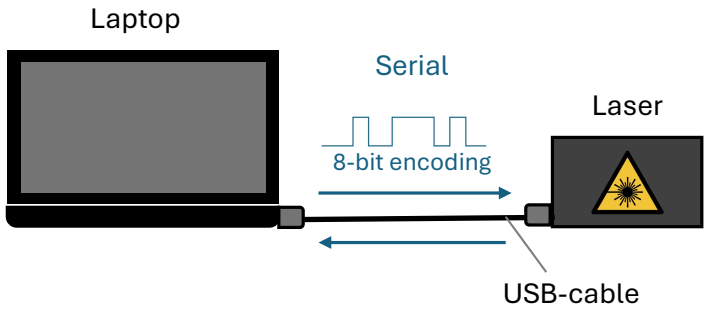

Figure 4.2 Schematics of the serial communication between the control laptop and the laser.

A User Interface (UI) was developed to allow basic control of IPS lasers, integrating the methods of the control module. The UI was later integrated by *Guillaume Sheehy* in the *ORAS* software, as a widget in the *Sources* pane (tab in Figure 4.3). The control module's methods were used in *ORAS* for Raman acquisitions.

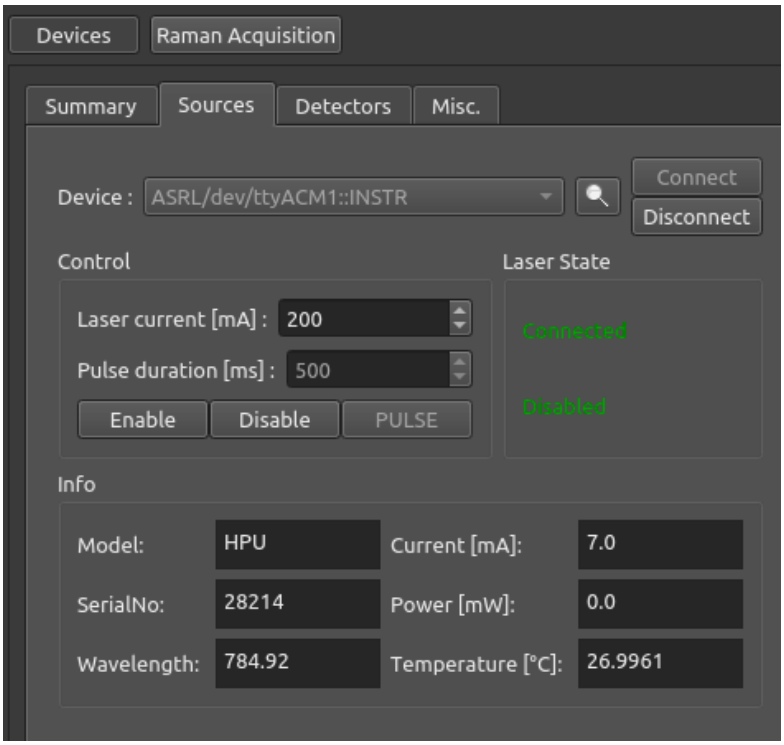

Figure 4.3 User Interface (UI) of the laser control module integrated as a widget in the *Sources* pane (i.e. tab) in the *ORAS* software.

The user graphical interface was designed for surgical application use cases. It allows the minimum level of control necessary to operate the laser in that context. More advanced functionalities also exposed by the laser controller module are reserved for specialized research

purposes. The first section of the UI manages device connectivity via USB. The *Control* section enables users to adjust the laser current, toggle its enabled state, and generate pulses with specified durations. The *Laser State* section indicates whether the laser is connected or disconnected and if it is enabled or disabled. When the laser is turned on, a red icon accompanied by the text "Enabled" is shown to minimize ambiguity. The *Info* section provides real-time updates (refreshed every 100 ms) on laser model, current, power delivered at the module output, and temperature reported as per the lookup table last uploaded on the unit's board.

Finally, the system's output for laser excitation was originally designed for SC/PC optical fiber connectors. However, the endonasal probe presented in Chapter 3 features an SMA connector for excitation. To make the system compatible with the probe, the optical fiber connecting the laser module to the system's output was changed to match the probe's fiber, and a custom SMA-SMA connector was designed to replace the original SC/PC connector. This connector was manufactured using a 3D-printed component that secures a *Thorlabs* SMA to SMA mating sleeve (ADASMA) to the system's casing. Further details about this connector are provided in Appendix C.

4.2 Clinical laser safety

This section reviews the risks and precautions associated with the use of a class IIIB laser in a clinical study. The safety of the patient and the operating room staff are paramount and take precedence over all research objectives. The 785 nm continuous-wave (cw) laser excitation source is limited to a maximal power at the probe's output of 100 mW. The potential pathologic effect or injury associated with radiation exposure depends on the laser's wavelength. The principal risk involving a continuous wave near-infrared (NIR) laser consists of thermal effects. [110]. Infrared lasers can damage the eye by heating the retina, cornea, or lens and may cause thermal damage to other tissues such as coagulation, cauterizing, and burning. However, they are not associated with the photochemical risks that arise when dealing with shorter wavelengths.

Direct contact exposure to class IIIB infrared lasers can cause permanent eye damage. However, since the Raman probe laser beam is not collimated, its divergence quickly reduces the laser intensity with the distance traveled, eliminating the risk of harmful specular reflections. Laser exposure to the eyes at distances $\geq$ 1 cm from the probe's tip and for durations of $\leq$ 10 seconds is deemed safe with class IIIB lasers, as certified by the probe's manufacturer. The neurosurgeon and operating room staff are informed of this risk and advised to avoid close contact of the probe tip with their eyes. Moreover, the system's operator must always

verify the probe's tip position before enabling the laser.

Regarding the patient's safety and the risk of thermal damage to the various tissues intended to be probed, laser exposure can be assessed with the Maximal Permissible Exposure (MPE) set by ANSI Z136.1 standards for research laboratory laser safety [111]. The MPE is defined as the highest laser radiation to which an unprotected person may be exposed without adverse biological changes. It is primarily considered for accidental laser exposure, ensuring tissue integrity. However, exceeding the MPE does not necessarily result in tissue damage. According to ANSI Z136.3 laser safety in healthcare, intentional laser exposure for diagnostic purposes may exceed the MPE if the associated risks are warranted [112]. Before exceeding this limit, extensive testing of thermal doses and potential damages must be performed, which was not explored in this thesis.

Since multiple different tissues are intended to be probed, and to account for potential unwanted exposure, the MPE for skin is used in calculations as a conservative approach to minimize risks, as recommended by ANSI Z136.1 standards. Skin is a bigger infrared light absorber than most other tissues in the body due to its composition (e.g., melanin, hemoglobin) [113], making it more susceptible to thermal damage.

The exposure for cw lasers is defined as

$$E = \frac{P \cdot t}{A} \quad [\ \mathrm{J} \cdot \mathrm{m}^{-2}] \tag{4.1}$$

where P is the power in Watts, t is the exposition duration in seconds, and A is the limiting aperture to consider for tissue irradiance (spot size) in m^2.

The MPE defined for a laser wavelength of $\lambda \in [700 \text{ to } 1050]$ and a continuous exposure of duration $t \in 10^{-3}$ to 10 seconds is

$$\begin{aligned} \mathrm{MPE} &= 1.1 \times 10^4 \cdot C_4 \cdot t^{0.25} \quad [\ \mathrm{J} \cdot \mathrm{m}^{-2}] \\ C_4 &= 10^{0.002(\lambda - 700)} \end{aligned} \tag{4.2}$$

The system specifications used in the calculations to ensure compliance with the MPE are presented in Table 4.2. These values are also used to compute the MPE for the clinical study presented in Chapter 5.

Table 4.2 Relevant parameters for MPE computation.

Wavelength	785 nm
Laser type	cw
Exposure duration (t)	< 10 s
Spot size (A)	9.6×10^{-6} cm^{-2}

4.3 Endoscopic white light filtering

A significant source of artifacts for Raman spectroscopy measurements performed in a clinical setting is the presence of ambient lights [97]. In open surgeries, artifacts can arise from various light sources illuminating the tissue during measurements, including operating room lights and surgical microscopes. In transsphenoidal surgeries performed with endoscopic systems, the nasal cavity naturally shields the probed tissues from external light. However, the endoscopic system itself includes a potential artifact source: the white light integrated into the instrument, which is used to illuminate and visualize the surgical field displayed on operating room monitors, as illustrated in Figure 4.4.

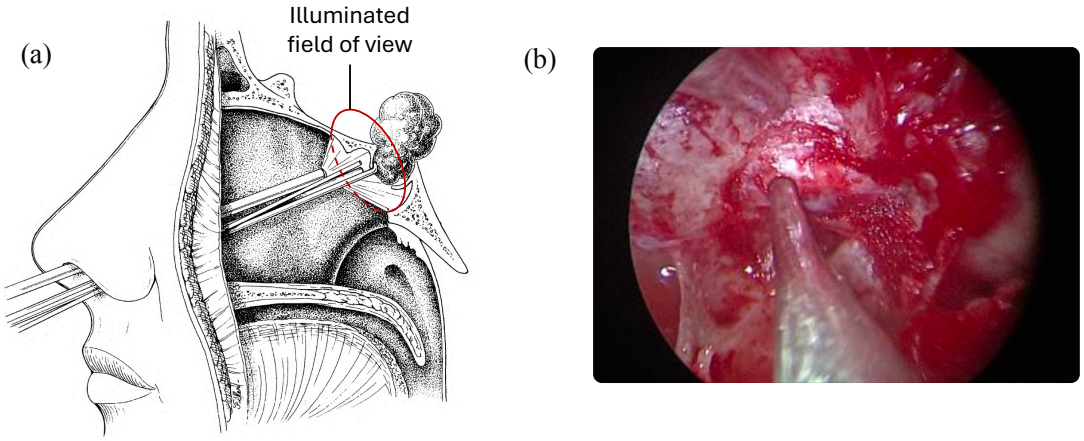

Figure 4.4 (a) Illustration of endoscopic transsphenoidal surgery of a pituitary adenoma through a nostril. The illuminated field of view is illustrated in red. Adapted from [10] with permission. (b) Endoscopic image of the field of view, illuminating an instrument, such as the Raman probe during measurements.

While this white light is essential for the surgeon's visibility, it also emits NIR wavelengths within the detector's range. These NIR components can scatter within the illuminated tissue and introduce unwanted spectral contributions, leading to artifacts in the processed Raman spectra. Requiring light sources to be turned off during intraoperative spectral acquisition can be impractical and slow down the procedure. Furthermore, the neurosurgeon must see

the tissues he intends to discriminate with the probe.

A first approach to mitigate the spectral contribution from broadband lights is the subtraction of a background measurement from the spectral acquisition. As described in section 3.3.6 covering spectral processing, a background measurement with the laser turned off is performed before Raman illumination to capture the "background" contribution to the spectra. This subtraction of the background is an effective tool to reduce the impact of external light illumination on Raman spectra. However, comparative studies have shown that this method may under-perform when the external light source contributes significantly to the acquired spectra [97]. Therefore, when possible, appropriate filtering of the white light contribution should be performed without impacting the visible illumination needed for the surgical procedure.

To assess the impact of endoscopic white light on Raman spectroscopy measurements, an experiment was conducted in collaboration with personnel at CHUM, where the clinical study presented in Chapter 7 was planned. The experimental setup, shown in Figure 4.5 was designed to simulate *in vivo* conditions. The endoscope was held in place to illuminate the Raman probe's tip at a distance of approximately 10 cm, and filter holders were mounted at the endoscope's tip to evaluate the impact of filters on endoscopic light artifacts with various samples.

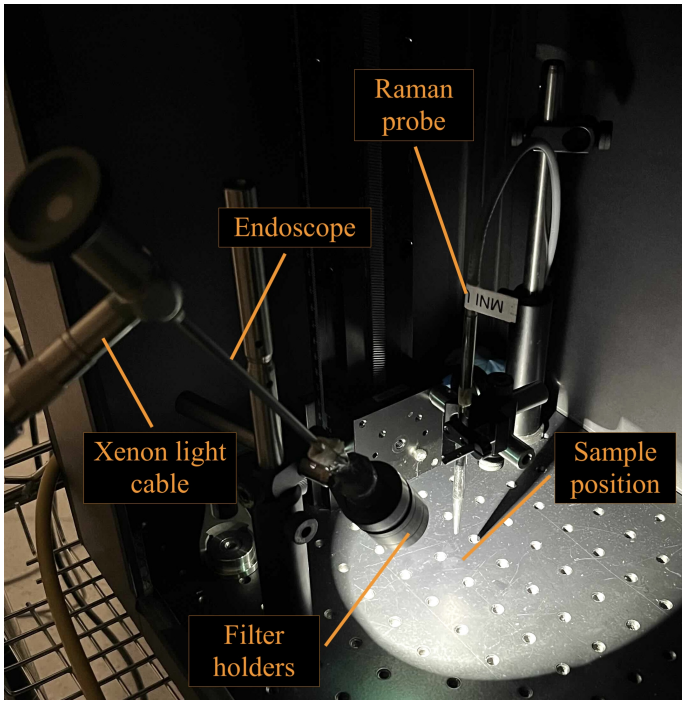

Figure 4.5 Experimental setup designed to simulate *in vivo* endoscopic light illumination.

The xenon light source used in the endoscope (Karl Storz Telescope Hopkins II) of the CHUM emits infrared light within the spectral range used for Raman spectroscopy, approximately 810 to 931 nm (∼400 to 2000 cm^{-}1). This contribution in the spectrometer range was acquired with a fixed exposure time of 500 ms at different light intensities (Figure 4.6a). The intensity is adjustable and the manufacturer advises against increasing it beyond 50% during operations to avoid excessive heating [114].

A Short-Pass (SP) filter with a cut-off wavelength below 780 nm (excitation wavelength) can be used to reduce the contribution of endoscopic light to the spectral range of interest. However, to avoid impacting the visibility of the surgeon, the cut-off wavelength must be above the visible wavelengths ($\gtrapprox$ 750 nm). A SP filter with a cut-off wavelength of 750 nm and an Optical Density (OD) 6 was selected for this purpose. When the filter was placed in the filter holder at the endoscope's output, the intensity of the endoscopic light contribution was significantly reduced (Figure 4.6b).

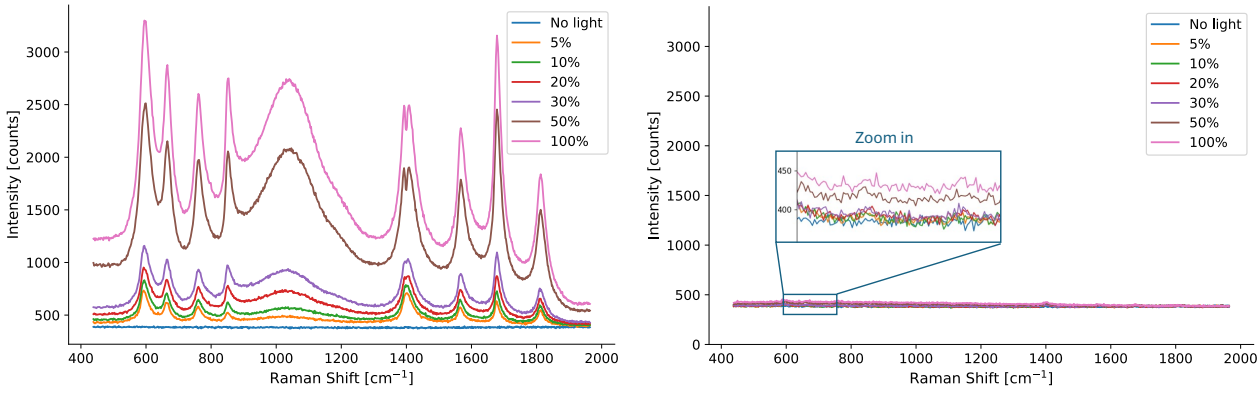

(a) Endoscopic light

(b) Endoscopic light with a 750 nm SP filter OD6

Figure 4.6 Spectral acquisitions of the endoscopic light at different intensities with a fixed exposure time of 500 ms. (a) No filter (b) 750 SP filter placed at the endoscope's output. A section of the figure is zoomed in in a blue frame to showcase intensity variations.

With the filter in place, the spectral intensity of the endoscopic light was reduced to a level comparable to the usual noise (thermal noise, readout noise, and shot noise) observed in measurements taken without any light. This reduction was observed for all light intensities, with a slight increase (<20% of noise level) when the light was set to 100% intensity. This result is promising, but it does not guarantee an absence of impact on Raman spectra, especially since the spectral intensities were not compared with those of the Raman peaks.

4.3.1 Impact of the light on porcine tissues measurements

The impact of endoscopic light on Raman acquisitions of biological samples was assessed using porcine tissues. Fat and muscle samples were selected for their distinct optical and Raman scattering properties, providing a representative model of the diversity of biological tissues encountered in surgical applications. These two tissues differ significantly in optical opacity, affecting the amount of transmitted light reaching the Raman probe, and exhibit distinct responses to laser illumination, characterized by differing Signal-to-Baseline Ratio.

To ensure consistency in the analysis, a fixed contact position was maintained for both samples, and multiple measurements were performed under varying endoscopic light intensities, both with and without the optical filter. All measurements were acquired during a fixed exposition time of 1500 ms. The unprocessed spectra (prior to baseline removal) at different light intensities for both tissues, without the filter, are shown in Figure 4.7. These raw measurements illustrate the lower opacity of muscle, which results in a higher contribution of endoscopic light to its measurements. The variation in SBR between the tissues is evident, with Raman peaks being approximately an order of magnitude higher in fat compared to muscle.

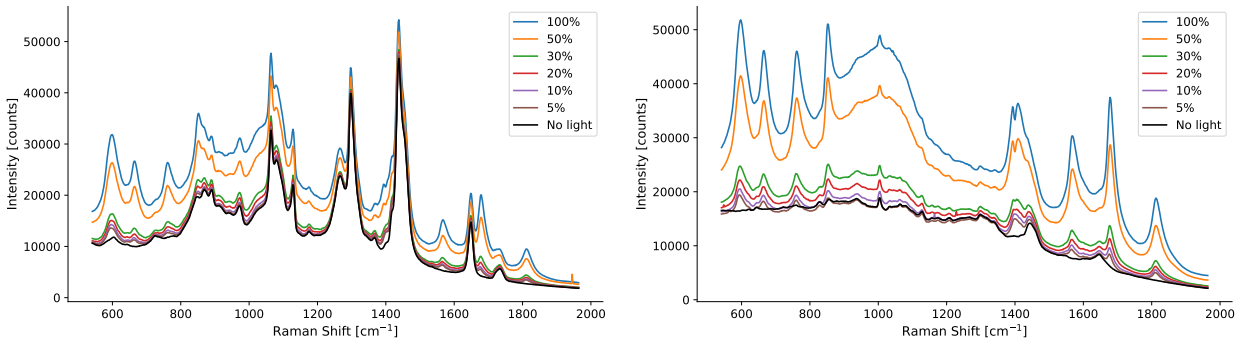

(a) Fat (b) Muscle

Figure 4.7 Impact of the endoscopic light at different intensities on unprocessed spectral acquisitions of porcine samples at a fixed position.

During data processing, baseline removal using the *Bubblefill* algorithm eliminates the broad spectral contribution of the endoscopic light, leaving only narrow residual peaks comparable to Raman peaks, as shown in Figures 4.8a and 4.8c. These residual peaks may interfere with spectral analysis by altering Raman peaks associated with the sample's molecular composition after SNV normalization. Even minor intensity variations can significantly affect the performance of ML models, particularly when distinguishing tissues with subtle molecular differences. The endoscopic illumination is more pronounced in muscle measurements, with

some white light peaks reaching nearly an order of magnitude higher than the Raman peaks. Figures 4.8b and 4.8d show the processed Raman spectra obtained using the SP filter. With the filter in place, the Raman spectra remain consistent across different levels of endoscopic light illumination, making them nearly indistinguishable from one another. The porcine tissue measurements reveal only minimal residual light artifacts, such as at 1821 cm^{-1}, which do not significantly alter the relative height of main Raman peaks often used for ML classification. Furthermore, these residual peaks can be further mitigated through numerical background subtraction.

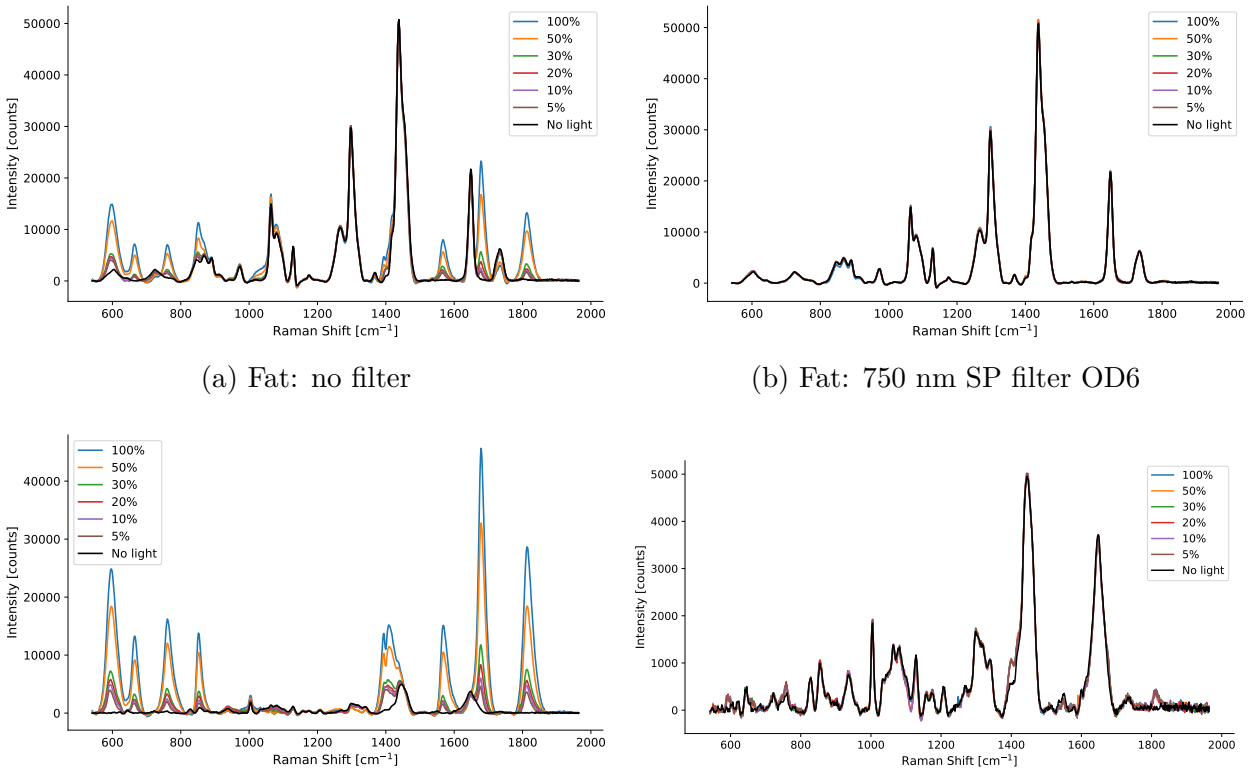

(a) Fat: no filter

(b) Fat: 750 nm SP filter OD6

(c) Muscle: no filter

(d) Muscle: 750 nm SP filter OD6

Figure 4.8 Impact of the endoscopic light at different intensities and its filtering on Raman spectral acquisitions of porcine fat and muscle at a fixed probe position.

Subsequently, five fixed measurement locations were selected in each sample to evaluate the spectral similarity of Raman spectra under varying illumination intensities, with and without SP filtering. At each location, the same light intensities as in the previously analyzed single measurements were tested. Two similarity metrics were employed to assess deviations from the reference spectra acquired without illumination. The Spectral Angle Mapper (SAM) focuses on spectral shape similarity by comparing relative intensities while being insensitive

to magnitude variations (see section 3.3.6), and the Mean Squared Error (MSE) captures both spectral shape distortions and intensity variations. For each measurement, both metrics were computed relative to the reference spectrum at the same location, then averaged across all locations. The results are represented in Figures 4.11.

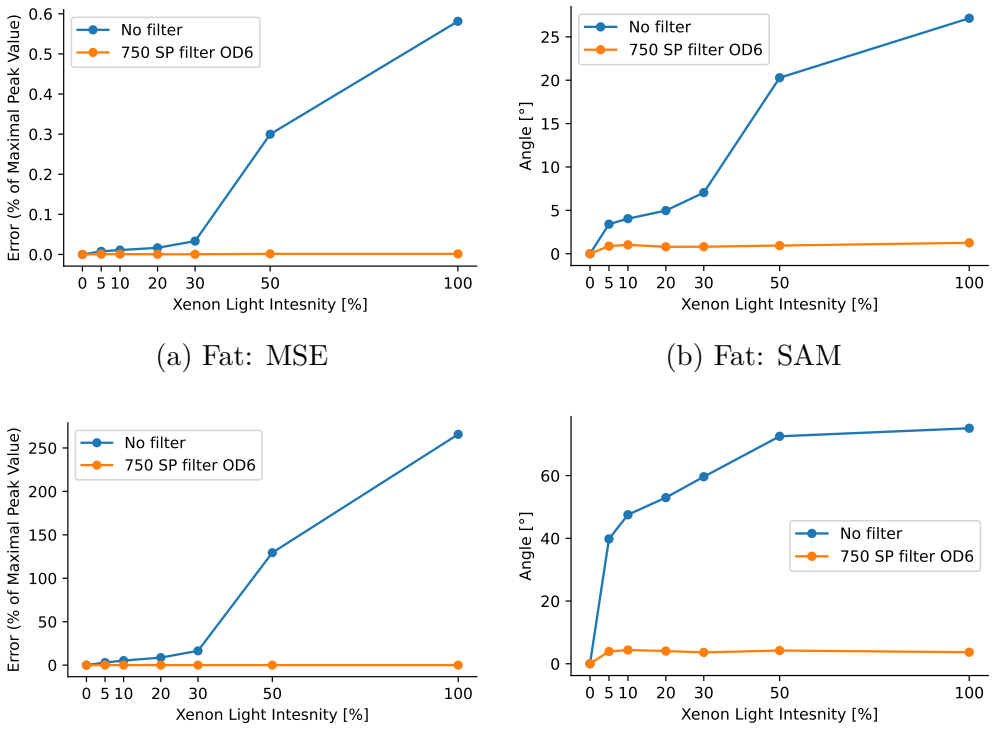

(a) Fat: MSE

(b) Fat: SAM

(c) Muscle: MSE

(d) Muscle: SAM

Figure 4.9 Comparison of the Raman measurements under different illumination conditions with the reference spectra. MSE and SAM values were averaged for 5 different measurement locations for each sample.

The MSE comparisons, shown in Figures 4.9a and 4.9c, were normalized to the maximal Raman peak intensity of each reference spectrum. These results highlight the effectiveness of the SP filter in preserving spectral similarity to the unilluminated spectrum in both tissues. The normalized SME values illustrate the greater susceptibility of muscle spectra to unfiltered light artifacts and the significant reduction of those artifacts for both samples when the filter is applied. The SAM comparisons (Figure 4.9b and 4.9d) remained below 2° for fat and under 5° for muscle at all light intensities with the filter. The comparison with the higher angles of the unfiltered measurements illustrates the filter's effectiveness. SAM values below 5° correspond to highly similar spectral profiles in terms of relative intensity across the entire range [100].

To further minimize white light artifacts, optical filtering could be combined with numerical background subtraction.

4.3.2 Application to the operating room

In the experiment, the filter was placed at the tip of the endoscope with a fixed filter holder (Figure 4.5). However, this is not reproducible during an operation in the context of a research project. The sterile *Karl Storz* endoscope, introduced inside the patient, cannot be heavily modified by a third party, especially with a component including the filter that could potentially detach inside the patient's body. However, the white light could be filtered before being injected into the endoscope. The xenon light source (Figure 4.10b) is connected to the endoscope with a fiber optic light guide (Figure 4.10a), which is screwed onto the endoscope with connector A, as shown in Figure 4.5.

(a) Karl Storz Fiber Optic Light Cable, 230cm, Ø3.5mm 495NA

(b) Karl Storz 300 Watt SCB Xenon Light Source

Figure 4.10 Karl Storz illumination system used for surgical endoscopy.

The filter could be placed on the cable at connector B, which is inserted in the xenon light source. A cable prototype was realized with a 750 nm SP filter, shaped to match connector B, and attached with epoxy glue. Similarly to the experimental setup, this cable effectively filtered artifacts, while the visible light intensity remained unaffected. Unfortunately, the epoxy-ed filter detached when it was removed from the cable connector of the light source due to its "claw-like" internal metallic holders.

A solution for clinical endoscopic light filtering to minimize its contribution to spectral acquisitions is still under development. Ideally, this solution should be transposable to different endoscopic systems to allow compatibility with multiple hospitals.

4.4 Complete system for practical *in vivo* and *ex vivo* acquisitions

Based on the comparison of acquisition methods in the animal study and the discussion in section 3.5, it was determined to conduct *in vivo* acquisitions, prior to specimen removal, and *ex vivo* acquisitions on the resected specimens. Briefly, *ex vivo* acquisitions enable direct comparison with *in vivo* measurements by providing spectra less affected by surgical light, liquids, and contribution of neighboring structures. To facilitate these measurements, the Raman spectroscopy system was mounted on a cart for transport into the operating room, incorporating an ambient light isolation box for *ex vivo* measurements (Figure 4.11a). The complete system includes a medical-grade transformer, calibration materials, and appropriate cleaning supplies for the probes' tip (see 3.3.3).

The endonasal probe requires sterilization before each use in a patient to reduce the risk of infection. A sterilization case (Figure 4.11c) and a custom sterilization procedure, aligned with CHUM sterilization protocols, were transmitted to the appropriate personnel. A second hand-held Raman spectroscopy probe was manufactured to facilitate *ex vivo* measurement acquisitions and avoid using the contaminated endonasal probe after its use. This *ex vivo* probe, represented in Figure 4.11b has a straight shape and the exact same optical fibers and probe tip design as the endonasal probe to ensure reproducible acquisitions. Figure 4.11b shows the *ex vivo* probe fixed with a vertical translation mount to make precise close contact with the specimens, inside the ambient light isolation box. The sample in this picture is acetaminophen, used for x-axis calibration, correlating each camera pixel to a Raman shift.

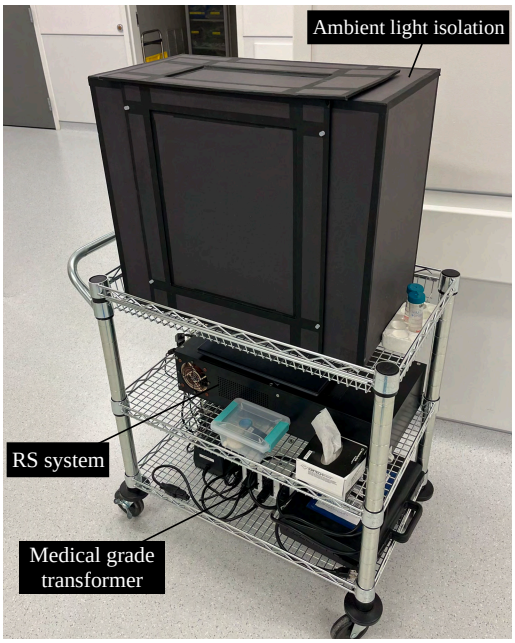

(a) Cart equipped with the Raman spectroscopy (RS) system, an ambient light isolation box, and a medical-grade transformer.

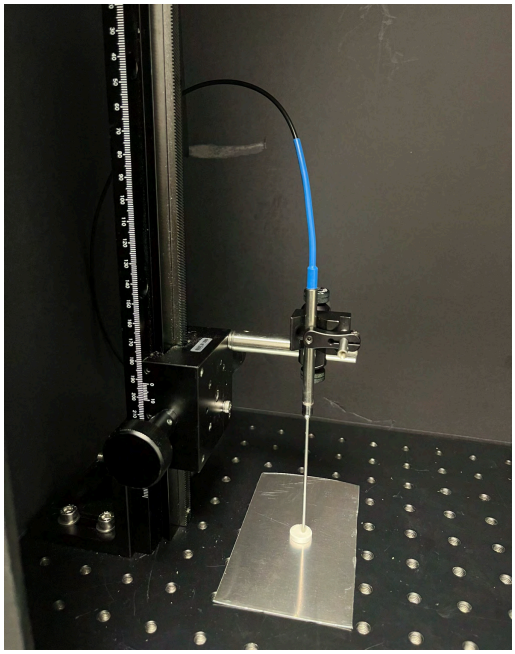

(b) *Ex vivo* probe acquisition on acetaminophen inside the ambient light isolation box.

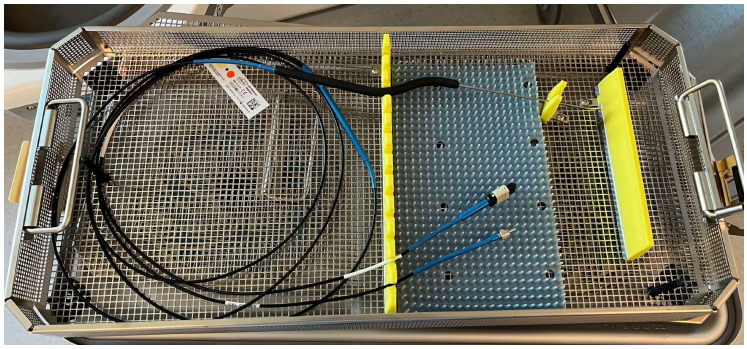

(c) Sterilization case with the endonasal probe

Figure 4.11 Complete system for practical *in vivo* and *ex vivo* Raman spectroscopy measurements in the clinical study.

CHAPTER 5 PRELIMINARY RESULTS OF THE SURGICAL CLINICAL STUDY

This chapter presents the clinical study, its preliminary results, and the challenges encountered. The first section outlines the objectives of the study, safety and ethics considerations, as well as the estimation of the sample size and study duration with statistical power analysis. The following section details the clinical acquisition protocols defined for both *in vivo* and *ex vivo* measurements. The third section covers the preliminary results of the clinical study, including data collected from eight tumor resection surgeries. The chapter concludes with a discussion of the challenges associated with intraoperative measurements, such as unintended signal sources, and a brief evaluation of the safety and feasibility of the study thus far.

5.1 Context

The promising results from the animal study, combined with the validation of the probe's design and safety by the CHUM neurosurgery team, paved the way for a clinical study. The research project, titled *"Détection de l'adénome hypophysaire à l'aide de la sonde Raman in vivo et ex vivo"*, was initiated at the CHUM under ethics protocol number 23.55, with neurosurgeon *Moujahed Ladibi* as the primary researcher.

The clinical study aims to collect Raman spectroscopy measurements of critical structures involved in the surgical resection of tumors within the parasellar region, with the aim of training classifiers to detect surgical abnormalities. These measurements are performed both *in vivo* on tissues prior to their resection, and *ex vivo* on the specimens after resection. The primary objective is to acquire spectra of normal (healthy) pituitary gland and pituitary adenomas. Given the probe's ability to access the entire parasellar region, the study's scope was expanded to include other tumors in this area, which also require intraoperative diagnostic techniques [6]. This approach facilitates *in vivo* acquisitions of normal pituitary gland tissue during the resection of unrelated tumors, without relying solely on resection errors to obtain spectra of the healthy glands. The secondary objective is to measure Raman spectra of various critical structures during the procedure to provide surgical guidance with real-time tissue mapping for improved procedural safety.

Study participants provided their informed consent to participate in the clinical study after receiving a consent form and detailed explanations. This process was conducted by a third party, specifically a member of the *Lumed Lab*, independent of the medical team, to avoid

any undue influence or authority bias in their decision-making. Patient and staff safety remains the highest priority, taking precedence over all research objectives. The endonasal probe undergoes decontamination and sterilization before each case, and laser safety was addressed in section 4.2. To avoid interfering with the surgical decision-making, no classification information is provided to the surgeon during data collection.

5.1.1 Statistical power and sample size

In ML applications, achieving high classification performance on a small dataset does not guarantee the detection of meaningful differences or patterns across all possible instances of the classes. A statistical power study helps determine the sample size required to draw reproducible conclusions and to minimize the risk of failing to detect a real effect. The classification of pituitary glands and adenomas—the primary research goal—is used to determine the required sample size. The diagnostic and prognostic value of the study are both considered.

An effect size-based calculation was performed to evaluate the sample size necessary to obtain a clinically relevant effect. It is hypothesized that there is a statistically significant difference in mean spectral fingerprints between normal tissue and adenomas. The study assumes a standard effect size $d = 0.2$, estimated conservatively compared to the effect size of 1 found in statistical analysis of over 400 Raman spectra of normal brain and glioblastomas. [59]. This value represents the anticipated magnitude of the difference between the mean spectral fingerprints of the two groups while accounting for variance. A class imbalance of 0.6 is considered to ensure a realistic representation of the dataset, which should have fewer healthy gland measurements. A significance level threshold $\alpha = 0.05$ was applied to control type I errors, and the statistical power of the test was set to 95% to ensure sufficient sensitivity to detect true differences. Given these parameters, 1400 total samples are required to ensure this statistical power with a two-sample t-test (G*Power 3.1 [115]). Based on prior studies, it was estimated that 20% of the data might be excluded due to quality issues, necessitating adjustments to the sample size, which is now 1750 samples.

In addition to considering the effect size, it is crucial to consider ML performance in the sample size calculation. Even if statistical differences do exist, the model's ability to capture and classify these differences must also be addressed. Briefly, to achieve 90% sensitivity and specificity, with a maximal permissible error of 5%, (L = 0.05), the required sample sizes are 196 pituitary adenoma samples and 139 pituitary gland samples. These sample size calculations, based on ML performance, are less limiting than the statistical effect size analysis.

Regarding the duration of the study to detect a significant effect, the estimation of 8 specimens per patient leads to 220 patients, which corresponds conservatively to a study lasting 5 years with approximately 50 patients per year.

5.2 Clinical Raman spectroscopy acquisition protocol

All acquisitions performed during the procedure are determined by *Dr. Labidi* and do not interfere with the surgical resection objectives. The probed tissues correspond to anatomical structures resected for debulking during the approach or tumor removal. No specimen is resected solely for research purposes. To ensure accurate labeling of each spectral acquisition, histopathological analysis of the specimens is conducted under the supervision of *Dr. Romain Cairol*. This step is crucial for ML applications, as accurate labels are essential for developing reliable classifiers trained on this data.

To expand the dataset without relying solely on healthy tissue obtained from resection errors, additional measurements are taken on unresected normal pituitary glands during unrelated tumor resections, provided the surgeon is fully confident in their healthy nature. Statistical comparison with the histopathology-confirmed data should be performed before including these spectra in ML models.

5.2.1 *In vivo* acquisitions

During the procedure setup, the sterile endonasal probe is connected to the Raman spectroscopy system and placed onto the surgical tray by the qualified operating room staff to ensure sterility and perform *in vivo* acquisitions. As with other instruments, the probe is inserted in the nasal cavity opposite to the endoscope, as shown in Figure 5.1a. Each Raman spectroscopy measurement is performed on a tissue before its resection (Figure 5.1b), with only one *in vivo* acquisition conducted per specimen. To document each measurement, a screen capture of the endoscopic view is taken for each measurement. The neurosurgeon then inserts an instrument to simulate the probe's position, capturing a neuronavigation image for subsequent data analysis, as illustrated in Figure 2.1. Finally, the specimen is resected and labeled for spectral correlations with histopathology reports.

To minimize the contribution of blood in Raman spectra, the region surrounding the probe is cleared of blood using dedicated suction devices before and during the measure. To reduce the white light contribution discussed in section 4.3, the endoscopic light is dimmed to 5% during the measurement and restored to its previous intensity immediately afterward.

The Raman spectroscopy system (Figure 4.11a) is operated by a qualified *Lumed lab* member

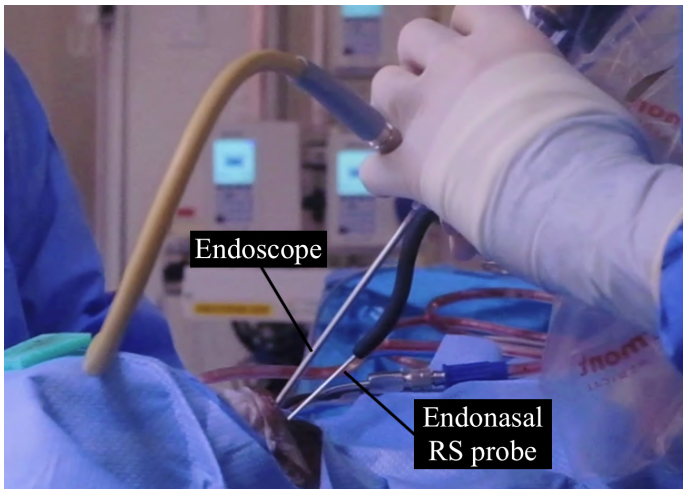

(a) Conjunctive use of the endonasal Raman spectroscopy probe and endoscope.

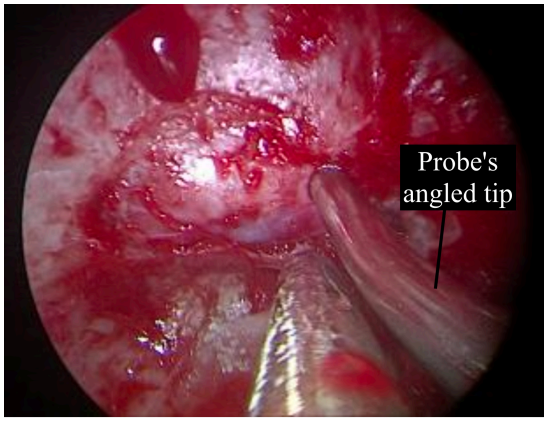

(b) Endoscopic view showing the angled tip of the Raman spectroscopy probe positioned on a pituitary adenoma to acquire a measurement.

Figure 5.1 Intraoperative use of the endonasal Raman spectroscopy probe.

(i.e. the author so far) using the custom *ORAS* software. Acquisitions are triggered once the surgeon positions the probe in contact with the tissue and gives the command. Laser power and exposure duration are controlled to ensure all acquisitions remain within the Maximal Permissible Exposure (MPE) of the skin (section 4.2). A maximum total exposure time of 4 seconds was selected to enable rapid interrogation.

5.2.2 *Ex vivo* acquisitions

Ex-vivo acquisitions are conducted on resected specimens after all *in vivo* measurements are completed. The specimens are fixed in formalin after their interrogations, within an hour from their removal. This timeframe was approved by histopathology clinicians and considered an acceptable part of the post-surgery clinical diagnostic workflow. To minimize Raman spectral contributions from the underlying material, the specimens are placed on an aluminum plate and shielded from ambient light, as shown in Figure 4.11b. They vary in size, typically ranging from a few millimeters to 5 centimeters in diameter, depending on the tissue type and surgical requirements. One to five acquisitions are performed on each specimen at different locations, depending on their size, with an approximate 4 mm margin (twice the diameter of the probe tip) between each measurement.

For *ex vivo* measurements on specimens, the total exposure limit was increased to twice the MPE, and histopathologists verified the absence of thermal damage.

5.2.3 Spectral measurements

Each spectral measurement consists of averaging N spectral accumulations. The exposure time of individual accumulations is automatically adapted through *ORAS* using Automatic Exposure Control (AEC) to maximize the photonic count while avoiding CCD sensor saturation [95]. The number of accumulations N is maximized given the total exposure time of the measurement to increase spectral quality [95].

5.3 Spectral fingerprints of tumors and healthy tissues

This section covers the preliminary results of the spectral measurements obtained during the clinical study, which involved tumor resection surgeries on eight different patients. Due to the limited size of the dataset relative to the scope of the study, no ML classifier was developed at this stage.

5.3.1 Spectral data processing and dataset

The spectroscopic data pre-processing steps applied to each raw spectroscopic measurement are described in section 3.3.6. However, curve smoothing with a Savitzky-Golay filter (step 6) was omitted to accurately represent tissue differences. Each individual processing step (e.g. calibration, cosmic ray removal, subtraction of the background measurement) was monitored for all spectral acquisitions. Labels were validated and corrected based on histopathology reports, with instances such as a pituitary adenoma being reclassified as normal glandular tissue.

Unlike the approach used in the animal study (section 3.3.6), no spectra were excluded from the dataset based on a Quality Factor (QF) threshold. This decision was made to include tissues with lower spectral quality in this small dataset. However, it is highly recommended for further ML development as it has been shown to increase cancer detection sensitivity and specificity [95]. Spectra were discarded from the dataset after evaluation of two criteria: (1) excessive contribution of endoscopic light and (2) significant blood (i.e. hemoglobin) contribution to the spectral acquisition. The selection criteria and their impact on spectra are discussed in section 5.4.

Before filtering, the total dataset included 31 *in vivo* spectra and 162 *ex vivo* spectra. Three acquisitions were removed due to light contribution (*in vivo*) and 10 were removed due to blood contribution (7 *in vivo*, 3 *ex vivo*). Table 5.1 presents an overview of the clinical dataset derived from the 8 cases. It includes, for each tissue type, the number of patients, the number

of retained acquisitions for both *in vivo* and *ex vivo* methods, and the number of spectra excluded from the dataset due to contributions of endoscopic light or blood. Some tissues were grouped into broader categories, despite the more specific labels originally provided by the surgeon. For example, the *bone* category regroups the following cortical bone structures: sella turcica bone, dorsum sellae, clivus, nasal concha, sinus bone, and petrous bone.

Additionally, measurements were performed on blood clots to analyze the spectral fingerprint of blood contribution. For tissues where blood presence is expected, such as blood clots, cavernous sinus, and cavernomas, no spectra were excluded due to blood contribution. The cavernous sinus is composed of blood vessels, while cavernomas are vascular malformations made up of abnormal tangles of blood vessels [116].

Table 5.1 Summary of the clinical dataset acquired during 8 tumor resection surgeries.

	Tissues type	**Patients**	**Selected acquisitions (*in*/*ex*)**	**Discarded (light/blood)**
Disease	Pituitary adenoma	5	60 (6/54)	(0/0)
	Craniopharyngioma	1	16 (2/14)	(0/0)
	Chondrosarcoma	1	7 (1/6)	(0/0)
	Cavernoma	1	5 (0/5)	(0/0)
Normal	Pituitary gland	4	10 (2/8)	(0/0)
	Dura mater sella turcica	6	19 (2/17)	(1/5)
	Mucosa	4	23 (0/23)	(1/4)
	Bone (cortical)	4	20 (1/19)	(0/1)
	Cavernous sinus	3	10 (5/5)	(1/0)
	Blood clot	3	11 (2/9)	(0/0)

While this may provide valuable insights and should be considered in future analysis, no comparisons between the two acquisition methods were made at this stage of the project due to the limited number of *in vivo* measurements collected for individual tissue types. Beyond their role in evaluating the intraoperative contribution of unwanted signals in *in vivo* acquisitions, *ex-vivo* acquisitions significantly increase the size of the dataset by enabling multiple measurements at different locations on a given sample. This is particularly important, as a larger dataset could enhance the performance of future ML models.

5.3.2 Average Raman spectral fingerprints

A preliminary attempt to characterize the Raman spectral fingerprint of each tissue in the dataset is presented in this section. Figure 5.2 presents the average SNV-normalized Raman spectra and the variance for both tumor (5.2b) and normal tissues (5.2a). The SNV-

normalized Raman spectra of blood clot, cavernous sinus, and cavernoma are presented in Figure 5.3, considered separately due to their specific hemoglobin-related spectral signature.

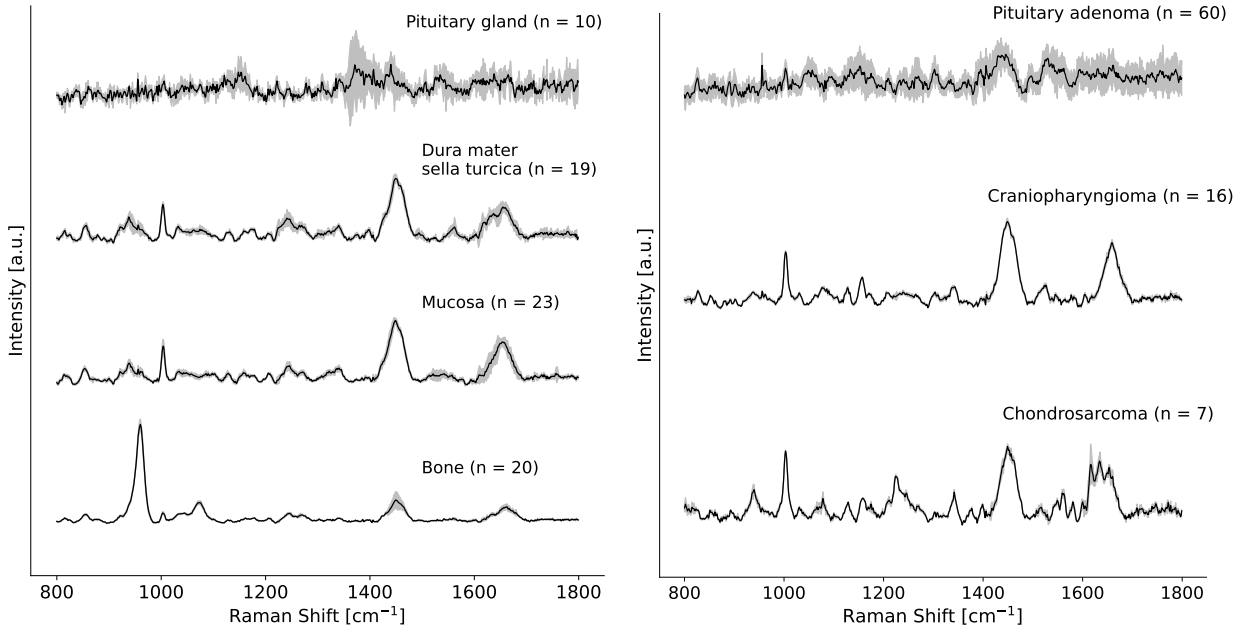

(a) Normal tissues

(b) Tumors

Figure 5.2 Average SNV-normalized Raman spectral fingerprints of (a) normal tissues and (b) tumors, with their spectral variance represented in grey.

Since SNV-normalized spectra do not reflect intensity variations in photonic counts across tissues, differences in noise levels are observed. A key finding is the reduced signal quality of pituitary glands and adenomas, characterized by increased noise, greater variance, and less distinct peaks. This lower signal quality compared to other tissues is further supported by their lower average Quality Factors (QF), presented in Table 5.2 with those of the other tissues. The signal from the pituitary gland appears predominantly as noise, with a potential Raman contribution around 1400 cm^{-1}. In contrast, the pituitary adenoma's signal exhibits subtle peaks at 1150, 1439, and 1532 cm^{-1}, which may correspond to Raman scattering, likely associated with fatty acids, lipids, and proteins, respectively [51, 53].

Apart from these two specific tissues of interest, high-quality Raman spectra (QF $>$ 0.3) were obtained for all other tissues, meeting the standards of previous studies realized with similar systems [59,67]. Among these tissues, bone exhibited the highest QF (0.78), while the cavernous sinus showed the lowest (0.32). Several factors may influence the QF, including the Signal-to-Baseline Ratio of the tissue, signal contamination, uneven probe contact, and other experimental variables, which are further explored in the following sections. Notably,

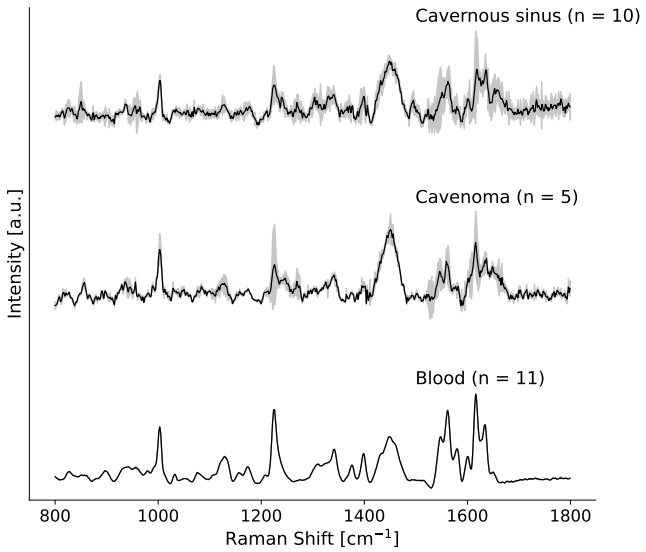

Figure 5.3 Average SNV-normalized Raman spectral fingerprints of tissues with important hemoglobin contribution, with their spectral variance represented in grey.

chondrosarcoma and craniopharyngioma spectra, which exhibited high QF values, appear distinguishable from structures requiring differentiation during surgery, such as the dura mater, cavernous sinus, and pituitary gland. These findings are promising for clinical applications of the probe and support further investigation into its use in the guidance of the resection of various parasellar tumors.

A brief biomolecular assignment of the principal Raman peaks and their presence in each tissue is described. For a more comprehensive review of the assignments and the associated vibrational modes, interested readers are referred to Table 3.1. The 961 cm^{-1} peak, commonly referred to as the "mineral" peak and associated with calcium hydroxyapatite [50, 59], is only significantly present in the bone's spectra. Peaks associated with lipid and protein contributions, such as those centered around 1439, 1449, and 1650 cm^{-1} [51–53], are highly present in the dura mater and mucosa spectra, as well as in tumor tissues, such as craniopharyngioma and chondrosarcoma. The phenylalanine peak at 1004 cm^{-1} is present in most tissues' spectra, including a slight contribution in pituitary adenoma.

The weak intensity of the mineral peak and the strong lipid and protein contributions in the dura mater spectra from the sella turcica support the hypothesis that measurements obtained in lamb heads (section 3.4.1) include an underlying bone contribution. The spectral fingerprints of the dura mater in lamb appear to represent a mixed contribution of the dura mater and bone spectra presented here. These were acquired mostly with *ex vivo* samples, thus minimizing interference from neighboring structures. While comparisons between Raman

Table 5.2 Average Quality Factor computed for each subset of tissue type.

Tissue type	**N° spectra**	**Mean QF**
Pituitary adenoma	60	0.17
Craniopharyngioma	16	0.59
Chondrosarcoma	7	0.48
Cavernoma	5	0.45
Pituitary gland	10	0.14
Dura mater sella turcica	19	0.47
Mucosa	23	0.55
Bone	20	0.78
Cavernous sinus	10	0.32
Blood	20	0.54

spectra acquired in living humans and deceased animals should be approached with caution, the spectral fingerprints of tissues such as the mucosa and bone are quite similar to those acquired in the animal study, whereas the dura mater fingerprint differs.

The spectral fingerprint of blood, presented in Figure 5.3, is primarily composed of the Raman signature of hemoglobin, as reported in the literature [117, 118]. This signal exhibits high fidelity with minimal spectral variance. The spectra associated with the cavernous sinus and cavernoma appear to contain a substantial contribution from the invariant hemoglobin spectrum, which is easily distinguishable in the spectral region between 1530 and 1660 cm^{-1}. The high variance in these tissues likely reflects the heterogeneous blood vessel composition within the sampled regions.

Despite these findings, the dataset remains relatively small and unevenly distributed across tissue types, which may introduce bias and limit the generalizability of results. This limitation also applies to the analyses in the following sections.

5.3.3 Tissue response to laser illumination and fluorescence

The complete photonic response of the tissues to laser illumination, prior to baseline removal, can provide deeper insights into Signal-to-Baseline Ratio and Raman spectral quality, particularly for the low-quality spectra observed in the pituitary gland and pituitary adenoma. Blood, cavernous sinus, and cavernoma were not included in this section due to the distinct response of hemoglobin, which interfered with the analysis.

To enable comparison across tissues, all spectral measurements were normalized to laser power and exposure duration. The resulting normalized laser-induced tissue responses are shown in Figure 5.4, with the average spectral measurement in Figure 5.4a and the boxplot

of the photonic response summed over all spectral bins for each tissue presented in Figure 5.4b.

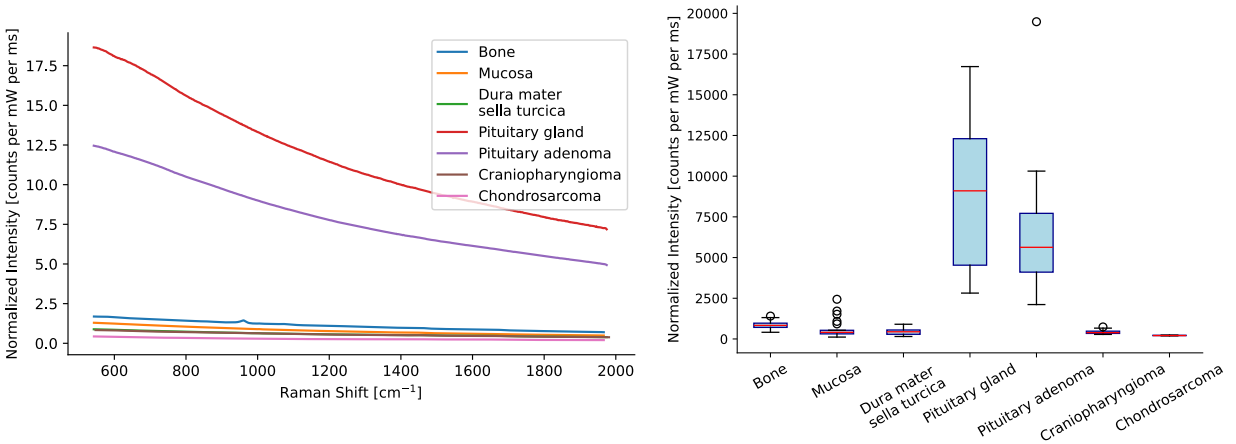

(a) Average photonic tissue responses to normalized laser illumination.

(b) Boxplot of total photonic tissue responses to normalized laser illumination summed over all spectral bins.

Figure 5.4 Comparison of laser-induced tissue responses across different tissue types. Normalization to laser power and exposure time enables consistent comparison of photonic responses.

The pituitary glands and pituitary adenomas exhibit significantly greater intensities in their photonic responses to laser illumination than all other tissues, with more than an order of magnitude higher photon counts for the same normalized laser exposure. This implies that, for the same delivered power, pituitary tissues will cause the camera's dynamic range to be filled more quickly, meaning the number of photonic counts per camera pixel will approach the saturation point of the CCD sensor. With Automatic Exposure Control (AEC), this results in shorter accumulation times and an increased number N of accumulations for a given total exposure time, as explained in section 5.2.3. The cause of this rapid saturation for pituitary tissues can be explored by examining the contributions of light-matter interactions to the measured signal.

The Signal-to-Baseline Ratio (SBR) represents the ratio between Raman scattering and fluorescence in spectral acquisitions. The signals corresponding to both interactions are separated during the baseline removal step of processing, with the *Bubblefill* algorithm described in section 2.2.8. To provide a metric comparable across tissue types, it is computed as the ratio of the summed signals over all spectral bins, rather than on specific Raman bands. The boxplot of the SBR across the different tissues is shown in Figure 5.5.

It can be observed that the SBR of pituitary tissues is lower than that of all other tissues.

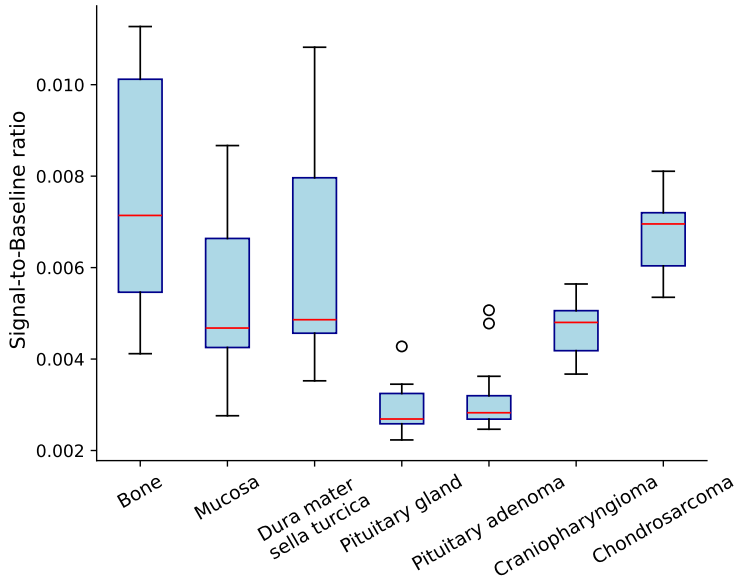

Figure 5.5 Boxplot of the Signal-to-Baseline Ratio (SBR) across the different tissues. This illustrates the ratio of Raman scattering to fluorescence.

This reveals that the rapid response to laser illumination is predominantly due to autofluorescence, explaining the reduced counts associated with Raman scattering, and, therefore, the lower quality of SNV-normalized Raman spectra. This difference in SBR, and consequently in the contributions of Raman scattering and fluorescence, is illustrated in 5.6 with two acquisitions performed at the same laser power (40 mW), respectively on bone and pituitary gland samples. For these acquisitions, each single accumulation, corresponding to the maximization of the detector's dynamic range, had a duration of 1440 ms for the bone and 102 ms for the pituitary gland.

Since the detector's dynamic range is already maximized, improving the SBR is essential to increase the total Raman count and enhance the quality of the Raman signal for pituitary tissues. Further investigation into the impact of acquisition parameters on the SBR is needed, and if these findings hold true with a larger dataset, potential solutions could involve probe or system improvements, or more advanced fluorescence reduction techniques. However, it's important to note that implementing such improvements could significantly increase the cost of the technology. This trade-off between performance enhancement and cost should be carefully considered for clinical applicability.

Given that fluorescence dominates the photonic response of pituitary tissues under laser illumination, its potential to be a distinguishable feature of adenoma and normal gland should also be investigated. Despite the challenges fluorescence poses for Raman scattering

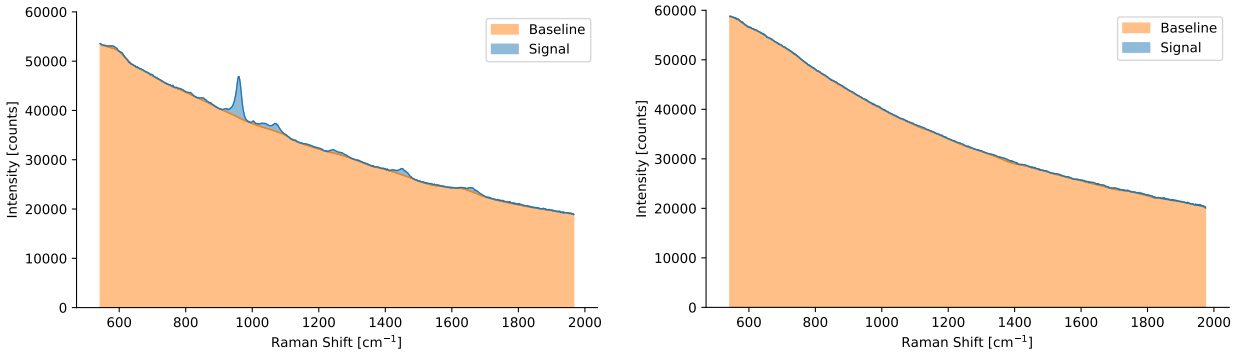

(a) Bone acquisition where each accumulation had a duration of 1440 ms.

(b) Pituitary gland acquisition where each accumulation had a duration of 102 ms.

Figure 5.6 Signal-to-Baseline Ratio illustration on specific acquisitions on the bone and pituitary gland, showcasing the different contributions of Raman scattering and fluorescence between different tissues.

collection, it could be valuable in differentiating these tissues, regardless of whether the SBR is improved. It may also be coupled with specific Raman peaks and other discriminative features of the tissue response in ML classification models.

While the current dataset does not yet allow for building a full ML model, we can explore potential classification features. From the current Raman spectra (Figure 5.2), the peak centered at 1441 cm^{-1}, associated with lipidic contributions, yields 74% sensitivity and 58% specificity in pituitary adenoma detection. Additionally, fluorescence, measured as the total baseline photonic count for a normalized laser exposure (Figure 5.4b), demonstrates an interesting 84% sensitivity and 66% specificity with a simple threshold. The normal gland appears to produce more autofluorescence than adenomas, which aligns with previous literature on fluorescence-based distinctions [42, 119].

5.4 Challenges associated with intraoperative Raman spectroscopy measurements

This section reviews the impact of unintended sources of signal contributing to the Raman spectral acquisitions. It discusses their effects on the spectra and the selection criteria used to discard spectra from the dataset.

5.4.1 Impact of endoscopic light on Raman spectra

The endoscopic light cable, specifically modified to filter the white light contribution, was not compatible with the surgical xenon light source, as discussed in section 4.3.2. Future work should focus on exploring more appropriate endoscopic light filtering techniques. To minimize the impact of the white light on measurements, the intensity was reduced to 5% during each acquisition. The white light artifacts were removed with numerical background subtraction, as part of the processing steps. Ideally, the presence of an endoscopic white light signal in *in vivo* acquisitions should be thoroughly compared to unaffected *ex vivo* acquisitions using statistical analysis or ML models to assess their discernibility after numerical background subtraction. However, the current dataset (Table 5.1) is limited in the number of acquisitions per tissue type for both methods, preventing such analysis at this stage.

To visualize the impact of the endoscopic light on *in vivo* measurements, the average background signal acquired with all 32 acquisitions (prior to data selection) is shown in Figure 5.7. The range of endoscopic light intensities, from minimum to maximum, across all background acquisitions is represented in semi-transparent form. To compare the intensities with Raman spectra, the maximum and the average of the highest peaks of each measurement were plotted in dotted lines.

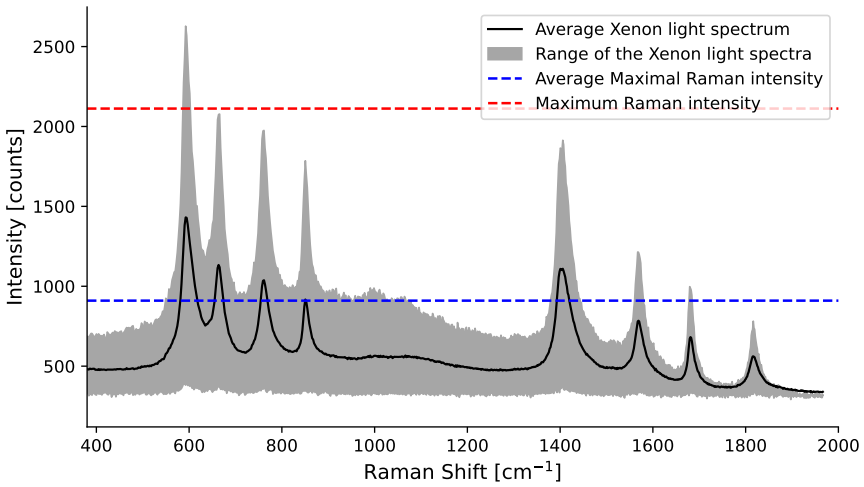

Figure 5.7 Comparison of xenon light intensities with Raman peak intensities over all 31 *in vivo* measurements. Xenon light intensities were measured as the background signal before each acquisition.

The comparison revealed that the peaks induced by white light have intensities comparable to the Raman spectra. This finding underscores the critical need for appropriate filtering of the infrared components of the endoscopic light before conducting measurements. The varying

intensity of the light may be attributed to several factors, including tissue transparency, as illustrated with pork samples in section 4.3, and the smoothness of the sample's contact surface with the probe.

During numerical background subtraction, the presence of residual white light peaks at their respective wavenumbers (cm^{-1}) was carefully monitored in spectral measurements before and after the subtraction. Three out of the 31 spectra were discarded because background removal was unsuccessful in eliminating all xenon peaks. The Raman spectral fingerprints presented in Figure 5.2 do not exhibit these peaks at their respective wavenumbers.

5.4.2 Impact of blood on Raman spectra

The presence of blood in some of the spectral acquisitions is difficult to control, as it is inherent to transsphenoidal surgeries. Although dedicated suction devices are used, blood may still be present between the probe and the intended surface of contact, as shown in Figure 5.8.

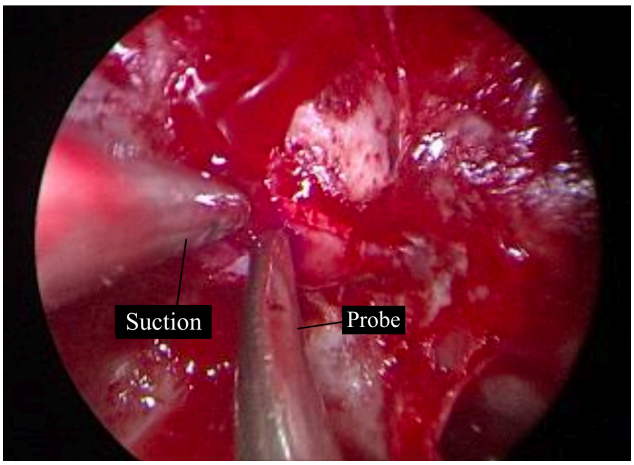

Figure 5.8 Blood contamination of *in vivo* measurements. Suction devices are used to minimize this effect.

The contamination of blood is characterized by the presence of Raman peaks of the hemoglobin in the measurement signal [117,118]. The relative contribution of blood was visually assessed to discard the contaminated samples. This process is illustrated with dura mater acquisitions in Figure 5.9, in which acquisition 1 appears to reflect the dura mater signal, while acquisition 2 seems to exhibit a mixed contribution with blood. A distinct feature of hemoglobin contamination is the presence of specific peaks in the spectral region between 1530 and 1660 cm^{-1}. In total, 9 acquisitions were removed from the dataset, including the measurement corresponding to acquisition 2 in Figure 5.9.

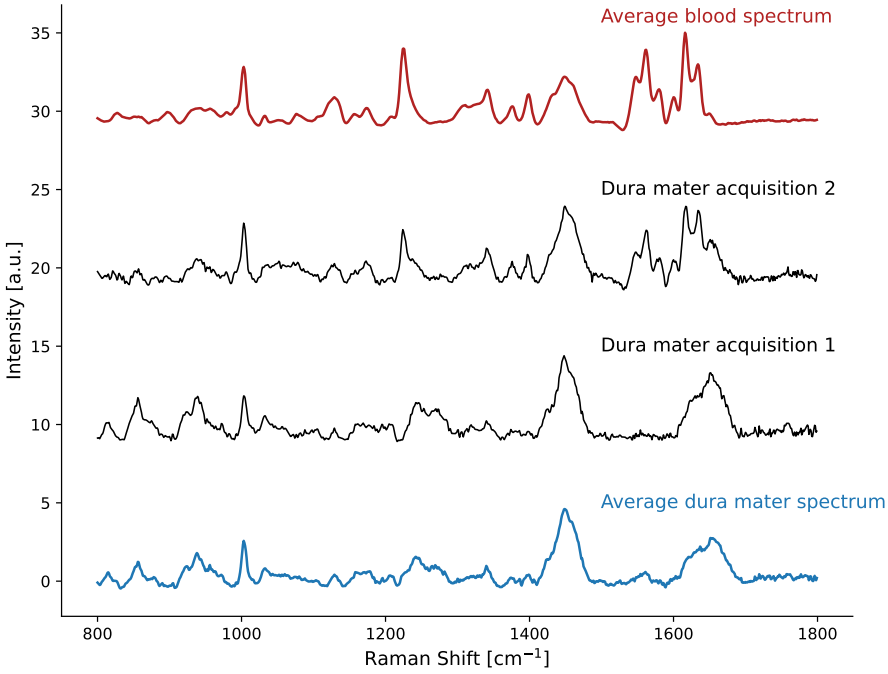

Figure 5.9 Illustration of blood (i.e. hemoglobin) contamination in tissue spectral acquisitions with examples from dura mater measurements. Acquisition 1 appears to reflect the dura mater signal, while acquisition 2 seems to exhibit a mixed contribution with blood.

Given the inherent presence of blood in transsphenoidal surgeries, automatic evaluation of the relative hemoglobin contribution to each measurement is necessary. To facilitate this, a dataset of measurements acquired on blood clots was initiated during the clinical study to train and test the automation of this task. The SAM metric could be applied either to the whole spectrum or specifically to the spectral region between 1530 and 1660 cm^{-1} to compare each acquisition with the hemoglobin Raman signature, providing a relative evaluation of the contamination. The SAM seems to be a suitable metric for this task as it evaluates spectral similarity independently of magnitude. This approach is not limited to this project and could be extended to any Raman spectroscopy measurements performed in surgical applications, either as part of data processing or during surgery, prior to ML classification for diagnostic needs.

5.5 Assesment of clinical safety and feasibility

Regarding laser safety, the Maximal Permissible Exposure of the skin was respected in all *in vivo* acquisitions, and no signs of damage or adverse effects from the laser illumination were observed during the postoperative follow-up with the consenting patients. This was

also consistent with numerous acquisitions performed in clinical studies on the brain [59], breast [67], and prostate [64], which adhered to the same MPE criteria. The analysis of the specimens by the pathologists did not reveal signs of thermal damages after the *ex vivo* acquisitions performed up to twice the MPE. The design of the probe was deemed safe by the operating room staff prior to the clinical study.

Regarding the feasibility and practical evaluation of the study, the design was deemed practical by the neurosurgeon, and the insertion into the cavity was facilitated by the 2.1 cm distal diameter. The angled tip effectively increased the reach and facilitated tissue interrogation with a smooth contact surface. This evaluation should, however, be validated by other neurosurgeons.

The time required to perform a single acquisition is 4 seconds, which could be further reduced by adjusting the acquisition parameters. However, the total acquisition time, including the spatial registration of the instrument for research and development purposes, is estimated to be 15 seconds. The total time added to the surgery, accounting for both installation and acquisitions, is estimated to be 15 min. Both of these parameters are quite promising when compared to the times mentioned for other diagnosis techniques presented in section 2.1.

CHAPTER 6 GENERAL DISCUSSION

6.1 Summary of works

The primary objective of this research project was to develop an optical instrument for intraoperative discrimination of pituitary adenomas. A comprehensive review of diagnostic techniques identified key parameters influencing diagnostic accuracy and clinical applicability. This review also highlighted the additional need for surgical guidance during the operations and detection tools for various parasellar tumors beyond pituitary adenomas. These insights led to the selection of Raman spectroscopy as the method to address the multiple clinical needs with molecular-based discrimination. This choice was motivated by recent advancements in RS, particularly its integration into fiber-optic instruments, enabling *in situ* interrogation, and the high diagnostic accuracy achieved in cancer detection [59].

A unique hand-held endonasal Raman spectroscopy probe was designed, developed, and evaluated, fulfilling research objective 1. The sterilizable instrument design was found to be compatible with current transsphenoidal endoscopic surgical workflows, enabling live interrogation of intracranial structures of the parasellar region. It was subsequently evaluated in an animal study, where it demonstrated highly accurate SVM classification of intracranial structures using Raman spectroscopy measurements in models specifically designed to simulate clinical needs.

These promising results laid the foundation for a clinical study. To prepare this study, as well as to support other ongoing projects within the *Lumed lab*, contributions were made to a general modernization of the RS systems. A laser control module and its user interface were developed for surgical applications. Additionally, endoscopic light interference was assessed with an experimental setup that simulated intraoperative illumination. Short-pass filtering effectively mitigated white light artifacts, though prototype compatibility with surgical systems remains an issue.

A clinical study was initiated at the CHUM, for which an ethics protocol was established, including laser safety and detailed acquisition protocols for both *in vivo* and *ex vivo* measurements. Practical, time-efficient, and safe acquisitions were performed on various tissues, including pituitary adenomas and other tumors, during eight transsphenoidal tumor resection surgeries using the upgraded RS system, equipped with the designed endonasal probe. A thorough analysis of the different spectral acquisitions obtained from this relatively limited dataset provided insight into tissue variations in spectral Raman fingerprints and fluores-

cence. Additionally, the impact of unwanted signals on Raman spectra, such as endoscopic light artifacts and Raman peaks originating from hemoglobin, was evaluated, along with an assessment of the safety and feasibility of the project.

The successful integration of the RS system into transsphenoidal surgeries and its ability to safely and effectively acquire diagnostically relevant intraoperative measurements validated research objectives 2 and 3.

6.2 Advantages of the proposed technology

Raman spectroscopy integrated into a fiber-optic probe enables minimally invasive, non-destructive, and real-time *in situ* interrogation, ensuring patient safety while providing molecularly specific information. This molecular specificity makes Raman spectroscopy a strong candidate for capturing the biochemical changes associated with the progression from healthy to tumorous tissue.

Previous studies have demonstrated the feasibility of pituitary adenoma differentiation *ex vivo* using resected specimens and Raman microspectroscopy systems [70, 71]. Additionally, successful *in vivo* differentiation of other tumor types has been reported [57], including studies using the *Lumed lab* system [59, 65, 67], which was optimized in this thesis. Although intense fluorescence in the pituitary glands and adenomas posed challenges in this study by reducing Raman signal quality, observed spectral differences support the feasibility of *in situ* Raman-based adenoma differentiation. Furthermore, the high-quality spectra acquired for other parasellar tumors and tissues highlight the strong potential of this new probe for a broader transsphenoidal application.

Many intraoperative diagnostic technologies rely on imaging, making their resolution a recurring limitation, particularly for small tumor detection, such as microadenomas. In contrast, the point-based interrogation of a Raman probe is independent of tumor size, offering an advantage for detecting small or residual tumors. It allows surgeons to perform localized tissue assessments, without altering their usual approach. This technology is label-free, eliminating the need for contrast agents, which can be time-sensitive and include additional preoperative steps in already complex surgical workflows.

The neurosurgeon who employed the probe judged the design practical for safe navigation in the cavity. It enabled rapid acquisitions in under five seconds, a substantial advantage compared to many previously explored detection techniques, which failed to achieve clinical adoption due to excessive acquisition times.

Finally, machine learning models trained on Raman spectra provide a powerful tool for tissue

differentiation, enabling the identification of new detection biomarkers associated with specific spectral features. ML also allows continuous classification values, which can help assess the gradient of diffuse tumor borders and provide confidence metrics for binary diagnosis. Additionally, transfer learning techniques facilitate the integration of data acquired with different systems or tumor types, potentially improving model accuracy and promoting the development of generalized models for broader oncological applications, such as generalized brain tumor detection [120].

6.3 Limitations

While the research objectives were generally validated and the technology showed promising results in the animal model and clinical study, several challenges and limitations were encountered and outlined below:

- The proposed diagnosis technique enables point-based interrogation, covering a surface of 500 μm diameter. While sufficient for localized tissue assessment, this may result in insignificant diagnostic information per measurement for delineating large tumors, such as macroadenomas. Comprehensive tumor mapping would necessitate multiple measurements, potentially overextending surgical duration and hindering clinical adoption.

- For thin tissues with thickness comparable to the probe's estimated depth of field (<600 μm), underlying structures can influence the acquired spectra. This was observed in the animal study, where dura mater measurements contained contributions from underlying bone. Though not observed in human patients with thicker dura mater, it highlights the general challenge of isolating the Raman signature of the target tissue from adjacent anatomical features, which may be present in the illuminated volume.

- In human patients, the Raman signal of pituitary tissues was inherently weak due to intense fluorescence, which maximized the sensor's dynamic range quickly. As a result, the SBR and quality of the acquired Raman spectrum were generally poor compared to the other probed tissues and may greatly affect the primary objective of differentiating adenomas.

- The endoscopic white light introduces spectral artifacts, with intensity levels comparable to Raman peaks. While experimental filtering demonstrated efficacy, no fully compatible filtering solution was successfully implemented for *in vivo* surgical measurements.

- The presence of blood is intrinsic to transsphenoidal operation and can result in hemoglobin contribution in the Raman spectra. This contribution may complicate spectral analysis and impact ML accuracy by introducing or modifying spectral features.
- The relatively small size of the dataset for the clinical study limited ML model development and the results and conclusions it allowed may not generalize to broader patient populations.

6.4 Future research

To further enhance the development of this probe as a practical and efficient tool for surgical guidance, future work should address its current limitations and explore the following areas:

- Continue and expand the clinical study: An increased sample size will capture the spectral signature of each tissue type more accurately and improve its understanding. Expanding the pituitary adenoma study to include other parasellar tumors, which can also be interrogated using the novel probe, has already yielded promising results and should be pursued. The other tumors probed so far were associated with high-quality spectra, showing great potential for their detection. Continuous fine-tuning aspects of the study, such as acquisition protocols and system settings, could significantly improve overall signal quality.
- Improve Raman signal quality in pituitary tissues: Previous work enabled significant improvements of the SNR, optimizing each measurement with numerous accumulations each maximizing the available dynamic range [95]. However, the low SBR observed in pituitary adenomas and glands remains a major limitation, reducing the quality of their Raman spectra. Simple approaches, such as further optimizing acquisition parameters, may increase the SBR without significant system modifications. Advanced fluorescence suppression techniques could be effective but would greatly increase the cost of the technology (section 2.2.8). Photobleaching could be explored as it requires minimal to no modifications to the laser illumination setup; however, its practical application within the constraints of the MPE may prove challenging. Modifying the probe's fiber-optic composition, such as using thinner fibers, could also enhance the SBR by increasing power density [121], though this may reduce overall power.
- Develop ML classification models addressing clinical needs: Continuous collaboration with neurosurgeons should be pursued to provide a tool tailored to their needs. Specifically, classifiers should be aimed at discriminating tumor types from surrounding normal

tissues, including the potential creation of subtype-specific classifiers for pituitary adenomas. The second identified need is a multiclass model to provide surgical guidance with differentiation of various parasellar tissues.

- Explore fluorescence for discrimination: Since fluorescence spectra are intrinsically measured with Raman, they could serve as complementary features in ML models for tissue discrimination. Multiple predictive factors could be extracted from the total spectral response and combined with Raman peaks to help mitigate the challenges associated with weak Raman signals from pituitary tissues. For instance, the observed higher fluorescence in normal pituitary glands compared to adenomas could aid in tissue classification. To implement this robustly, specific optical fibers of the probe could be dedicated to this modality.

- Address endoscopic light and blood interference: While numerical subtraction successfully reduced endoscopic light artifacts, a practical integration of the identified short-pass filter in a surgical setting is still needed to minimize this contribution. Additionally, automated detection and quantification of hemoglobin-related peaks could enhance model performances and provide real-time information on the presence of blood before classification for diagnostic-related measurement.

CHAPTER 7 CONCLUSION

This thesis lays the foundation for the integration of an endonasal Raman spectroscopy probe in transsphenoidal surgery for real-time tissue differentiation. Through instrument design, validation in an animal model, and clinical integration, the feasibility of intraoperative Raman spectroscopy for surgical guidance during parasellar tumor resections was demonstrated. The developed probe enabled the first-ever *in vivo* Raman acquisitions in the sella turcica cavity, including measurements on pituitary glands, adenomas, and various other intracranial structures and tumors. It provides minimally invasive, real-time (<5s), and safe interrogation, with machine learning models for tissue classification. To ensure clinical compatibility, safety, and efficiency, detailed acquisition protocols were implemented for *in vivo* and *ex vivo* measurements in the ongoing clinical study.

Although *ex vivo* studies successfully differentiated pituitary adenomas from healthy glands with Raman microspectroscopy and promising results were obtained with the developed probe in the animal model, its effectiveness for adenoma differentiation in human patients still needs to be established. Intense fluorescence from pituitary tissues, resulting in low signal-to-background ratios (SBR), was identified as a key challenge, along with unwanted spectral contributions from endoscopic light and blood. However, preliminary clinical results highlight strong potential for surgical guidance in the nasal and sella turcica cavities and for the detection of various tumors in this region.

Future research should focus on continuing the clinical study to increase the size of the clinical dataset and expand it, mitigating the fluorescence of pituitary tissues with probe improvements or fluorescence suppression techniques, and developing robust ML-based classification models tailored to clinical needs. With further advancements, this technology has the potential to improve tumor resection accuracy for transsphenoidal surgeries, reduce recurrence rates, and improve patient outcomes, contributing to the development of molecular-based approaches in neurosurgical diagnostics and guidance.

REFERENCES

[1] M. Buchfelder, S. M. Schlaffer, and Y. Zhao, "The optimal surgical techniques for pituitary tumors," *Best Practice & Research Clinical Endocrinology & Metabolism*, vol. 33, no. 2, Apr. 2019. [Online]. Available: https://www.sciencedirect.com/science/article/pii/S1521690X19300508

[2] S. A. El Sayed, M. W. Fahmy, and J. Schwartz, "Physiology, pituitary gland," in *StatPearls*. StatPearls Publishing, May 2023. [Online]. Available: http://www.ncbi.nlm.nih.gov/books/NBK459247/

[3] OHSU Brain Institute. Understanding pituitary disorders. [Online]. Available: https://www.ohsu.edu/brain-institute/understanding-pituitary-disorders

[4] S. Melmed, U. B. Kaiser, M. B. Lopes, J. Bertherat, L. V. Syro, G. Raverot, M. Reincke, G. Johannsson, A. Beckers, M. Fleseriu, A. Giustina, J. A. H. Wass, and K. K. Y. Ho, "Clinical biology of the pituitary adenoma," *Endocrine Reviews*, vol. 43, no. 6, pp. 1003–1037, Dec. 2022. [Online]. Available: https://doi.org/10.1210/endrev/bnac010

[5] S. Melmed, "Pathogenesis of pituitary tumors," *Nature Reviews Endocrinology*, vol. 7, no. 5, pp. 257–266, Mar. 2011. [Online]. Available: https://www.nature.com/articles/nrendo.2011.40

[6] S. Larkin and O. Ansorge, "Pathology and pathogenesis of pituitary adenomas and other sellar lesions," in *Endotext*. MDText.com, Inc., 2000. [Online]. Available: http://www.ncbi.nlm.nih.gov/books/NBK425704/

[7] M. E. Molitch, "Diagnosis and treatment of pituitary adenomas: A review," *JAMA*, vol. 317, no. 5, pp. 516–524, Feb. 2017. [Online]. Available: https://doi.org/10.1001/jama.2016.19699

[8] D. Gillett, J. MacFarlane, W. Bashari, R. Crawford, I. Harper, I. A. Mendichovszky, L. Aloj, H. Cheow, and M. Gurnell, "Molecular imaging of pituitary tumors," *Seminars in Nuclear Medicine*, vol. 53, no. 4, pp. 530–538, Jul. 2023. [Online]. Available: https://linkinghub.elsevier.com/retrieve/pii/S0001299823000119

[9] N. A. Tritos and K. K. Miller, "Diagnosis and management of pituitary adenomas: A review," *JAMA*, vol. 329, no. 16, pp. 1386–1398, Apr. 2023. [Online]. Available: https://doi.org/10.1001/jama.2023.5444

[10] H.-D. Jho, "Endoscopic transsphenoidal surgery," *Journal of Neuro-Oncology*, vol. 54, no. 2, pp. 187–195, Sep. 2001. [Online]. Available: https://doi.org/10.1023/A:1012969719503

[11] M. Buchfelder, "Treatment of pituitary tumors," *Endocrine*, vol. 28, no. 1, pp. 67–75, Oct. 2005. [Online]. Available: https://doi.org/10.1385/ENDO:28:1:067

[12] P. Cappabianca, L. M. Cavallo, F. Esposito, and E. de Divitiis, "Endoscopic endonasal transsphenoidal surgery: procedure, endoscopic equipment and instrumentation," *Child's Nervous System*, vol. 20, no. 11, pp. 796–801, Jun. 2004. [Online]. Available: https://doi.org/10.1007/s00381-004-0933-3

[13] J. Maletkovic, A. Dabbagh, D. Zhang, A. Zahid, M. Bergsneider, M. B. Wang, M. Linetsky, N. Salamon, W. H. Yong, H. V. Vinters, and A. P. Heaney, "Residual tumor confers a 10-fold increased risk of regrowth in clinically nonfunctioning pituitary tumors," *Journal of the Endocrine Society*, vol. 3, no. 10, pp. 1931–1941, Jul. 2019. [Online]. Available: https://www.ncbi.nlm.nih.gov/pmc/articles/PMC6777402/

[14] M. E. Sughrue, E. F. Chang, R. A. Gabriel, M. K. Aghi, and L. S. Blevins, "Excess mortality for patients with residual disease following resection of pituitary adenomas," *Pituitary*, vol. 14, no. 3, pp. 276–283, Apr. 2011. [Online]. Available: https://doi.org/10.1007/s11102-011-0308-1

[15] R. F. Dallapiazza, Y. Grober, R. M. Starke, E. R. Laws, and J. A. Jane, "Long-term results of endonasal endoscopic transsphenoidal resection of nonfunctioning pituitary macroadenomas," *Neurosurgery*, vol. 76, no. 1, pp. 42–53, Jan. 2015. [Online]. Available: https://journals.lww.com/00006123-201501000-00005

[16] M. H. Almalki, M. M. Ahmad, I. Brema, M. Almehthel, K. M. AlDahmani, M. Mahzari, and S. A. Beshyah, "Management of diabetes insipidus following surgery for pituitary and suprasellar tumours," *Sultan Qaboos University Medical Journal*, vol. 21, no. 3, pp. 354–364, Aug. 2021. [Online]. Available: https://doi.org/10.18295/squmj.4.2021.010

[17] A. Jahangiri, J. Wagner, S. W. Han, C. C. Zygourakis, S. J. Han, M. T. Tran, L. M. Miller, M. W. Tom, S. Kunwar, L. S. Blevins, and M. K. Aghi, "Morbidity of repeat transsphenoidal surgery assessed in more than 1000 operations: Clinical article," *Journal of Neurosurgery*, vol. 121, no. 1, pp. 67–74, Jul. 2014. [Online]. Available: https://thejns.org/view/journals/j-neurosurg/121/1/article-p67.xml

[18] J. H. Kim, J. H. Lee, J. H. Lee, A. R. Hong, Y. J. Kim, and Y. H. Kim, "Endoscopic transsphenoidal surgery outcomes in 331 nonfunctioning pituitary adenoma cases after a single surgeon learning curve," *World Neurosurgery*, vol. 109, pp. e409–e416, Jan. 2018. [Online]. Available: https://www.sciencedirect.com/science/article/pii/S1878875017317126

[19] D. Z. Khan, J. G. Hanrahan, S. E. Baldeweg, N. L. Dorward, D. Stoyanov, and H. J. Marcus, "Current and future advances in surgical therapy for pituitary adenoma," *Endocrine Reviews*, vol. 44, no. 5, pp. 947–959, Oct. 2023. [Online]. Available: https://doi.org/10.1210/endrev/bnad014

[20] N. T. Zwagerman, S. Lieber, and J. C. Fernandez-Miranda, "Surgical anatomy of the sellar region," in *Transsphenoidal Surgery: Complication Avoidance and Management Techniques*, J. Laws, Edward R., A. A. Cohen-Gadol, T. H. Schwartz, and J. P. Sheehan, Eds. Springer International Publishing, Sep. 2017, pp. 145–165. [Online]. Available: https://doi.org/10.1007/978-3-319-56691-7_10

[21] F. Janelle, V. Blanquez-Yeste, T. Tran, A. Khellaf, R. Cayrol, C. Beauregard, A. Lacroix, A. Weil, P. Lavigne, F. Leblond, and M. Labidi, "Challenges and opportunities for new intraoperative optical techniques in the surgical treatment of pituitary adenomas," Dec. 2024, submitted for publication.

[22] Y. Huang, L. Qin, H. Lv, S. Lv, and Y. Lu, "Neuronavigation-assisted pituitary neuroendocrine tumor resection: a systematic review and meta-analysis," *Quantitative Imaging in Medicine and Surgery*, vol. 14, no. 7, p. 5012, Jun. 2024. [Online]. Available: https://pmc.ncbi.nlm.nih.gov/articles/PMC11250324/

[23] Y. Enchev, "Neuronavigational neuroendoscopy—to be or not to be? an international pilot questionnaire-based study," *World Neurosurgery*, vol. 79, no. 2, pp. S16.e15–S16.e21, Feb. 2013. [Online]. Available: https://www.sciencedirect.com/science/article/pii/S1878875012001593

[24] A. A. J. d. Rotte, A. Groenewegen, D. R. Rutgers, T. Witkamp, P. M. J. Zelissen, F. J. A. Meijer, E. J. v. Lindert, A. Hermus, P. R. Luijten, and J. Hendrikse, "High resolution pituitary gland MRI at 7.0 tesla: a clinical evaluation in cushing's disease," *European Radiology*, vol. 26, no. 1, p. 271, May 2015. [Online]. Available: https://pmc.ncbi.nlm.nih.gov/articles/PMC4666272/

[25] N. G. Candy, A. K. Jukes, S. Patel, T. King, G. Bouras, N. Vrodos, P.-J. Wormald, and A. J. Psaltis, "Neuronavigation in endoscopic skull base surgery and the accuracy

of different MRI sequences," *Journal of Clinical Neuroscience: Official Journal of the Neurosurgical Society of Australasia*, vol. 123, pp. 203–208, May 2024. [Online]. Available: https://doi.org/10.1016/j.jocn.2024.04.006

[26] N. Qiao, B. Swearingen, E. T. Hedley-Whyte, and N. A. Tritos, "The utility of intraoperative cytological smear and frozen section in the surgical management of patients with cushing's disease due to pituitary microadenomas," *Endocrine Pathology*, vol. 30, no. 3, pp. 180–188, Jun. 2019. [Online]. Available: https://doi.org/10.1007/s12022-019-09582-5

[27] M. S. Eljamel, G. Leese, and H. Moseley, "Intraoperative optical identification of pituitary adenomas," *Journal of Neuro-Oncology*, vol. 92, no. 3, pp. 417–421, Apr. 2009. [Online]. Available: https://doi.org/10.1007/s11060-009-9820-9

[28] R. S. Pergolizzi, A. Nabavi, R. B. Schwartz, L. Hsu, T. Z. Wong, C. Martin, P. M. Black, and F. A. Jolesz, "Intra-operative MR guidance during trans-sphenoidal pituitary resection: preliminary results," *Journal of magnetic resonance imaging: JMRI*, vol. 13, no. 1, Jan. 2001. [Online]. Available: https://doi.org/10.1002/1522-2586(200101)13:1<136::aid-jmri1021>3.0.co;2-8

[29] H. A. Zaidi, K. De Los Reyes, G. Barkhoudarian, Z. N. Litvack, W. L. Bi, J. Rincon-Torroella, S. Mukundan, I. F. Dunn, and E. R. Laws, "The utility of high-resolution intraoperative MRI in endoscopic transsphenoidal surgery for pituitary macroadenomas: early experience in the advanced multimodality image guided operating suite," *Neurosurgical Focus*, vol. 40, no. 3, p. E18, Mar. 2016. [Online]. Available: https://doi.org/10.3171/2016.1.FOCUS15515

[30] P. S. Jones and B. Swearingen, "Intraoperative MRI for pituitary adenomas," *Neurosurgery Clinics of North America*, vol. 30, no. 4, pp. 413–420, Oct. 2019. [Online]. Available: https://www.sciencedirect.com/science/article/pii/S1042368019300397

[31] M. Buchfelder and S.-M. Schlaffer, "Intraoperative magnetic resonance imaging during surgery for pituitary adenomas: pros and cons," *Endocrine*, vol. 42, no. 3, pp. 483–495, Jul. 2012. [Online]. Available: https://doi.org/10.1007/s12020-012-9752-6

[32] J. S. Kuo, G. Barkhoudarian, C. J. Farrell, M. E. Bodach, L. M. Tumialan, N. M. Oyesiku, Z. Litvack, G. Zada, C. G. Patil, and M. K. Aghi, "Congress of neurological surgeons systematic review and evidence-based guideline on surgical techniques and technologies for the management of patients with nonfunctioning pituitary adenomas," *Neurosurgery*, vol. 79, no. 4, p. E536, Oct. 2016. [Online].

Available: https://journals.lww.com/neurosurgery/fulltext/2016/10000/congress_of_neurological_surgeons_systematic.18.aspx

[33] M. Ashraf, U. A. Kamboh, M. A. Raza, N. U. Haq, N. Choudhary, K. A. Sultan, S. S. Hussain, and N. Ashraf, "Usefulness of intraoperative computed tomography on extent of resection of large and giant pituitary adenomas. experience from a developing country," *World Neurosurgery*, vol. 157, pp. 13–20, Jan. 2022. [Online]. Available: https://www.sciencedirect.com/science/article/pii/S1878875021014674

[34] H. J. Marcus, T. Vercauteren, S. Ourselin, and N. L. Dorward, "Intraoperative ultrasound in patients undergoing transsphenoidal surgery for pituitary adenoma: Systematic review," *World Neurosurgery*, vol. 106, pp. 680–685, Oct. 2017. [Online]. Available: https://www.sciencedirect.com/science/article/pii/S1878875017311543

[35] J. C. Watson, T. H. Shawker, L. K. Nieman, H. L. DeVroom, J. L. Doppman, and E. H. Oldfield, "Localization of pituitary adenomas by using intraoperative ultrasoound pituitary in patients with cushing's disease and no demonstrable tumor on magnetic resonance imaging," *Journal of Neurosurgery*, vol. 89, no. 6, pp. 927–932, 1998. [Online]. Available: https://thejns.org/view/journals/j-neurosurg/89/6/article-p927.xml

[36] O. Solheim, T. F. Johansen, J. Cappelen, G. Unsgård, and T. Selbekk, "Transsellar ultrasound in pituitary surgery with a designated probe: Early experiences," *Operative Neurosurgery*, vol. 12, no. 2, p. 128, Jun. 2016. [Online]. Available: https://journals.lww.com/onsonline/abstract/2016/06000/transsellar_ultrasound_in_pituitary_surgery_with_a.5.aspx

[37] M. Alshareef, S. Lowe, Y. Park, and B. Frankel, "Utility of intraoperative ultrasonography for resection of pituitary adenomas: a comparative retrospective study," *Acta Neurochirurgica*, vol. 163, no. 6, pp. 1725–1734, Jan. 2021. [Online]. Available: https://doi.org/10.1007/s00701-020-04674-2

[38] F. Kai, A. P. Drain, and V. M. Weaver, "The extracellular matrix modulates the metastatic journey," *Developmental Cell*, vol. 49, no. 3, pp. 332–346, May 2019. [Online]. Available: https://doi.org/10.1016/j.devcel.2019.03.026

[39] M. Meyer, N. Bouchonville, C. Gaude, E. Gay, D. Ratel, and A. Nicolas, "The micromechanical signature of pituitary adenomas: New perspectives for the diagnosis and surgery," *Advanced NanoBiomed Research*, vol. 1, no. 9, p. 2000085, May 2021. [Online]. Available: https://onlinelibrary.wiley.com/doi/abs/10.1002/anbr.202000085

[40] N. Lakomkin, J. J. Van Gompel, K. D. Post, S. S. Cho, J. Y. K. Lee, and C. G. Hadjipanayis, "Fluorescence guided surgery for pituitary adenomas," *Journal of Neuro-Oncology*, vol. 151, no. 3, pp. 403–413, Feb. 2021. [Online]. Available: https://api.semanticscholar.org/CorpusID:231971446

[41] J. Muto, Y. Mine, Y. Nishiyama, K. Murayama, M. Hayakawa, M. Hasegawa, J. K. Lee, and Y. Hirose, "Intraoperative real-time near-infrared image-guided endoscopic endonasal surgery for pituitary tumors," *World Neurosurgery*, vol. 175, pp. e218–e229, Jul. 2023. [Online]. Available: https://linkinghub.elsevier.com/retrieve/pii/S1878875023003777

[42] S. S. Cho and J. Y. K. Lee, "Intraoperative fluorescent visualization of pituitary adenomas," *Neurosurgery Clinics*, vol. 30, no. 4, pp. 401–412, Oct. 2019. [Online]. Available: https://www.neurosurgery.theclinics.com/article/S1042-3680(19)30038-5/fulltext

[43] C. Jackson, D. K. Kong, Z. C. Gersey, E. W. Wang, G. Zenonos, C. H. Snyderman, and P. A. Gardner, "Contact endoscopy as a novel technique for intra-operative identification of normal pituitary gland and adenoma," *Neurosurgical Focus: Video*, vol. 6, no. 1, p. V17, Jan. 2022. [Online]. Available: https://thejns.org/video/view/journals/neurosurg-focus-video/6/1/article-pV17.xml

[44] J. A. Kim, D. J. Wales, and G.-Z. Yang, "Optical spectroscopy for in vivo medical diagnosis—a review of the state of the art and future perspectives," *Progress in Biomedical Engineering*, vol. 2, no. 4, p. 042001, Aug. 2020. [Online]. Available: https://dx.doi.org/10.1088/2516-1091/abaaa3

[45] K. Eberhardt, C. Stiebing, C. Matthäus, M. Schmitt, and J. Popp, "Advantages and limitations of raman spectroscopy for molecular diagnostics: an update," *Expert Review of Molecular Diagnostics*, vol. 15, no. 6, pp. 773–787, Apr. 2015. [Online]. Available: https://www.tandfonline.com/doi/full/10.1586/14737159.2015.1036744

[46] C. V. Raman, "A change of wave-length in light scattering," *Nature*, vol. 121, no. 3051, pp. 619–619, Apr. 1928. [Online]. Available: https://www.nature.com/articles/121619b0

[47] S. O. Williams and D. G. Imre, "Raman spectroscopy: time-dependent pictures," *The Journal of Physical Chemistry*, vol. 92, no. 12, pp. 3363–3374, Jun. 1988. [Online]. Available: https://pubs.acs.org/doi/abs/10.1021/j100323a012

[48] G. D. Ewen Smith, "The theory of raman spectroscopy," in *Modern Raman Spectroscopy – A Practical Approach*. John Wiley & Sons, Ltd, Dec. 2004, pp. 71–92. [Online]. Available: https://onlinelibrary.wiley.com/doi/abs/10.1002/0470011831.ch3

[49] S. Koljenovic, T. C. B. Schut, R. Wolthuis, B. d. Jong, L. Santos, P. J. Caspers, J. M. Kros, and G. J. Puppels, "Tissue characterization using high wave number raman spectroscopy," *Journal of Biomedical Optics*, vol. 10, no. 3, p. 031116, May 2005. [Online]. Available: https://www.spiedigitallibrary.org/journals/journal-of-biomedical-optics/volume-10/issue-3/031116/Tissue-characterization-using-high-wave-number-Raman-spectroscopy/10.1117/1.1922307.full

[50] A. C. S. Talari, Z. Movasaghi, S. Rehman, and I. u. Rehman, "Raman spectroscopy of biological tissues," *Applied Spectroscopy Reviews*, vol. 50, no. 1, pp. 46–111, Aug. 2014. [Online]. Available: https://doi.org/10.1080/05704928.2014.923902

[51] A. Rygula, K. Majzner, K. M. Marzec, A. Kaczor, M. Pilarczyk, and M. Baranska, "Raman spectroscopy of proteins: a review," *Journal of Raman Spectroscopy*, vol. 44, no. 8, pp. 1061–1076, Jul. 2013. [Online]. Available: https://onlinelibrary.wiley.com/doi/abs/10.1002/jrs.4335

[52] K. Czamara, K. Majzner, M. Z. Pacia, K. Kochan, A. Kaczor, and M. Baranska, "Raman spectroscopy of lipids: a review," *Journal of Raman Spectroscopy*, vol. 46, no. 1, pp. 4–20, Dec. 2014. [Online]. Available: https://onlinelibrary.wiley.com/doi/abs/10.1002/jrs.4607

[53] G. Zhu, X. Zhu, Q. Fan, and X. Wan, "Raman spectra of amino acids and their aqueous solutions," *Spectrochimica Acta Part A: Molecular and Biomolecular Spectroscopy*, vol. 78, no. 3, pp. 1187–1195, Mar. 2011. [Online]. Available: https://www.sciencedirect.com/science/article/pii/S1386142510007043

[54] M. Monici, "Cell and tissue autofluorescence research and diagnostic applications," in *Biotechnology Annual Review*. Elsevier, 2005, vol. 11, pp. 227–256. [Online]. Available: https://www.sciencedirect.com/science/article/pii/S1387265605110072

[55] A. C. Croce and G. Bottiroli, "Autofluorescence spectroscopy and imaging: A tool for biomedical research and diagnosis," *European Journal of Histochemistry : EJH*, vol. 58, no. 4, p. 2461, Dec. 2014. [Online]. Available: https://pmc.ncbi.nlm.nih.gov/articles/PMC4289852/

[56] P. Taroni, A. Pifferi, A. Torricelli, D. Comelli, and R. Cubeddu, "In vivo absorption and scattering spectroscopy of biological tissues," *Photochemical & Photobiological Sciences: Official Journal of the European Photochemistry Association and the European Society for Photobiology*, vol. 2, no. 2, pp. 124–129, Feb. 2003. [Online]. Available: https://doi.org/10.1039/B209651J

[57] I. P. Santos, E. M. Barroso, T. C. B. Schut, P. J. Caspers, C. G. F. v. Lanschot, D.-H. Choi, M. F. v. d. Kamp, R. W. H. Smits, R. v. Doorn, R. M. Verdijk, V. N. Hegt, J. H. v. d. Thüsen, C. H. M. v. Deurzen, L. B. Koppert, G. J. L. H. v. Leenders, P. C. Ewing-Graham, H. C. v. Doorn, C. M. F. Dirven, M. B. Busstra, J. Hardillo, A. Sewnaik, I. t. Hove, H. Mast, D. A. Monserez, C. Meeuwis, T. Nijsten, E. B. Wolvius, R. J. B. d. Jong, G. J. Puppels, and S. Koljenović, "Raman spectroscopy for cancer detection and cancer surgery guidance: translation to the clinics," *Analyst*, vol. 142, no. 17, pp. 3025–3047, Aug. 2017. [Online]. Available: https://pubs.rsc.org/en/content/articlelanding/2017/an/c7an00957g

[58] S. Valastyan and R. A. Weinberg, "Tumor metastasis: Molecular insights and evolving paradigms," *Cell*, vol. 147, no. 2, pp. 275–292, Oct. 2011. [Online]. Available: https://www.cell.com/cell/abstract/S0092-8674(11)01085-3

[59] K. Ember, F. Dallaire, A. Plante, G. Sheehy, M.-C. Guiot, R. Agarwal, R. Yadav, A. Douet, J. Selb, J. P. Tremblay, A. Dupuis, E. Marple, K. Urmey, C. Rizea, A. Harb, L. McCarthy, A. Schupper, M. Umphlett, N. Tsankova, F. Leblond, C. Hadjipanayis, and K. Petrecca, "In situ brain tumor detection using a raman spectroscopy system—results of a multicenter study," *Scientific Reports*, vol. 14, no. 1, p. 13309, Jun. 2024. [Online]. Available: https://www.nature.com/articles/s41598-024-62543-9

[60] M. Jermyn, K. Mok, J. Mercier, J. Desroches, J. Pichette, K. Saint-Arnaud, L. Bernstein, M.-C. Guiot, K. Petrecca, and F. Leblond, "Intraoperative brain cancer detection with raman spectroscopy in humans," *Science Translational Medicine*, vol. 7, no. 274, p. 274ra19, Feb. 2015. [Online]. Available: https://www.science.org/doi/10.1126/scitranslmed.aaa2384

[61] S. Murugappan, S. A. M. Tofail, and N. D. Thorat, "Raman spectroscopy: A tool for molecular fingerprinting of brain cancer," *ACS Omega*, vol. 8, no. 31, pp. 27 845–27 861, Jul. 2023. [Online]. Available: https://doi.org/10.1021/acsomega.3c01848

[62] J. Schleusener, P. Gluszczynska, C. Reble, I. Gersonde, J. Helfmann, J. W. Fluhr, J. Lademann, J. Röwert-Huber, A. Patzelt, and M. C. Meinke, "In vivo study

for the discrimination of cancerous and normal skin using fibre probe-based raman spectroscopy," *Experimental Dermatology*, vol. 24, no. 10, pp. 767–772, Oct. 2015. [Online]. Available: https://doi.org/10.1111/exd.12768

[63] H. C. McGregor, M. A. Short, S. Lam, T. Shaipanich, E.-L. Beaudoin, and H. Zeng, "Development and in vivo test of a miniature raman probe for early cancer detection in the peripheral lung," *Journal of Biophotonics*, vol. 11, no. 11, p. e201800055, Nov. 2018. [Online]. Available: https://doi.org/10.1002/jbio.201800055

[64] S. David, A. Plante, F. Dallaire, J.-P. Tremblay, G. Sheehy, E. Macdonald, L. Forrest, M. Daneshmand, D. Trudel, B. C. Wilson, L. Hopkins, S. Murugkar, B. Vanderhyden, and F. Leblond, "Multispectral label-free raman spectroscopy can detect ovarian and endometrial cancer with high accuracy," *Journal of Biophotonics*, vol. 15, no. 2, p. e202100198, Nov. 2021. [Online]. Available: https://doi.org/10.1002/jbio.202100198

[65] F. Picot, R. Shams, F. Dallaire, G. Sheehy, T. Trang, D. Grajales, M. Birlea, D. Trudel, C. Ménard, S. Kadoury, and F. Leblond, "Image-guided raman spectroscopy navigation system to improve transperineal prostate cancer detection. part 1: Raman spectroscopy fiber-optics system and in situ tissue characterization," *Journal of Biomedical Optics*, vol. 27, no. 9, p. 095003, Sep. 2022. [Online]. Available: https://www.spiedigitallibrary.org/journals/journal-of-biomedical-optics/volume-27/issue-9/095003/Image-guided-Raman-spectroscopy-navigation-system-to-improve-transperineal-prostate/10.1117/1.JBO.27.9.095003.full

[66] K. Hanna, E. Krzoska, A. M. Shaaban, D. Muirhead, R. Abu-Eid, and V. Speirs, "Raman spectroscopy: current applications in breast cancer diagnosis, challenges and future prospects," *British Journal of Cancer*, vol. 126, no. 8, pp. 1125–1139, Dec. 2021. [Online]. Available: https://www.nature.com/articles/s41416-021-01659-5

[67] S. David, T. Tran, F. Dallaire, G. Sheehy, F. Azzi, D. Trudel, F. Tremblay, A. Omeroglu, F. Leblond, and S. Meterissian, "In situ raman spectroscopy and machine learning unveil biomolecular alterations in invasive breast cancer," *Journal of Biomedical Optics*, vol. 28, no. 3, p. 036009, Mar. 2023. [Online]. Available: https://www.spiedigitallibrary.org/journals/journal-of-biomedical-optics/volume-28/issue-3/036009/In-situ-Raman-spectroscopy-and-machine-learning-unveil-biomolecular-alterations/10.1117/1.JBO.28.3.036009.full

[68] G. W. Auner, S. K. Koya, C. Huang, B. Broadbent, M. Trexler, Z. Auner, A. Elias, K. C. Mehne, and M. A. Brusatori, "Applications of raman spectroscopy in cancer diagnosis," *Cancer Metastasis Reviews*, vol. 37, no. 4, pp. 691–717, Dec. 2018. [Online]. Available: https://europepmc.org/articles/PMC6514064

[69] Y. Zhou, C.-H. Liu, Y. Sun, Y. Pu, S. Boydston-White, Y. Liu, and R. R. Alfano, "Human brain cancer studied by resonance raman spectroscopy," *Journal of Biomedical Optics*, vol. 17, no. 11, p. 116021, Aug. 2013. [Online]. Available: https://doi.org/10.7785/tcrt.2012.500325

[70] D. Bovenkamp, A. Micko, J. Püls, F. Placzek, R. Höftberger, G. Vila, R. Leitgeb, W. Drexler, M. Andreana, S. Wolfsberger, and A. Unterhuber, "Line scan raman microspectroscopy for label-free diagnosis of human pituitary biopsies," *Molecules*, vol. 24, no. 19, p. 3577, Oct. 2019. [Online]. Available: https://www.mdpi.com/1420-3049/24/19/3577

[71] G. Giardina, A. Micko, D. Bovenkamp, A. Krause, F. Placzek, L. Papp, D. Krajnc, C. P. Spielvogel, M. Winklehner, R. Höftberger, G. Vila, M. Andreana, R. Leitgeb, W. Drexler, S. Wolfsberger, and A. Unterhuber, "Morpho-molecular metabolic analysis and classification of human pituitary gland and adenoma biopsies based on multimodal optical imaging," *Cancers*, vol. 13, no. 13, p. 3234, Jun. 2021. [Online]. Available: https://www.mdpi.com/2072-6694/13/13/3234

[72] A. Banerjee, A. Halder, P. Jadhav, R. Bankar, J. Pattarkine, A. Hole, A. Shah, A. Goel, C. Murali Krishna, and S. Srivastava, "Metabolomics profiling of pituitary adenomas by raman spectroscopy, attenuated total reflection-fourier transform infrared spectroscopy, and mass spectrometry of serum samples," *Analytical Chemistry*, vol. 94, no. 34, pp. 11 898–11 907, Aug. 2022. [Online]. Available: https://doi.org/10.1021/acs.analchem.2c02487

[73] M. Jermyn, J. Mercier, K. Aubertin, J. Desroches, K. Urmey, J. Karamchandiani, E. Marple, M.-C. Guiot, F. Leblond, and K. Petrecca, "Highly accurate detection of cancer in situ with intraoperative, label-free, multimodal optical spectroscopy," *Cancer Research*, vol. 77, no. 14, pp. 3942–3950, Jul. 2017. [Online]. Available: https://doi.org/10.1158/0008-5472.CAN-17-0668

[74] J. Desroches, M. Jermyn, K. Mok, C. Lemieux-Leduc, J. Mercier, K. St-Arnaud, K. Urmey, M.-C. Guiot, E. Marple, K. Petrecca, and F. Leblond, "Characterization of a raman spectroscopy probe system for intraoperative brain tissue classification,"

Biomedical Optics Express, vol. 6, no. 7, pp. 2380–2397, Jul. 2015. [Online]. Available: https://opg.optica.org/boe/abstract.cfm?uri=boe-6-7-2380

[75] D. Wei, S. Chen, and Q. Liu, "Review of fluorescence suppression techniques in raman spectroscopy," *Applied Spectroscopy Reviews*, vol. 50, no. 5, pp. 387–406, Mar. 2015. [Online]. Available: https://doi.org/10.1080/05704928.2014.999936

[76] C. A. Lieber and A. Mahadevan-Jansen, "Automated method for subtraction of fluorescence from biological raman spectra," *Applied Spectroscopy*, vol. 57, no. 11, pp. 1363–1367, Nov. 2003. [Online]. Available: https://doi.org/10.1366/000370203322554518

[77] G. Sheehy, F. Picot, F. Dallaire, K. Ember, T. Nguyen, K. Petrecca, D. Trudel, and F. Leblond, "Open-sourced raman spectroscopy data processing package implementing a baseline removal algorithm validated from multiple datasets acquired in human tissue and biofluids," *Journal of Biomedical Optics*, vol. 28, no. 2, p. 025002, Feb. 2023. [Online]. Available: https://www.ncbi.nlm.nih.gov/pmc/articles/PMC9941747/

[78] M. N. Leger and A. G. Ryder, "Comparison of derivative preprocessing and automated polynomial baseline correction method for classification and quantification of narcotics in solid mixtures," *Applied Spectroscopy*, vol. 60, no. 2, pp. 182–193, Feb. 2006. [Online]. Available: https://opg.optica.org/as/abstract.cfm?uri=as-60-2-182

[79] M. A. da Silva Martins, D. G. Ribeiro, E. A. Pereira dos Santos, A. A. Martin, A. Fontes, and H. da Silva Martinho, "Shifted-excitation raman difference spectroscopy for in vitro and in vivo biological samples analysis," *Biomedical Optics Express*, vol. 1, no. 2, pp. 617–626, Aug. 2010. [Online]. Available: https://www.ncbi.nlm.nih.gov/pmc/articles/PMC3018003/

[80] M. Kögler and B. Heilala, "Time-gated raman spectroscopy – a review," *Measurement Science and Technology*, vol. 32, no. 1, p. 012002, Oct. 2020. [Online]. Available: https://dx.doi.org/10.1088/1361-6501/abb044

[81] N. Blake, R. Gaifulina, L. D. Griffin, I. M. Bell, and G. M. H. Thomas, "Machine learning of raman spectroscopy data for classifying cancers: A review of the recent literature," *Diagnostics (Basel, Switzerland)*, vol. 12, no. 6, p. 1491, Jun. 2022. [Online]. Available: https://doi.org/10.3390/diagnostics12061491

[82] T. Sciortino, R. Secoli, E. d'Amico, S. Moccia, M. Conti Nibali, L. Gay, M. Rossi, N. Pecco, A. Castellano, E. De Momi, B. Fernandes, M. Riva, and L. Bello,

"Raman spectroscopy and machine learning for IDH genotyping of unprocessed glioma biopsies," *Cancers*, vol. 13, no. 16, p. 4196, Aug. 2021. [Online]. Available: https://doi.org/10.3390/cancers13164196

[83] X. Li, T. Yang, S. Li, D. Wang, Y. Song, and S. Zhang, "Raman spectroscopy combined with principal component analysis and k nearest neighbour analysis for non-invasive detection of colon cancer," *Laser Physics*, vol. 26, no. 3, p. 035702, Feb. 2016. [Online]. Available: https://dx.doi.org/10.1088/1054-660X/26/3/035702

[84] D. Bury, G. Faust, M. Paraskevaidi, K. M. Ashton, T. P. Dawson, and F. L. Martin, "Phenotyping metastatic brain tumors applying spectrochemical analyses: Segregation of different cancer types," *Analytical Letters*, vol. 52, no. 4, pp. 575–587, Jul. 2018. [Online]. Available: https://doi.org/10.1080/00032719.2018.1479412

[85] M.-J. Jeng, M. Sharma, L. Sharma, T.-Y. Chao, S.-F. Huang, L.-B. Chang, S.-L. Wu, and L. Chow, "Raman spectroscopy analysis for optical diagnosis of oral cancer detection," *Journal of Clinical Medicine*, vol. 8, no. 9, p. 1313, Aug. 2019. [Online]. Available: https://doi.org/10.3390/jcm8091313

[86] K. Aubertin, V. Q. Trinh, M. Jermyn, P. Baksic, A.-A. Grosset, J. Desroches, K. St-Arnaud, M. Birlea, M. C. Vladoiu, M. Latour, R. Albadine, F. Saad, F. Leblond, and D. Trudel, "Mesoscopic characterization of prostate cancer using raman spectroscopy: potential for diagnostics and therapeutics," *BJU international*, vol. 122, no. 2, pp. 326–336, Aug. 2018. [Online]. Available: https://doi.org/10.1111/bju.14199

[87] D. Ma, L. Shang, J. Tang, Y. Bao, J. Fu, and J. Yin, "Classifying breast cancer tissue by raman spectroscopy with one-dimensional convolutional neural network," *Spectrochimica Acta. Part A, Molecular and Biomolecular Spectroscopy*, vol. 256, p. 119732, Jul. 2021. [Online]. Available: https://doi.org/10.1016/j.saa.2021.119732

[88] X. Wu, S. Li, Q. Xu, X. Yan, Q. Fu, X. Fu, X. Fang, and Y. Zhang, "Rapid and accurate identification of colon cancer by raman spectroscopy coupled with convolutional neural networks," *Japanese Journal of Applied Physics*, vol. 60, no. 6, p. 067001, May 2021. [Online]. Available: https://dx.doi.org/10.35848/1347-4065/ac0005

[89] P. Pradhan, S. Guo, O. Ryabchykov, J. Popp, and T. W. Bocklitz, "Deep learning a boon for biophotonics?" *Journal of Biophotonics*, vol. 13, no. 6, p. e201960186, Jun. 2020.

[90] K. Hajian-Tilaki, "Receiver operating characteristic (ROC) curve analysis for medical diagnostic test evaluation," *Caspian Journal of Internal Medicine*, vol. 4, no. 2, pp. 627–635, 2013. [Online]. Available: https://www.ncbi.nlm.nih.gov/pmc/articles/PMC3755824/

[91] A. Akbarzadeh, E. Edjlali, G. Sheehy, J. Selb, R. Agarwal, J. Weber, and F. Leblond, "Experimental validation of a spectroscopic monte carlo light transport simulation technique and raman scattering depth sensing analysis in biological tissue," *Journal of Biomedical Optics*, vol. 25, no. 10, p. 105002, Oct. 2020. [Online]. Available: https://doi.org/10.1117/1.JBO.25.10.105002

[92] S. L. Jacques, "Optical properties of biological tissues: a review," *Physics in Medicine & Biology*, vol. 58, no. 11, p. R37, May 2013. [Online]. Available: https://dx.doi.org/10.1088/0031-9155/58/11/R37

[93] J. L. Sandell and T. C. Zhu, "A review of in-vivo optical properties of human tissues and its impact on PDT," *Journal of Biophotonics*, vol. 4, no. 11, pp. 773–787, 2011. [Online]. Available: https://onlinelibrary.wiley.com/doi/abs/10.1002/jbio.201100062

[94] W. Cheong, S. Prahl, and A. Welch, "A review of the optical properties of biological tissues," *IEEE Journal of Quantum Electronics*, vol. 26, no. 12, pp. 2166–2185, May 1990. [Online]. Available: https://ieeexplore.ieee.org/document/64354/?arnumber=64354

[95] F. Dallaire, F. Picot, J.-P. Tremblay, G. Sheehy, Lemoine, R. Agarwal, S. Kadoury, D. Trudel, F. Lesage, K. Petrecca, and F. Leblond, "Quantitative spectral quality assessment technique validated using intraoperative in vivo raman spectroscopy measurements," *Journal of Biomedical Optics*, vol. 25, no. 4, p. 040501, Apr. 2020. [Online]. Available: https://www.spiedigitallibrary.org/journals/journal-of-biomedical-optics/volume-25/issue-4/040501/Quantitative-spectral-quality-assessment-technique-validated-using-intraoperative-in-vivo/10.1117/1.JBO.25.4.040501.full

[96] R. P. Aguiar, E. T. Falcão, C. A. Pasqualucci, and L. Silveira, "Use of raman spectroscopy to evaluate the biochemical composition of normal and tumoral human brain tissues for diagnosis," *Lasers in Medical Science*, vol. 37, no. 1, pp. 121–133, Nov. 2022. [Online]. Available: https://doi.org/10.1007/s10103-020-03173-1

[97] J. Desroches, A. Laurence, M. Jermyn, M. Pinto, M.-A. Tremblay, K. Petrecca, and F. Leblond, "Raman spectroscopy in microsurgery: impact of operating

microscope illumination sources on data quality and tissue classification," *Analyst*, vol. 142, no. 8, pp. 1185–1191, Apr. 2017. [Online]. Available: https://pubs.rsc.org/en/content/articlelanding/2017/an/c6an02061e

[98] N. Adeeb, M. M. Mortazavi, R. S. Tubbs, and A. A. Cohen-Gadol, "The cranial dura mater: a review of its history, embryology, and anatomy," *Child's Nervous System*, vol. 28, no. 6, pp. 827–837, Apr. 2012. [Online]. Available: https://doi.org/10.1007/s00381-012-1744-6

[99] I. Nasi-Kordhishti, S. Giese, B. Hirt, and J. Honegger, "Chapter 5 - anatomy of the pituitary region," in *Pituitary Tumors*, J. Honegger, M. Reincke, and S. Petersenn, Eds. Academic Press, Apr. 2021, pp. 67–85. [Online]. Available: https://www.sciencedirect.com/science/article/pii/B9780128199497000615

[100] F. A. Kruse, A. B. Lefkoff, J. W. Boardman, K. B. Heidebrecht, A. T. Shapiro, P. J. Barloon, and A. F. H. Goetz, "The spectral image processing system (SIPS)—interactive visualization and analysis of imaging spectrometer data," *Remote Sensing of Environment*, vol. 44, no. 2, pp. 145–163, May 1993. [Online]. Available: https://www.sciencedirect.com/science/article/pii/003442579390013N

[101] A. Plante, F. Dallaire, A.-A. Grosset, T. Nguyen, M. Birlea, J. Wong, F. Daoust, N. Roy, A. Kougioumoutzakis, F. Azzi, K. Aubertin, S. Kadoury, M. Latour, R. Albadine, S. Prendeville, P. Boutros, M. Fraser, R. G. Bristow, T. V. D. Kwast, M. Orain, H. Brisson, N. Benzerdjeb, H. Hovington, A. Bergeron, Y. Fradet, B. Têtu, F. Saad, D. Trudel, and F. Leblond, "Dimensional reduction based on peak fitting of raman micro spectroscopy data improves detection of prostate cancer in tissue specimens," *Journal of Biomedical Optics*, vol. 26, no. 11, p. 116501, Nov. 2021. [Online]. Available: https://www.spiedigitallibrary.org/journals/journal-of-biomedical-optics/volume-26/issue-11/116501/Dimensional-reduction-based-on-peak-fitting-of-Raman-micro-spectroscopy/10.1117/1.JBO.26.11.116501.full

[102] X. Feng, "Chemical and biochemical basis of cell-bone matrix interaction in health and disease," *Current Chemical Biology*, vol. 3, no. 2, pp. 189–196, May 2009. [Online]. Available: https://doi.org/10.2174/187231309788166398

[103] H. Singh and K. K. Carroll, "Lipid composition of beef and human pituitary glands," *Lipids*, vol. 5, no. 1, pp. 121–127, Jan. 1970. [Online]. Available: https://doi.org/10.1007/BF02531106

[104] Y. Poitelon, A. M. Kopec, and S. Belin, "Myelin fat facts: An overview of lipids and fatty acid metabolism," *Cells*, vol. 9, no. 4, p. 812, Mar. 2020. [Online]. Available: https://doi.org/10.3390/cells9040812

[105] P. Morell and R. H. Quarles, "Characteristic composition of myelin," in *Basic Neurochemistry: Molecular, Cellular and Medical Aspects. 6th edition.* Lippincott-Raven, 1999. [Online]. Available: https://www.ncbi.nlm.nih.gov/books/NBK28221/

[106] K. M. Beekman, G. Duque, A. Corsi, M. Tencerova, P. H. Bisschop, and J. Paccou, "Osteoporosis and bone marrow adipose tissue," *Current Osteoporosis Reports*, vol. 21, no. 1, pp. 45–55, Feb. 2023. [Online]. Available: https://doi.org/10.1007/s11914-022-00768-1

[107] S. M. Ott, "Cortical or trabecular bone: What's the difference?" *American Journal of Nephrology*, vol. 47, no. 6, pp. 373–375, Jul. 2018. [Online]. Available: https://doi.org/10.1159/000489672

[108] S. Timmler and M. Simons, "Grey matter myelination," *Glia*, vol. 67, no. 11, pp. 2063–2070, Nov. 2019. [Online]. Available: ttps://doi.org/10.1002/glia.23614

[109] Innovative Photonic Solutions, *IPS Digital U-Type Module User Guide*, Innovative Photonic Solutions, Plainsboro, NJ, USA, accessed December 2024. [Online]. Available: http://www.innovativephotonics.com/multi-mode-digital-u-type-module/

[110] International Electrotechnical Commission, "IEC 60825-1:2014 - safety of laser products - part 1: Equipment classification and requirements." [Online]. Available: https://webstore.iec.ch/en/publication/3587

[111] American National Standards Institute, "ANSI Z136.1: Safe Use of Lasers," 2014. [Online]. Available: https://www.ansi.org/

[112] ——, "ANSI Z136.3: Safe Use of Lasers in Health Care," 2018. [Online]. Available: https://www.ansi.org/

[113] Y. Tanaka, H. Motomura, and M. Jinno, "Biological defenses against ultra-violet, visible light, and near-infrared exposure," *Optics and Photonics Journal*, vol. 6, no. 1, pp. 8–14, Jan. 2016. [Online]. Available: https://www.scirp.org/journal/paperinformation?paperid=63105

[114] Karl Storz Endoskope, *Instructions for use: Fiber optic light cable, fluid light cable*, 04 2022. [Online].

Available: https://www.bioclinicalservices.com.au/karl-storz-endoskope/surgical/fiber-optic-light-cable-fluid-light-cable-instructions-for-use

[115] F. Faul, E. Erdfelder, A. Buchner, and A.-G. Lang, "Statistical power analyses using g*power 3.1: Tests for correlation and regression analyses," *Behavior Research Methods*, vol. 41, no. 4, pp. 1149–1160, Nov. 2009. [Online]. Available: https://doi.org/10.3758/BRM.41.4.1149

[116] D.-A. Nguyen, H. T. Nguyen, T. V. Duong, B. H. Pham, and H.-L. Vo, "Surgical treatment of cavernous sinus cavernomas: Evidence from vietnam," *Reports*, vol. 3, no. 2, p. 16, May 2020. [Online]. Available: https://www.mdpi.com/2571-841X/3/2/16

[117] C. G. Atkins, K. Buckley, M. W. Blades, and R. F. Turner, "Raman spectroscopy of blood and blood components," *Applied Spectroscopy*, vol. 71, no. 5, pp. 767–793, Apr. 2017. [Online]. Available: https://doi.org/10.1177/0003702816686593

[118] Y.-X. Huang, Z.-J. Wu, B.-T. Huang, and M. Luo, "Pathway and mechanism of pH dependent human hemoglobin tetramer-dimer-monomer dissociations," *PLOS ONE*, vol. 8, no. 11, p. e81708, Nov. 2013. [Online]. Available: https://doi.org/10.1371/journal.pone.0081708

[119] Z. N. Litvack, G. Zada, and E. R. Laws, "Indocyanine green fluorescence endoscopy for visual differentiation of pituitary tumor from surrounding structures," *Journal of Neurosurgery*, vol. 116, no. 5, pp. 935–941, May 2012. [Online]. Available: https://doi.org/10.3171/2012.1.JNS11601

[120] F. Leblond, F. Dallaire, K. Ember, A. L. Moël, V. Blanquez-Yeste, H. Tavera, G. Sheehy, T. Tran, M.-C. Guiot, A. G. Weil, R. Dudley, C. Hadjipanayis, and K. Petrecca, "Quantitative assessment of the generalizability of a brain tumor raman spectroscopy machine learning model to various tumor types including astrocytoma and oligodendroglioma," *Journal of Biomedical Optics*, vol. 30, no. 1, p. 010501, Jan. 2025. [Online]. Available: https://www.spiedigitallibrary.org/journals/journal-of-biomedical-optics/volume-30/issue-1/010501/Quantitative-assessment-of-the-generalizability-of-a-brain-tumor-Raman/10.1117/1.JBO.30.1.010501.full

[121] M. Berry, "How to reduce fluorescence in raman spectroscopy," Edinburgh Instruments, Edinburgh, Scotland, Tech. Rep., Dec. 2022. [Online]. Available: https://doi.org/10.3171/2012.1.JNS11601

[122] B. Halász, "Pituitary gland anatomy and embryology," in *Encyclopedia of Endocrine Diseases*, L. Martini, Ed. Elsevier, Jan. 2004, pp. 636–643. [Online]. Available: https://doi.org/10.1016/B0-12-475570-4/01022-2

APPENDIX A ANATOMICAL STRUCTURES OF THE SELLAR REGION

The content presented in this section is based on the following references: [2, 4, 10, 122].

The sellar region is a crucial anatomical area explored during transsphenoidal surgeries and illustrated in Figure A.1. It is located in the central base of the skull, containing the sella turcica, where the pituitary gland is lodged. The sellar area is surrounded by critical neurovascular structures, which explains its skilled surgical requirement. The sella turcica is inferiorly bordered by the sphenoid sinus, laterally by the cavernous sinuses, and superiorly by the diaphragma sellae. The cavernous sinus contains many cranial nerves (III, IV, V1, V2, and VI), along with the internal carotid artery. The optic chiasm lies above the diaphragm, which is fundamental for visual pathways. These structures must be carefully navigated during surgery to avoid any complications.

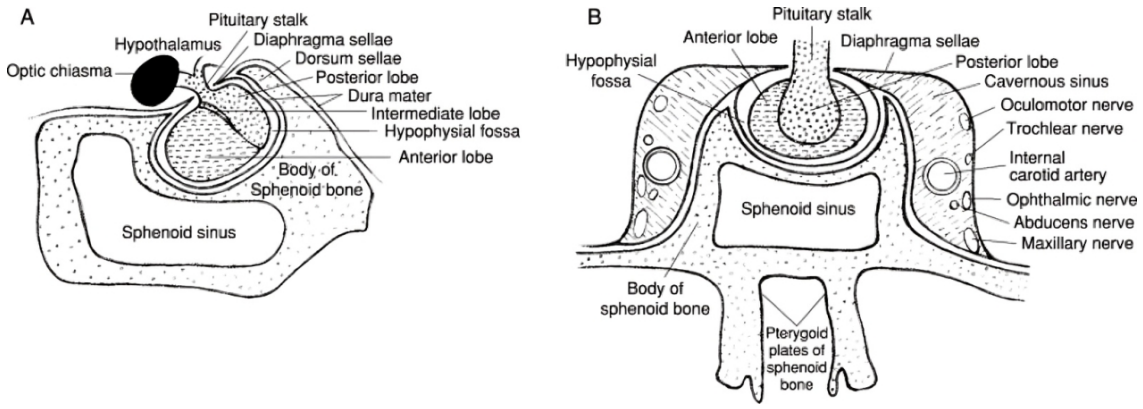

Figure A.1 Schematic of the location and topography of the pituitary in a midsagittal section (A) and a coronal section (B) of the sphenoid bone. Reprinted from [122] with permission.

The surgical procedure to access the sellar region is usually achieved through a transsphenoidal approach. This approach involves passing through the sphenoid sinus to reach the sella turcica and allow miniminal disruption to the surrounding structures. This method is frequently employed in the treatment of pituitary adenomas and other sellar pathologies.

The pituitary gland is divided into two main parts: the anterior lobe (adenohypophysis) and the posterior lobe (neurohypophysis). This gland plays a critical role in the endocrine system. Often referred to as the "master gland" it controls hormone regulation and numerous physiological processes through the release of hormones such as growth hormone (GH), adrenocorticotropic hormone (ACTH), and thyroid-stimulating hormone (TSH).

APPENDIX B HAND-HELD ENDONASAL RAMAN SPECTROSCOPY PROBE: TECHNICAL DESIGN

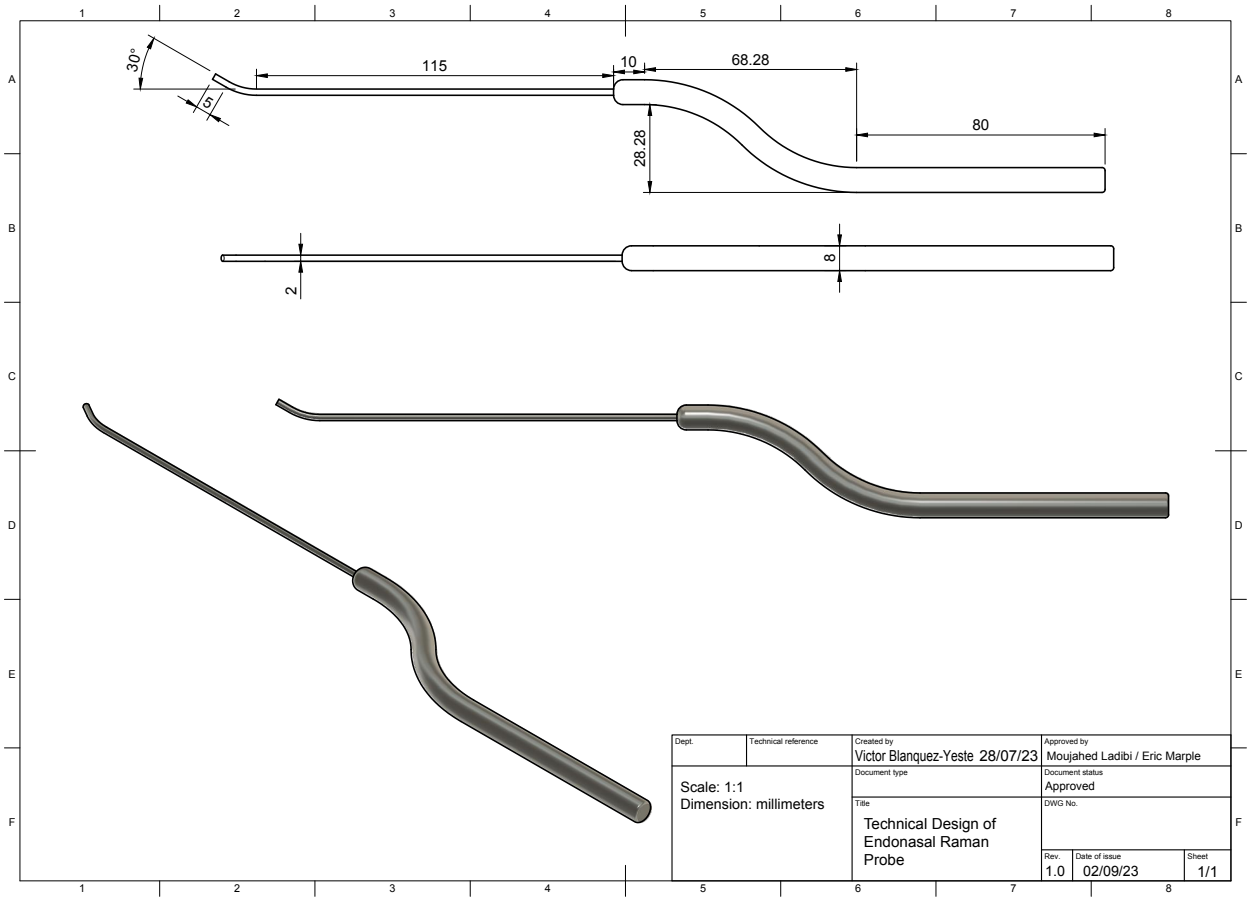

Figure B.1 Technical drawing of the design of the hand-held endonasal Raman spectroscopy probe.

APPENDIX C SMA PROBE CONNECTOR DESIGN FOR *LUMED LAB* SYSTEMS

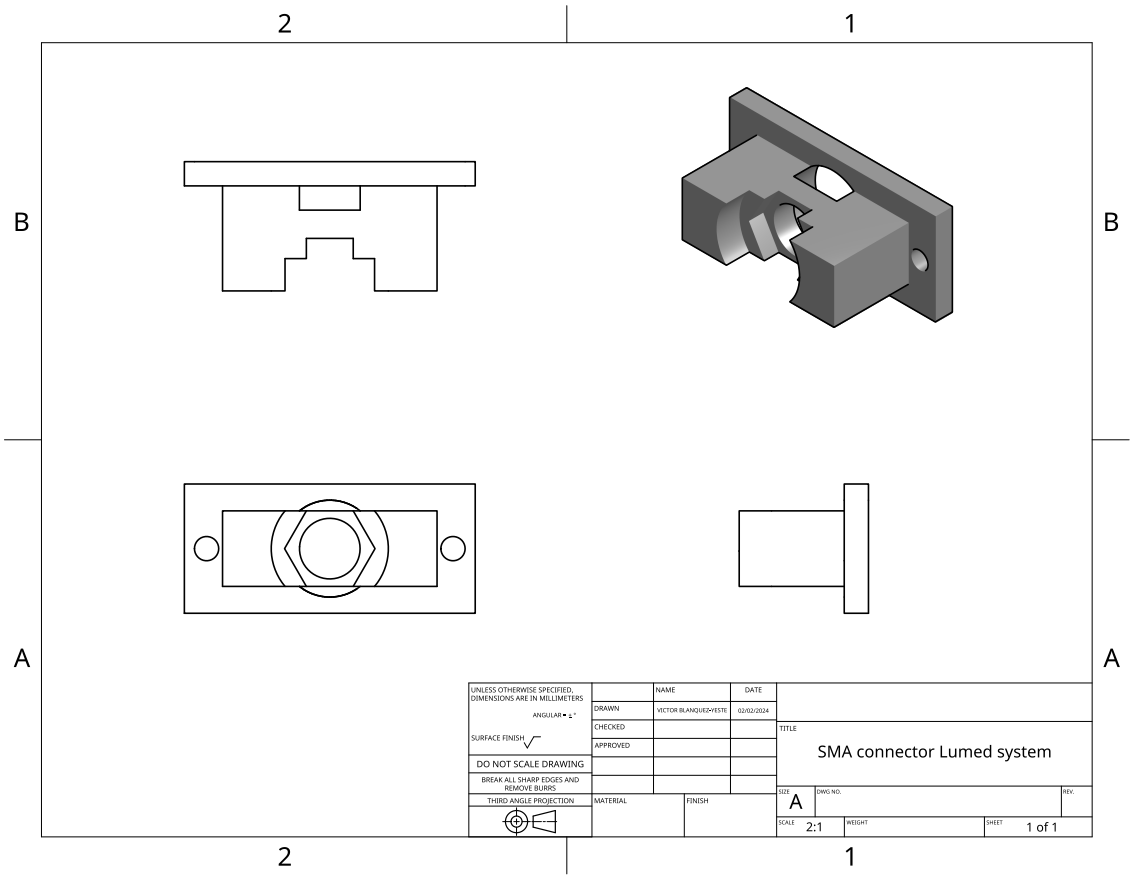

Figure C.1 Technical drawing of the component designed to function as a connector for Raman probes with SMA fibers and *Lumed lab* RS systems.

The designed component is intended to be used with a *Thorlabs* SMA to SMA mating sleeve (ADASMA), to function as a connector for SMA to SMA fibers for *Lumed lab* systems.